UNIVERSITY OF CUKUROVA
INSTITUTE OF NATURAL AND APPLIED SCIENCES

Ph.D. THESIS

Candan IŞIK

INCLUSIVE SEARCH OF THE HYPOTHETICAL X_b EXOTIC STATE DECAYS TO $\chi_{b1}(1P)\pi^+\pi^-$ and $\Upsilon(1S)\pi^+\pi^-$ FINAL STATES WITH RUN-II DATA COLLECTED BY THE CMS EXPERIMENT AT THE LARGE HADRON COLLIDER

DEPARTMENT OF PHYSICS

ADANA, 2021

To my family

ABSTRACT

Ph.D THESIS

INCLUSIVE SEARCH OF THE HYPOTHETICAL X_b EXOTIC STATE DECAYS TO $\chi_{b1}(1P)\pi^+\pi^-$ and $\Upsilon(1S)\pi^+\pi^-$ FINAL STATES WITH RUN-II DATA COLLECTED BY THE CMS EXPERIMENT AT THE LARGE HADRON COLLIDER

Candan IŞIK

DEPARTMENT OF PHYSICS
INSTITUTE OF NATURAL AND APPLIED SCIENCES
UNIVERSITY OF ÇUKUROVA

Supervisor : Prof. Dr. İsa DUMANOĞLU
Year : 2021, Pages : 132
Jury : Prof. Dr. İsa DUMANOĞLU
: Prof. Dr. Ayşe POLATÖZ
: Prof. Dr. Aysel KAYIŞ TOPAKSU
: Prof. Dr. Sezgin AYDIN
: Asst. Prof. Dr. Evrim Ersin KANGAL

An analysis of $\Upsilon(1S)\pi^+\pi^-$ and $\chi_{b1}(1P)\pi^+\pi^-$ final states have been performed, with the purpose to search for the possible exotic X_b signal, by exploiting the nearly whole data sample collected during the Run-II data taking by the CMS experiment. Two decay chains were fully implemented and configured to obtain the distributions for the $\Upsilon(1S)\pi^+\pi^-$ and $\chi_{b1}(1P)\pi^+\pi^-$ final states. The reconstruction of the χ_{b1} state through its radiative decay has shown the importance of the photons reconstruction by their conversion in the CMS Tracker material. The obtained spectra for the two final states ($\Upsilon(1S)\pi^+\pi^-$ and $\chi_{b1}(1P)\pi^+\pi^-$ allow to report no significant peaking structure that could be associated with the hypothetical X_b exotic state.

Key Words: Exotic hadrons, X(3872), X_b, pp Collision, CMS

ÖZ

DOKTORA TEZİ

$\chi_{b1}(1P)\pi^+\pi^-$ ve $\Upsilon(1S)\pi^+\pi^-$ SON DURUMLARINA GİDEN HİPOTETİK X_b EGZOTİK DURUMLARININ BÜYÜK HADRON ÇARPIŞTIRICISIN'NDAKİ CMS DENEYİNDEN ALINAN RUN-II VERİLERİ KULLANILARAK KAPSAMLI BİR ŞEKİLDE ARAŞTIRILMASI

Candan IŞIK

ÇUKUROVA ÜNİVERSİTESİ
FEN BİLİMLERİ ENSTİTÜSÜ
FiZiK ANABİLİM DALI

Danışman : Prof. Dr. İsa DUMANOĞLU
Yıl : 2021, Sayfa : 132
Jüri : Prof. Dr. İsa DUMANOĞLU
: Prof. Dr. Ayşe POLATÖZ
: Prof. Dr. Aysel KAYIŞ TOPAKSU
: Prof. Dr. Sezgin AYDIN
: Dr. Ögr. Evrim Ersin KANGAL

Olası egzotik X_b sinyalini aramak amacıyla $\chi_{b1}(1P)\pi^+\pi^-$ ve $\Upsilon(1S)\pi^+\pi^-$ nihai durumlarının analizi CMS deneyinde Run-II verileri alımı sırasında toplanan neredeyse tüm veri örneğinden yararlanılarak gerçekleştirilmiştir. $\chi_{b1}(1P)\pi^+\pi^-$ ve $\Upsilon(1S)\pi^+\pi^-$ nihai durumları için dağılımları elde etmek üzere bu iki bozunma zinciri tamamen yapılandırılmıştır. χ_{b1} durumunun radyatif bozunma yoluyla yeniden yapılandırılmasıyla, CMS İzleyici malzemesinde dönüşerek yeniden yapılandırılan fotonların önemi gösterilmiştir. İki nihai durum ($\chi_{b1}(1P)\pi^+\pi^-$ ve $\Upsilon(1S)\pi^+\pi^-$) için elde edilen spektrumlar da, varsayımsal X_b egzotik durumu ile ilişkilendirilebilecek hiçbir önemli tepe yapısı rapor edilememiştir.

Anahtar Kelimeler: Egzotik hadronlar, X(3872), X_b, pp Çarpışmaları, CMS

EXTENDED ABSTRACT

Currently the Standard Model is the most established theory in Physics able to describe the nature of the elementary particles and their interactions. The elementary particles can be divided into four groups: 1) leptons, 2) quarks, 3) gauge bosons and 4) the Higgs boson. The last one has been discovered few years ago by the CMS (Compact Muon Solenoid) and ATLAS (A Toroidal LHC Apparatus) Collaborations at the Large Hadron Collider (LHC), that is the largest accelerator in the world, operating at the laboratories of European Nuclear Research Center (CERN) laboratories that encompasses the Swiss-French borders. Six different types of quarks have been discovered and they are named up, down, strange, charm, bottom/beauty and top/truth (u, d, s, c, b, t). The quarks, which are characterised by a fractional value of charge, have never been observed free, but they can group in order to build up particles, called hadrons. The easiest way in which hadrons can be a quarks compound, according to the Quantum Chromo-Dynamics (QCD) theory, is a quark-antiquark pair ($q\bar{q}$), namely a meson, or three quarks (qqq), called baryon. However the QCD foresees other hadronic structures, considered exotics, such as multiquarks, glueballs or hybrids. Possible configurations for multi-quark structures are tetraquarks (qq-$\bar{q}\bar{q}$), pentaquarks (qqq-qq) and dibaryons (six quarks or three quarks and three antiquarks). Glueballs are hadrons with valence gluons instead of valence quarks, whereas hybrids are hadrons that have both quarks and gluons as valence constituents (e.g. qqg). These possible configurations are - nowadays - searched for in the so-called hadron spectroscopy research field.

Since 2003, the hadron spectroscopy has experienced a renaissance thanks to the experimental findings at the B-factories and at the Hadron Colliders (initially at Tevatron and recently LHC). A new wide zoology of quarkonium-like states, many

of them with manifestly exotic characteristics (the so-called XYZ states), still needs to be interpreted within a consistent theoretical framework. About 30 states, mostly appearing to behave like heavy resonances, do not fit the charmonium ($c\bar{c}$) or bottomonium ($b\bar{b}$) spectra and show to be characterised by features that do not allow to describe them as ordinary mesons. The development of theoretical models is not yet able to provide an unified explanation of these states, even for the majority of them. For instance the nature of the X(3872) state, namely the first charmonium-like state to be discovered (in 2003) and then observed by many experiments (at B-factories and Hadron Colliders), is still unknown. The analyses of LHC Run-I data have contributed to carry out new experimental observations and measurements for exotic mesons. Among them it is worthy to mention the study of the inclusive prompt production characteristics of the X(3872) state and the search for its neutral bottomonium partner, with Run-I data, in the $\Upsilon(1S)\pi^+\pi^-$ final state.

With reference to the latter, Heavy Quark Symmetry considerations suggest the existence of a beauty partner of the X(3872), called X_b. In particular the hadronic molecular model suggests to search it. The strategy for X_b observation at the LHC experiments (in particular at CMS) with Run-II data should include its search in the $\chi_{b1}(1P)\pi^+\pi^-$ final state, where $\chi_{b1}(1P)$ is reconstructed in its decay to $\Upsilon(1S)$ plus a photon with $\Upsilon(1S)$ decaying into two muons ($\Upsilon(1S)\rightarrow \mu^+\mu^-$). The previous one is the most promising channel that can be carried out at CMS (as suggested by theorists Karliner and Rosner). Alternatively the $\Upsilon(1S)\pi^+\pi^-$ final state can be still explored (as done by CMS with Run-I data) since its reconstruction in the data is more efficient thus compensating the fact that the searched decay $X_b\rightarrow\Upsilon(1S)\pi^+\pi^-$ should be suppressed because of the implied G-parity symmetry violation. By exploiting the data collected during Run-II, CMS has the capability to reconstruct the aforementioned two final states and look for the X_b signal with enough experimental sensitivity. The purpose of the project is the inclusive search of the X_b particle in the $\chi_{b1}(1P)\pi^+\pi^-$ final state with the LHC Run-II data (2016-2018) collected by the CMS experiment. This research is important for the physics of hadrons, in particular the exotic ones, and can help sheding light on the way quark combines to build the particles and ultimately about how the matter can be intimately composed.

In this thesis, an analysis of $\Upsilon(1S)\pi^+\pi^-$ and $\chi_{b1}(1P)\pi^+\pi^-$ final states have been presented, with the purpose to search for the possible exotic X_b signal, by exploiting the nearly whole data sample collected during the Run-II data taking by the CMS experiment. Two decay chains were fully implemented and configured to obtain the distributions for the $\Upsilon(1S)\pi^+\pi^-$ and $\chi_{b1}(1P)\pi^+\pi^-$ final states.

As a consequence of these studies, the obtained spectra for the two final states ($\Upsilon(1S)\pi^+\pi^-$ and $\chi_{b1}(1P)\pi^+\pi^-$) allow reporting no significant peaking structure that could be associated to the hypothetical X_b exotic state. This result holds the amount of LHC Run-II data collected by the CMS experiment and its current sensitivity.

GENİŞLETİLMİŞ ÖZET

Standard Model (SM), temel parçacıkların doğasını ve etkileşimlerini tanımlayabilen fizikteki en yerleşik teoridir. Bu teori, üç etkileşimi tanımlar. Birincisi, elektrik ve manyetizmadan sorumlu "elektromanyetik etkileşim" ikincisi, radyoaktivitenin kökenindeki "zayıf etkileşim" ve üçüncüsü, hadronlarda kuarklar arasında etki yapan ve nükleonları atom çekirdeklerinde bir arada tutan "güçlü etkileşim"dir. SM'e göre temel parçacıklar dört gruba ayrılır: 1) leptonlar, 2) kuarklar, 3) ayar (gauge) bozonları ve 4) Higgs bozonu. Sonuncusu, birkaç yıl önce, İsviçre- Fransa sınırında bulunan Avrupa Nükleer Araştırma Merkezi (CERN) laboratuvarlarında faaliyet gösteren, dünyanın en büyük hızlandırıcısı olan Büyük Hadron Çarpıştırıcısı'ndaki (BHÇ) Kompakt Müon Selenoid (CMS) ve Trodial BHÇ Aparatı (ATLAS) işbirlikleri tarafından keşfedildi. Günümüze kadar altı farklı kuark türü keşfedildi ve bunlar yukarı (u), aşağı (d), garip (s), tılsım (c), alt/güzellik (b) ve üst/gerçek (t) olarak adlandırıldı.

Kesirli bir yük değeri ile karakterize edilen kuarklar hiçbir zaman serbest olarak gözlenmemiştir, ancak hadron adı verilen parçacıkları oluşturmak için gruplanabilirler. Kuantum Renk Dinamiği (QCD) teorisine göre hadronların bir kuark bileşiği olabilmesinin en kolay yolu, bir kuark-antikuark çifti ($q\bar{q}$) yani bir mezon ve baryon adı verilen üç kuarktır (qqq). Bununla birlikte, QCD, çoklu kuarklar (multiquarks), glueball'lar veya hibritler (hybrids) gibi ekzotik olarak kabul edilen diğer hadronik yapıları öngörür. Çoklu kuark yapıları için olası konfigürasyonlar tetrakuarklar (qq-$\bar{q}\bar{q}$), pentakuarklar (qqq-qq) ve dibaryonlardır (altı kuark veya üç kuark ve üç antikuark).Glueball'lar, değerlik kuarkları yerine valans gluonları olan hadronlardır, hibritler ise değerlik kurucuları olarak hem kuark hem de gluonlara sahip hadronlardır (örneğin qqg). Günümüzde bu olası konfigürasyonlar hadron spektroskopi olarak bilinen araştırma alanında aranmaktadır.

2003'ten beri hadron spektroskopisi B-fabrikalarında ve Hadron Çarpıştırıcılarındaki deneysel bulgular sayesinde bir rönesans yaşamıştır (başlangıçta Tevatron' da ve son zamanlarda BHÇ' de). Çoğu açık bir şekilde egzotik özelliklere sahip (XYZ durumları olarak adlandırılan) kuarkonyum benzeri durumların yeni bir geniş zoolojinin tutarlı bir teorik çerçevesi içinde yorumlanması gerekmektedir. Çoğunlukla ağır rezonanslar gibi davranan yaklaşık 60 durum charmonium ($c\bar{c}$) veya bottomonium ($b\bar{b}$) spektrumlarına uymaz ve sıradan mezonlar olarak tanımlamaya izin vermeyen özellikler ile karakterize edilir. Teorik modellerin gelişimi, bu durumların bir açıklamasını henüz çoğunluğu için sağlayamamıştır. Örneğin 2003 yılında ilk charmonium benzeri durum olarak keşfedilen ve daha sonra (B-fabrikaları ve Hadron çarpıştırıcılarındaki) birçok deneyde gözlemlenen X(3872) durumunun doğası hala bilinmemektedir. BHÇ Run-I verilerinin analizi, egzotik mezonlar için yeni deneysel gözlemler ve ölçümler yapmaya katkıda bulunmuştur. Bunların arasından, X(3872) durumunun üretim özelliklerinin çalışılması ve X(3872) durumunun nötr bottomonium ortağının Run-I verileriyle $\Upsilon(1S)\pi^+\pi^-$ son durumunda araştırılması bahsedilmeye değerdir.

Gerçekten de Ağır Quark Simetrisi (Heavy Quark Symmetry) ile ilgili düşünceler X(3872)'in X_b adlı bir güzellik (beauty) eşinin varlığını göstermektedir. Özellikle, hadronik moleküler model bunu araştırmayı önerir. BHÇ deneylerinde Run-II verileri ile (özellikle CMS'de) X_b'yi keşfetmek için kullanılacak strateji, $\chi_{b1}(1P)\pi^+\pi^-$ son durumunun araştırılmasını içermelidir. Burada $\chi_{b1}(1P)$, $\Upsilon(1S)$ ve iki zıt yüklü piona bozunumu ($X_b \to \Upsilon(1S)\pi^+\pi^-$) ile yeniden yapılandırılır, $\Upsilon(1S)$ ise iki müona bozunur ($\Upsilon(1S) \to \mu^+\mu^-$). Birincisi CMS' de araştırabilecek en umut verici kanaldır. Bozunumun kendisinin G-parite simetrisi tarafından bastırılmış olabilmesine rağmen yeniden yapılandırılması daha verimli olduğundan alternatif olarak, Run-

I verileriyle CMS' de yapıldığı gibi $\Upsilon(1S)\pi^+\pi^-$ son durumu hala araştırılabilir. CMS, Run-II sırasında toplanan verileri kullanarak, yukarıda bahsedilen iki son durumu yeniden oluşturma ve X_b sinyalini yeterli deneysel hassasiyetle arama yeteneğine sahiptir.

Bu çalışmanın amacı, CMS deneyi tarafından toplanan BHÇ Run-II (2016-2018) verileriyle $\chi_{b1}(1P)\pi^+\pi^-$ ve $\Upsilon(1S)\pi^+\pi^-$ son durumlarında X_b parçacığının kapsamlı bir şekilde araştırılmasıdır. Bu araştırma, hadronların fiziği, özellikle de egzotik olanlar için önemlidir ve kuarkların parçacıkları oluşturmak için bir araya gelme şekline ve - nihayetinde - maddenin nasıl oluşturulabileceğine ışık tutmaya yardımcı olabilir.

Bu çalışmada, olası egzotik X_b sinyalini aramak amacıyla $\chi_{b1}(1P)\pi^+\pi^-$ ve $\Upsilon(1S)\pi^+\pi^-$ nihai durumlarının analizi CMS deneyi tarafından Run-II verileri sırasında toplanan neredeyse tüm veri örneğinden yararlanılarak gerçekleştirilmiştir. $\chi_{b1}(1P)\pi^+\pi^-$ ve $\Upsilon(1S)\pi^+\pi^-$ nihai durumları için dağılımları elde etmek üzere bu iki bozunma zinciri tamamen yapılandırılmıştır.

Bu çalışmanın bir sonucu olarak, iki nihai durum ($\chi_{b1}(1P)\pi^+\pi^-$ ve $\Upsilon(1S)\pi^+\pi^-$) için elde edilen spektrumlarda, varsayımsal X_b egzotik durumu ile ilişkilendirilebilecek hiçbir önemli tepe yapısı rapor edilememiştir. Bu sonuç, CMS deneyi tarafından toplanan BHÇ Run-II verilerinin miktarı ve mevcut hassasiyeti göz önüne alındığında şaşırtıcı değildir.

ACKNOWLEDGEMENTS

The research study represented in this thesis would not have been possible without the support of many people. Thanking everyone who contributed not only to my academic but also to my personal growth during this time is almost impossible. But I will try to mention the most important persons here.

First of all, I would like to state my sincere gratitude to my advisor İsa Dumanoğlu for his continuous support, patience, and motivation. He has opened the door to me of a new world with a lot of opportunities. I am grateful to him for being my advisor.

I'm also grateful to Alexis Pompili for his support and guidance during my visit to University of Bari Aldo Moro in Italy. I would like to thank him and his group for all their help and contribution to my thesis. In addition, my sincere thanks to TUBITAK for funding me with 2214-A research scholarship program that enabled me to visit University of Bari Aldo Moro in Italy for this analysis work. I also would like to thank TENMAK for funding me for my CERN visits during my Ph.D.

I feel very lucky to have had the opportunity to meet and work with so many great scientists at CERN. I would like to thank all of the HCAL team for their cooperation during my Ph.D. Especially, I would like to express my deepest appreciation to Jay R. Dittmann for all of his guidance in my HCAL studies. I am grateful for his willingness to share knowledge and teach.

And I am extremely grateful to my big and amazing family for their unconditional love, support, and endless encouragement I have gotten over the years. I undoubtedly could not have done this without them.

CONTENTS **PAGE**

LIST OF TABLES **PAGE**

LIST OF FIGURES **PAGE**

ABBREVATIONS

ALICE	:	A Large Ion Collider Experiment
ASICs	:	Application-Spesific Integrated Circuits
ATLAS	:	A Toroidal LHC ApparatuS
BNL	:	Brookhaven National Laboratory
BPH	:	B-Physics
BPix	:	Pixel Detector Barrel Layers
CEM	:	Color Evaporation Model
CERN	:	European Organisation for Nuclear Research
CS	:	Color Singlet
CO	:	Color Octet
CMS	:	Compact Muon Selenoid
CSC	:	Cathode Stript Chambers
CSM	:	Color-Singlet Model
CV	:	Conversion Vertex
DT	:	Drift Tubes
DQM	:	Data Quality Monitoring
EB	:	ECAL Barrels
ECAL	:	Electromagnetic Calorimeter
EE	:	ECAL Endcaps
FPGAs	:	Fiels Programmable Gate Arrays
FPix	:	Pixel Detector Endcap Discs
GT	:	Global Trigger

HB	:	HCAL Barrel
HCAL	:	Hadronic Calorimeter
HE	:	HCAL Endcap
HF	:	HCAL Forward
HLT	:	High-Level Trigger
HO	:	HCAL Outer Barrel
ICEM	:	Improved Color Evaporation Model
IP	:	Interaction Point
LDMEs	:	Long-Distance Matrix Elements
LHCb	:	Large Hadron Collider beauty
LEP	:	Large Electron-Pozitron Collider
LHC	:	Large Hadronic Collider
LINAC2	:	Linear Accelerator 2
LO	:	Leading Order
LS	:	Long Shutdown
L1	:	Level-1 Trigger
MC	:	Monte Carlo
NLO	:	The First Next Leading Order
NNLO	:	The Next-to-Next-to Leading Order
NP	:	Non-Prompt
NRQCD	:	Non-Relativistic Quantum Chromodynamics
PAGs	:	Physics Analysis Groups

PDs	:	Primary Datasets
PR	:	Prompt
PS	:	Proton Synchroton
PU	:	Pile-Up
SLAC	:	Standford Linear Accelerator Complex
SM	:	Standard Model
SPS	:	Super Proton Synchroton
RPC	:	Resistive Plate Chambers
TEC	:	Tracer End Caps
TIB	:	Tracer Inner Barrel
TID	:	Tracer Inner Discs
TOB	:	Tracer Outer Barrel
QCD	:	Quantum Chromodynamics
QED	:	Quantum Electrodynamics

1. INTRODUCTION

The fundamentals of particle physics was established in the first half of the 20th century, and the first steps taken with the observation of an entirely new set of phenomena. These phenomena are the discovery of the positron which is the oppositely charged electron, observation of new particles with extraordinary properties in the cosmic rays, virtual particles in the vacuum, and the breaking of symmetries. Particle physics did not settle for observing natural phenomena during the development period. Accelerators were established to produce these new particles in a laboratory environment and examine their features remotely. At the end of 2009, LHC (the Large Hadron Collider), the world's largest and highest-energy particle accelerator, started its operations at the CERN (the European Organization for Nuclear Research) laboratories in Geneva. The purpose of this accelerator is to try to understand the nature of matter by searching for answers to some of the fundamental questions in physics concerning the basic laws governing the interactions and forces among the elementary particles. This enormous collider contains four significant experiments,CMS (Compact Muon Solenoid), ATLAS (A Toroidal LHC Apparatus), LHCb (Large Hadron Collider beauty) , and ALICE (A Large Ion Collider Experiment).

CMS is a general-purpose detector designed to investigate a large number of physical phenomena. It has a superconducting solenoid magnet with a field of 3.8 T which fields lets to an inner tracking detector to reconstruct the charged tracks and primary and secondary vertices with a high resolution, and with an efficient muon spectrometer located in the return yoke of the magnet which provides a very good reconstruction of muons with the help of the inner tracker.

After many revolutionary explorations in the last century, the current understanding of matter is contained in the Standard Model of particle physics. It explains all the fundamental structure of the matter known today. There are basic combinations in nature, but theoretically, it is possible to obtain new states that do not fit these basic structures. The development of theoretical models is not yet able to provide a unified explanation of most of these new states. For instance, the nature of the X(3872) state, namely the first charmonium-like state to be discovered and then observed by many experiments, is still unknown. The LHC Run-I and Run-II data analyses have contributed to carrying out new experimental observations and measurements for exotic mesons. Although LHCb is a dedicated experiment to contribute to this new spectroscopy, the CMS experiment has also provided some critical results in this field. Among them, it is crucial to study the production characteristics of the X(3872) state and to search of its neutral bottomonium partner with Run-I and Run-II data in the $\Upsilon(1S)\pi^+\pi^-$ and $\chi_{b1}(1P)\pi^+\pi^-$ final states. Indeed Heavy Quark Symmetry considerations suggest the existence of a beauty partner of the X(3872), called X_b.

This thesis presents an inclusive examination of the X_b particle, a beauty partner of the X(3872), using the data collected by the CMS experiment at LHC. This thesis organized as follows. Chapter 2 starts with the Standart Model, continues with the Quark Model and exotic hadrons and spectroscopy of them, finishes with a comprehensive review of the theoretical knowledge on X(3872) and X_b. Chapter 3 presents a general description of the experimental apparatus, the LHC accelerator and the CMS experiment. Chapter 4 represents the analysis strategy for $\Upsilon(1S)\pi^+\pi^-$ and $\chi_{b1}(1P)\pi^+\pi^-$ final states. While chapter 5 represents the analysis of the X_b decay to $\chi_{b1}(1P)\pi^+\pi^-$, chapter 6 represents the analysis of the X_b decay to $\Upsilon(1S)\pi^+\pi^-$ final state. Finally, the Conclusions chapter contains the summary of the obtained results and the prospects for future studies on the X_b with the CMS experiment.

2. THEOERICAL FUNDAMENTALS

2.1. The Standard Model of the Particle Physics

All the facts that have been observed so far in particle physics can be explained with a single theory called Standard Model (SM). This theory describes three fundamental interactions. The first is the “electromagnetic interaction” responsible for electricity and magnetism, and the second is the “weak interaction” at the root of radioactivity as well as the energy of the sun. Finally, the “strong interaction” holds together the quarks in hadrons and nucleons in the atomic nuclei.

The SM also defines the elementary particles that make up the matter. In the SM, there are two types of particles; Fermions and Bosons. Fermions called for their accordance to Fermi-Dirac statistics, carry half-integer spin, and are responsible for all known matter in the universe. Bosons, called for their accordance to Bose-Einstein statistics, carry integer spin and intervene the fundamental forces through emission and absorption by fermions.

Fermions are divided into two families: leptons and quarks. The charged leptons interact only through the electromagnetic and weak forces, and quarks also interact through the strong force. Additionally the leptons have three different types: the electron, the muon, and the tau, and their corresponding neutrinos interacts only through the weak force. There are three generation quarks, each consisting of an up-type: the up, the charm, the top, and a down-type: the down, the strange, and the bottom quark. Figure 2.1. shows fundamental particles and their interactions as described by the SM.

The SM, moreover, predicted the presence of the Higgs boson, which allows the intermediate vector bosons to gain mass as a result of the Higgs mechanism. In 2012, the discovery of the Higgs boson, the last missing part of SM (Georges Aad

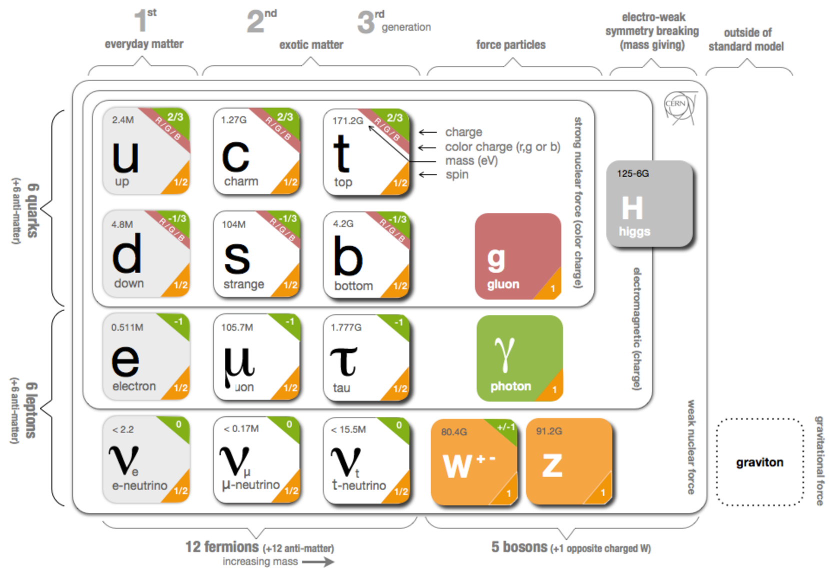

Figure 2.1. Particles and forces described by the SM (Purcell, 2012)

et al., 2012b) proved its great success in explaining the interactions of SM subatomic particles. Even if it is one of the most successful theoretical models in physics, SM is still regarded as a theory with many deficiencies. The most important of these deficiencies, the SM, does not include gravity, the fourth basic force. Another deficiency concerns the mass of the neutrinos. Neutrinos are massless in the SM; however, it has been understood that neutrinos have a mass by the observation of the neutrino oscillations (Ahmad et al., 2001). The other deficiency of the SM is the absence of a candidate for dark matter, which is predicted to exist from the observations such as gravitational lensing and the expected rotation curves of galaxies (Clowe et al., 2006). Mathematically, the SM is a quantum field theory based on the gauge symmetry of $SU(3) \times SU(2) \times U(1)$. The $SU(2) \times U(1)$ gauge symmetry is responsible for combining electromagnetic and weak force into the electroweak force mediated by the photon, the Z^0 and the $W^{\pm}$ bosons, respectively. An additional field has been added that allows the Z^0 and $W^{\pm}$ bosons which are manifested in the presence of the Higgs boson, to obtain a mass by the self-symmetry breaking mechanism (Higgs, 1964).

2.2. The Quantum Chromodynamics

The quantum field theory of strong interactions was formulated in 1973 (Fritzsch, 1977). This theory of quarks and gluons called Quantum Chromodynamics (QCD) is similar to Quantum Electrodynamics (QED). Similar to the single electric charge in QED, there are three color charges in QCD, which are the orthogonal states in the *SU(3)* color space, red, green, and blue. Just as the anti-particles carry an opposite electric charge in QED, the anti-quarks carry an opposite color charge in QCD. This theory explains the strong interaction between quarks and eight massless gluon fields. By the theory, quarks carrying a color charge are fundamental particles, and gluons existing as massless quanta are responsible for strong interactions. The strong force connects the quarks into nucleons and nucleons into atomic nuclei. Thus, it keeps all our visible world together at the innermost level. Even though the strong interaction dynamics is consistently defined in QCD, certain conditions are required for some perceptible calculations. This is related to the fact that gluons that mediate the strong force, themselves carry color charge and they are, so, self-interacting. The consequence of this is the phenomenon of asymptotic freedom which is represented by α_s, the strong coupling constant (Politzer, 1973). The expansion of α_s is limited due to perturbative QCD calculations in processes with high energies, containing high momentum transfers over short distances where α_s is small. In such scattering processes, the interaction between quarks and gluons is reduced. On the contrary, the interaction between the quarks and gluons is strengthened at low energy and long distances, that is, in the soft QCD field, and therefore the expansion is disturbed. This causes the phenomenon of quark confinement, which provides that only colored singlet states are visible. The hadrons are characterized by low momentum transfer (Brambilla, 2011) processes that lead to QCD bound states; for this reason, they cannot be easily accessed with perturbative QCD calculations. Nevertheless, this problem can be alleviated for the charm or bottom quarks, which are heavy quarks and shown as c and b, respectively.

2.3. Quarkonium

Quarkonium denotes the bound state comprised of a heavy quark and its antiquark by the strong interaction. These are particles called mesons, a subset of bosons made up of a connected pair of $q\bar{q}$ that may have different flavours. Depending on the flavour of the heavy quark, mesons are divided into two families, the charmonium family for $c\bar{c}$ states and the bottomonium family for $b\bar{b}$ states. Because of their heavy masses, top quarks do not form bound states because they decay electroweakly before a bound state can compose.

In 1974, the J/ψ was the first quarkonium state discovered at the Brookhaven National Laboratory (BNL) (Aubert et al., 1974) and the Stanford Linear Accelerator Complex (SLAC) (Augustin et al., 1974) almost at the same time. This newly found state was accepted as a bound state of $c\bar{c}$, which confirmed charm quark's existence (Glashow et al., 1975). The first observation of the $\Upsilon(1S)$, a particle with a bottom quark, was discovered only three years later. It was the first member of the bottomonium family (Herb et al., 1977).

2.4. Quarkonium Spectra

The charmonium and bottomonium family members happen in different quantum states. These quantum states are qualified by quantum numbers that define spin S, angular momentum L, total angular momentum $J = L + S$, and the principal quantum number n. There are different ways to define all possible configurations as J^{PC}, with parity $P = (-1)^{L+1}$ and charge conjugation $C = (-1)^{L+S}$. Moreover, using the so-called spectroscopic notation $n^{2S+1}L_J$ is another way.

There are two different categories in the spectra: *S-wave* states with $L = 0$ and P wave states with $L = 1$. The *S-wave* states are the $J^{PC} = 1^{--}$, vector mesons which are J/ψ and its radial excitation ϒ(2S) and the ϒ(1S) and its radial excitations ϒ(2S) and ϒ(3S). *S-wave* states are represented as ψ(nS) with *n = 1,2* in the charmonium family, while the bottomonium family is represented as ϒ(nS) with *n= 1, 2, 3*. *S-wave* states are the $J^{PC} = J^{++}$ pseudovector mesons which are χ_{cJ}(1P) and χ_{bJ}(1P) and its radial excitations χ_{bJ}(2P) and χ_{bJ}(3P), in triplets matching to *J = 0, 1, 2*. The charmonium and bottomonium states are shown in Figure 2.2. and 2.3.

In 2012 the χ_{bJ}(3P) state was discovered (Georges Aad et al., 2012a) and its triplet structure has been approved (Sirunyan et al., 2012) even though the generality of these defined states has been known for a long time. The dimuon channel, ψ(nS)→ $\mu^+\mu^-$ and ϒ(nS)→ $\mu^+\mu^-$, in the *S-wave* states, is the experimentally most important decay at hadron colliders. Generally, the *P-wave* states are reconstructed using their radiative decays from *S-wave* states which are χ_{bJ} →J/ψγ and χ_{bJ}(nS)→ ϒ(mS)γ. Before the decay, the quarkonium states travel just too small distances. Such decays are named prompt (PR). The *S-wave* and the *P-wave* quarkonium states have decay times in the order of 10^{-20}–10^{-21} and 10^{-22}–10^{-23} s, respectively. This too-short decay time makes it impossible to experimentally separate between directly produced quarkonia

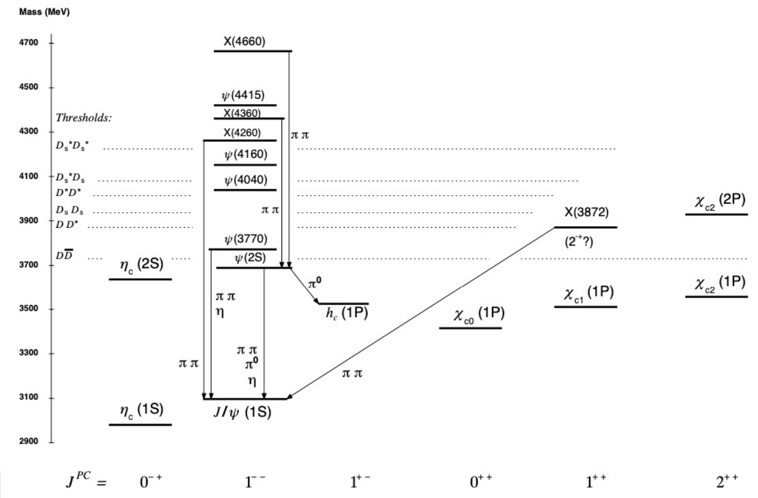

Figure 2.2. Charmonium spectrum (Tanabashi et al., 2018)

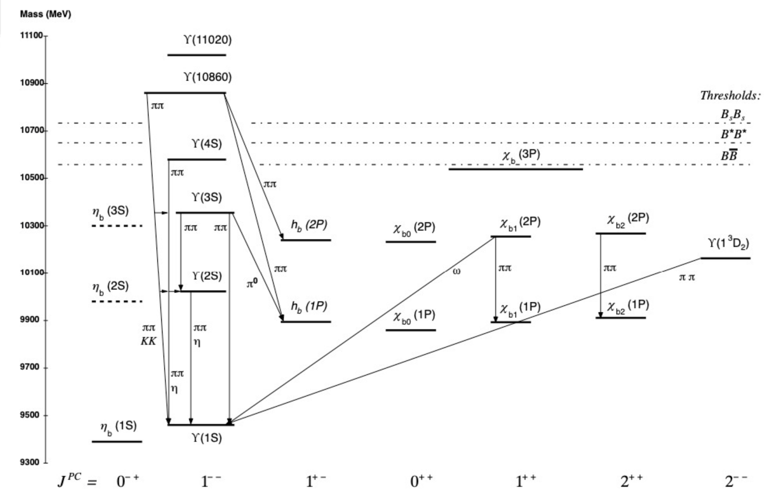

Figure 2.3. Bottomonium spectrum (Tanabashi et al., 2018)

and decay products of heavier quarkonium states named feed-down decays. Though it is theoretically possible to separate such feed-down decays by reconstructing all decay products of the heavier states from directly produced quarkonia, such a procedure is not possible in the hadron collisions. *P-wave* quarkonium states can provide identification in samples of softer *S-wave* states by adding photon in the dimuon final states and thus can reconstructing all the radiative decay of the *P-wave* quarkonia. In the charmonium system, it is also necessary to consider an additional component, called non-prompt (NP), which results from the decays of heavier b-hadrons. Nevertheless, these decays can be identified experimentally with the replacement of the secondary vertex, which is in the order of 100 μm, because the mean decay time is in the order of picoseconds (Tanabashi et al., 2018).

2.5. Quarkonium Production

Quarkonium production studies are an ideal laboratory for understanding QCD owing to the large masses of the participating quarks and the nature of the quark-antiquark system. A complete understanding of quarkonium production is important for understanding the hadron formation process in which the strong interaction binds quarks into hadronic bound states. Although sometimes some differences in the formation of the initial pair of $q\bar{q}$ are also presented (Andronic et al., 2016), the main differences between these two approaches are the second step which is called hadronization. When considered the huge masses of c and b-quarks, quarkonia can be acted as non-relativistic bound states because the relative $q\bar{q}$ velocity v in the bound quarkonium state is $v^2 \simeq 0.3$ and $v^2 \simeq 0.1$ for charmonium and bottomonium, respectively. Such non-relativistic states are described with three different real momentum scales, which are the heavy-quark mass, m_q, the momentum of the heavy-quark or antiquark in the quarkonium rest frame, $m_q v$, and the binding energy of the quark-antiquark pair,

$m_q v^2$ (Brambilla, 2011). The timescale is ∝ -$1/m_q$ to happens the production of the initial q$\bar{q}$ pair and it is $1/(m_q v^2)$ for the evolution into the physically observable bound state (Bodwin et al., 1995). The separation of the short distance and long-distance effects are dependent on the good separation of these two timescales. This situation is also well fulfilled in the bottomonium and charmonium systems. Nevertheless, this situation is different for soft hadrons; the production factor is broken since the time scales are not separated well. Because of this reason, quarkonium production studies provide important opportunities to study strong interactions involving long-distance, non-perturbative effects, and thus, to understand the hadron formation process.

The Non-Relativistic Quantum Chromodynamics (NRQCD) (ibid.) is the still common theoretical model for defining quarkonium production. The Color-Singlet Model (CSM) (Baier et al., 1983), the Color Evaporation Model (CEM) (Halzen et al., 1977) and the fragmentation function approach are among the other theoretical models for quarkonium production. The NRQCD will be described in detail in the following parts, and other models will only be briefly mentioned.

2.5.1. Non-Relativistic Quantum Chromodynamics

NRQCD is an effective field theory that allows the calculation of measurable observables, despite the importance of non-disturbing effects for the definition of quarkonium production, inspired by QCD. This theory defines two separate stages of quarkonium production. The first stage is the formation of an initial q$\bar{q}$ pair, and the second stage is the evolution of the initial q$\bar{q}$ pair into a bound quarkonium state. The initial q$\bar{q}$ pair, which is characterized by features depending on the production mechanism, such as different spins, angular momenta, and color eigenstates, is produced as a superposition of various resonant q$\bar{q}$ states. In the NRQCD factorization approach, the inclusive cross-section for the direct production of a quarkonium state H at large momentum transfer can be formulated as a sum of short-distance coefficients times NRQCD long-distance matrix elements (LDMEs) as follows (Brambilla, 2011):

$$\sigma(H) = \sum_n \sigma_n(\Lambda) \cdot \left\langle Q_n^H \right\rangle \tag{2.1}$$

Where Λ represents the ultraviolet part of the effective theory, the σ_n are expansions in powers of v of the cross-sections to produce a $q\bar{q}$ pair in the color, spin, and orbital-angular momentum state n (ibid.). This formula works on all potential $q\bar{q}$ states $\{n\}$, which including color singlet *(CS) (C = 1)* and color octet *(CO) (C = 8)* configurations. $\sigma_n(\Lambda)$ are the so-called short-distance coefficients and they define the production of the initial $q\bar{q}$ pair in a given quantum state $\{n\} = {}^{2S+1}L_J^{[C]}$, with the color multiplicity $C \in \{1,8\}$. The short-distance coefficients can be calculated using perturbative QCD methods, and they represent the inclusive partonic cross sections requisite to produce a $q\bar{q}$ state with quantum numbers $\{n\}$. As a consequence of this, different collision systems and energies are process-dependent and different. In general, a short-distance coefficient must not be singly observable; in case the sum over all partial cross-sections remains physically significant, it can even be negative. The Long Distance Matrix Elements (LDMEs), Q_n^H, is the evolution of the initial state with quantum numbers $\{n\}$ in a bound quarkonium state Q, which processes independent constant parameters that include all non-perturbative physics. Since LDMEs are independent of the energy, collision system, and $q\bar{q}$ kinematics, they are assumed to be universal constants in the NRQCD. They determine the importance of single $q\bar{q}$ states according to the entire quarkonium cross-section. The calculations of the LDMEs have to be estimated from fits to experimental measurements because it is not possible to perform within QCD (ibid.).

2.5.2. Color Singlet Model

For quarkonium production, the Color Singlet Model (CSM) was one of the first models put forward after the discovery of J/ψ. In this model, the quarkonium production process can be divided into two independent processes as the first generation of the $q\bar{q}$ pair, which takes place at short relative distances that can be calculated with the perturbative QCD, and the formation of the $q\bar{q}$ pair into a bound state, which is a low energy non-perturbative process. Until the early 1990s, when the experimentally measured cross-sections appeared to be much higher than predicted, CSM has been considered as a very well-defined model of quarkonium production (Baier et al., 1983). The CSM is a model that has not any free parameters, so the CS LDMs can be calculated theoretically and fixed with measurements of the decay rates of the quarkonium states. At higher energies, the first next-to-leading order (NLO) and next-to-next-to-leading order (NNLO) calculations in the α_s revealed that these additives are dramatically more significant than the ones in leading order (LO) (Brambilla, 2011). Although this has somehow revived the possibility of CSM defining important production mechanisms, it is not apparent that the expansion in α_s converges. In addition to all of these issues, CSM shows discrepancy, in the definition of *P-wave* quarkonium production, which can only be compensated by taking into account the CO terms in the NRQCD factorization method (ibid.).

2.5.3. Color Evaporation Model

The Color Evaporation Model (CEM) is another early model proposed in the late 1970s (Abe et al., 1997), trying to explain the production of quarkonium, such as CSM. Moreover, like CSM, CEM had quite a success in explaining measurements until the mid-1990s, when the conflict had occurred at higher collision energies. The basis of this model is the quark-hadron duality principle (Fritzsch, 1977). According to this principle, the production cross-section of a quarkonium state is straightly concerned with the producing of a $q\bar{q}$ pair in a mass field which allows evolution into a bound quarkonium state. The main difference is that the initial production of the $q\bar{q}$ pair in CEM can be produced in a colored state and, in some versions of the theory, a spin state. Unlike the quarkonium state, it will finally form through several non-perturbative emissions of soft gluons, which is the base of the term “color evaporation”. Since these soft gluon interactions are assumed to have a negligible effect on the kinematics of the $q\bar{q}$ pair, each heavy $q\bar{q}$ pair with an invariant mass below the open-flavour threshold will form some quarkonium state in CEM. Even though CEM has some success in phenomenological approaches, it has some inconsistencies in transverse momentum spectra, and most importantly, there is no way to explain quarkonium polarization. Nevertheless, some of these questions have lately received some attention within the framework of an improved CEM (ICEM) that addresses some of these questions and also includes the possibility of explaining quarkonium polarization (Ma et al., 2016).

2.5.4. The Fragmentation Function Approach

The new improvements in the theoretical definition of general quarkonium production have been called the fragmentation function approach (Nayak et al., 2005). The cross-section for quarkonium production with $p_T \gg m_q$ is defined as the sum of single-parton production cross-sections with single-parton fragmentation functions (Collins et al., 1982). Thus, all information about the new-coming state is included in the parton production cross-section. The probability distributions of the evolution of a $q\bar{q}$ pair in a quarkonium state defined by the parton fragmentation functions. The fragmentation function approach might provide a more convenient way than the organization in the NRQCD which organize contributions to the quarkonium production cross-section as a function of $m_q/\ p_T$. With the assumption that NRQCD factorization is valid, it is also the first step to prove NRQCD factorization by providing a way to express the fragmentation function as the sum of NRQCD LDMEs.

2.6. Bottomonium Production in b-Hadron Decays

In hadronic collisions, the decays of hadrons containing the B quark provide an important contribution to the production of charmonium. There are no similar processes that contribute to the production of bottomonium due to the absence of hadrons containing large mass top quarks. In high-energy hadron colliders, bottom quarks, and hence b-hadrons are produced abundantly. Generally, b-hadrons such as $B^{\pm}$, B^0, B_s^0, and Λ_b are produced with excited $B^{\star}$ states, which decay into these states in $p\bar{p}$ collisions. Then they decay into final states related to charmonium. Bottomonium production is examined with the Υ(nS) and χ_b(nP) states at hadron colliders. From these two states, the Υ(nS) states are the most studied. The feed-down additions to the Υ(1S) cross-section contain additions from the radiative decays of all the χ_b states and the hadronic decays of the Υ(2S, 3S) states, thus are complicated. The fraction of Υ(nS) (n = 1,2,3) produced has been measured in $p\bar{p}$ collisions, at center-of-mass energies of 7 TeV (Khachatryan et al., 2015). For the prompt χ_b(nP) cross-sections the feed-down contributions are the radiative decays $\Upsilon(nS) \rightarrow \chi_b((n-1)P)\gamma$. The direct fractions of prompt χ_{bJ}(nP) (J = 1, 2 and n = 1, 2) production has been measured in $p\bar{p}$ collisions, at center-of-mass energies of 8 TeV (Aaij et al., 2014).

2.7. Quarkonium Polarization

The polarisation or the spin alignment of a particle can be described as its preferred production with a particular subset of angular momentum eigenstates J_z throughout a given quantization axis from a superposition of different production mechanisms. The different contributions with different quantum numbers to the total cross-section cannot be measured one by one, but results about the features of the first pair of $q\bar{q}$ can be obtained by measuring one of the variables. The alignment of the total angular momentum vector J can be measured relative to a quantization *axis* z. The *S-wave* quarkonia vector mesons with J = 1 can be observed in three likely eigenstates of the angular momentum component $J_z = 0, \pm 1$ relative to a quantization *axis z*.

$$|Q\rangle = a_{+1}\,|+1\rangle + a_{-1}\,|-1\rangle + a_0\,|0\rangle \tag{2.2}$$

Equation 2.2 (Faccioli et al., 2010) describes *S-wave* quarkonium state as a superposition of the three eigenstates where a_i, for $i \in \{+1, -1, 0\}$, are the amplitudes of the separate components. In order to be able to say that a quarkonium is unpolarized, the probability of having a quarkonium state H in a given J_z eigenstate must be the same as all possible values of J_z. When the $J_z = \pm 1$ or the $J_z = 0$ eigenstates are used, the quarkonium is called transversely or longitudinally polarized, respectively. For instance, for the ψ mesons, in NRQCD, the color-octet components are expected to possess production through gluon fragmentation processes at higher energies, and this causes an expected strong transverse polarization $J_z = \pm 1$ but the CSM foresee strong longitudinal polarization $J_z = 0$ (Baier et al., 1983). Measuring the angular distribution needs defining a reference frame in the quarkonium rest frame relative to which the momentum of one of the decay products can be denoted. Figure 2.4.

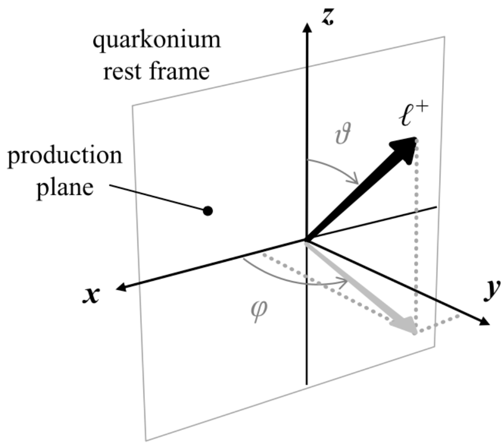

Figure 2.4. The coordinate system used to describe the polar angle θ and the azimuthal angle Φ of the positively charged lepton ℓ^+, here a μ^+, with respect to a quantization *axis z* (Faccioli et al., 2010)

represents how the polar angle θ and the azimuthal angle Φ of the positively charged lepton are defined.

While the *x-z plane* of the reference frame is designated by the production plane, which is extended by the momenta of the colliding beams *b*1 and *b*2, the *y-axis* is defined to be orthogonal to the production plane in the direction of $b1 \times b2$ as observed in the quarkonium rest frame. The direction of the *z-axis* is determined using different conventions to make the definition a perfect reference frame.

2.8. Hadrons

The strong interaction through a gauge symmetry is explained in QCD by the SM. QCD is in some way an excellent theory, but physicists cannot claim any definite tests of it that are comparable to those in the electroweak sector. While it is excellent in terms of validity in all energies as far as is known, it is quite difficult to use

QCD to make predictions for a wide variety of phenomena observed at low energies. This puzzle is related to the great value of the QCD's strong interaction. Interactions between particles that sense this strong interaction produce bound states, that is, hadrons. While these hadrons can be observed in particle detectors, their quarks components are never directly observed due to a feature called confinement (Cowan et al., 2018).

There are other approaches that allow theoretical estimates to be made even though the methods that allow definite tests of QED cannot be applied to QCD at low energies. Identifying an empirically limiting QCD potential is a simple but effective method. The technique of lattice QCD, which comprises formulating the theory in separate points on a four-dimensional (space and time) system and then using powerful supercomputers to calculate quantities of interest, is another more sophisticated approach. This approach, which was introduced in the 1970s (Fritzsch, 1977), has been continually improved since then with increased computing power. With this advance of the lattice QCD, the comparison of its estimates with the measurements has become highly insightful. Although the lattice QCD is promising to solve the unsustainability of the QCD calculations, it still needs to obtain the computational power required to accomplish this. In theoretical models, what will be taken as a result is mostly related to what is added to the model. In theoretical physics, this is named the choice of operators to include. Making lattice QCD estimates of the exotic hadron spectrum is all about deciding whether to include operators for quarks, the building blocks of hadrons (Cowan et al., 2018).

As mentioned in section 2.2., the QCD theory specifies that each quark can be in one of three different states, colored red, green and blue *(r, g, b)*. The combination of r+g+b is named colourless because the colours cancel themselves out. Antiquarks carry anticolour ($\bar{r}$, $\bar{g}$, $\bar{b}$), and colour + anticolour, e.i., $r + \bar{r}$, is also colourless. So, $\bar{r}$

is equal to g+b, and suchlike. The gauge bosons of QCD, gluons, also carry colour in one of eight possible combinations, e.i., r+$\bar{g}$. These colours allowing them to interact with quarks and themselves (see Figure 2.5.).

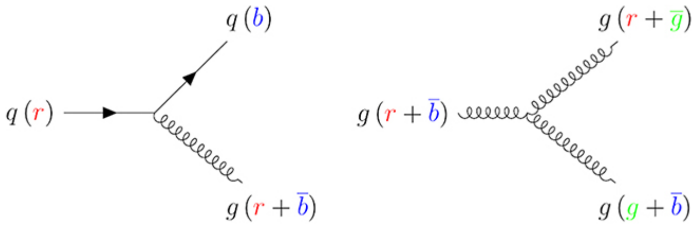

Figure 2.5. Feynman diagrams of the qqg and ggg interactions in QCD (Cowan et al., 2018)

Hadrons can be observed with only colorless combinations, and this allows some simple estimations. The simplest colorless combinations are meson ($q\bar{q}$) and baryon (qqq). The spectra of mesons and baryons can be predicted based on six different types, or flavours, of quark. The ω^{-} baryon was predicted by this way at a time when only the three lightest quark flavours - up, down, and strange - were known. Moreover, in 1964, the experimental confirmation of this baryon was critical in the development of QCD (Cowan et al., 2018). In the 1970s, the charm and beauty quarks were discovered in their quark-antiquark meson states, the J/ψ (Aubert et al., 1974) and Υ (Herb et al., 1977) particles respectively. And these discoveries were leading to the acceptance of the quark model (Cowan et al., 2018).

2.8.1. Exotic Hadrons

Possible colorless combinations of quarks and gluons are not just mesons and baryons. The tetraquarks, including two quarks and two antiquarks, and pentaquarks, including four quarks and one antiquark (or four antiquarks and one quark), are other possibilities (Figure 2.6.). Gluons can also form a colorless object called a glueball, including two or three gluons. In addition, hybrid states, which are some mixture of hadron and glueball, are also possible. According to the QCD, these exotic hadron types are likely to be produced in particle physics experiments. Until 2003, for exotic hadrons, there was no clear evidence. However, since then, hadron spectroscopy has experienced a revolution with the observation of new hadronic states, which indicate that they have combinations containing exotic hadron features (Cowan et al., 2018).

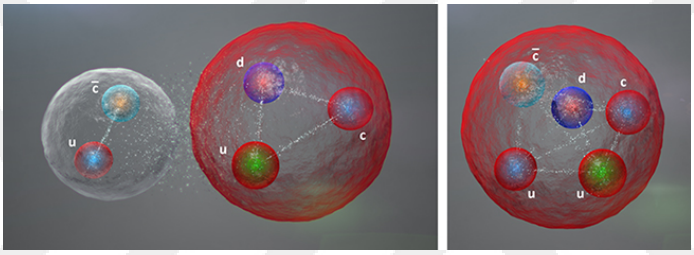

Figure 2.6. Possible quark combinations to make mesons, baryons and pentaquarks (Cowan et al., 2018)

2.8.2. Spectroscopy of Exotic Hadrons

While the components of the hadrons can never be observed, how is it determined whether a particle observed in the experiment is a traditional meson or baryon rather than an exotic hadron? The answer to this question is about the quantum numbers of hadrons that are used to classify them. These numbers are a set of key features that discriminate different types of particles (ibid.). For example, the total angular momentum J and parity P quantum numbers indicate how the wave function of particle proceeds when all spatial coordinates are inverted. When taking into account a quark-antiquark system, i.e., a meson, quarks are spin-1/2 particles, and hence if the orbital angular momentum L does not exist between them, the total angular momentum is equal to the internal spin S. And S is zero if the spins are anti-aligned or one if the spins are aligned. Particle and antiparticle have opposite parity is an essential feature of fermions, and so $P=-$ (Cowan et al., 2018). Therefore, the possible spin and parity quantum numbers are $J^P = 0^-$ and 1^-, which are called pseudoscalar and vector, respectively. But, in the case of one unit of orbital angular momentum between quark and antiquark, the total spin has three possible values, according to the rule for adding angular momentum in quantum mechanics $J = L \oplus S$. The four states with $J = 0^+$, 1^+, 1^+, 2^+ are the results of this. Higher spin states have higher energy and therefore higher mass, so a different pattern of states can be predicted. Whether the observed particle is exotic or not can be determined by whether it fits into this pattern (ibid.). If the particle does not fit into this pattern, that could be a sign of its exotic nature. Based on how the wave function behaves when all particles are replaced with antiparticles, C can be either + or –, like P. If a particle is an eigenstate of charge conjugation, that is, its own antiparticle, the quantum number C can be well-defined. For this reason, among hadrons, C only applies to mesons with quark and antiquark have the same flavour, usually called “onia” in case of heavy quarks, c, and b (ibid.). The rule that associates C with total spin is $C = (-)^{L+S}$. Whereas the $L = 0$ states have $J^{PC} = 0^{-+}$ and 1^{--}, the orbitally-excited states are 0^{++}, 1^{++}, 1^{+-} and 2^{++} for onia. These six combinations refer to particles known as η_c, J/ψ, χ_{c0}, χ_{c1}, h_c, and χ_{c2} respectively, in charmonia. In bottomonia, these six combinations refer to particles known as η_c, Υ, χ_{b0}, χ_{b1}, h_b, and χ_{b2} respectively. The characteristics of all hadrons referred to throughout this section are summarized in Table 2.1..

$n^{2S+1} L^J$ is sometimes used as another type of labeling. Here the notation *S, P, D, F* is used to correspond to orbital angular momentum values L= 0, 1, 2, 3, respectively. With this layout, the same six charmonia states with the principal quantum number n = 1, n = 2 are $^1S_0$, $^3S_1$, $^3P_0$, $^3P_1$, $^1P_1$, $^3P_2$. These are sometimes referred to with notations like ψ(2S) or ψ(3686), where the values in parentheses are the nL quantum numbers and the mass in units of MeV, respectively. This notation is generally used for open flavour hadrons which include quark and antiquark of different flavours, like mesons.

Particle ($J^{P(C)}$)	Typical mass (GeV)	Quark content
π^+, π^-, $\eta(0^{-(+)})$	0.14(π), 0.15(η)	$u\bar{d}$, $u\bar{u} - d\bar{d}$, $u\bar{u} + d\bar{d}$
ρ^+, ρ^0, $\omega(1^{-(-)})$	0.78	$u\bar{d}$, $u\bar{u} - d\bar{d}$, $u\bar{u} + d\bar{d}$
p, n(1/2)	0.94	uud,udd
K^+, $K^0(0^-)$	0.50	$u\bar{s}$, $d\bar{s}$
K^{*+}, K^{*0} (1^-)	0.89	$u\bar{s}$, $d\bar{s}$
$\Lambda(1/2^+)$	1.1	uds, usc, dsc
D^+, D^0, D_s^+ (0^-)	1.9	$c\bar{d}$, $c\bar{u}$, $c\bar{s}$
D^{*+}, D^{*0}, D_s^{*+} (1^-)	2.0	$c\bar{d}$, $c\bar{u}$, $c\bar{s}$
Λ_c^+, Ξ_c^+, Ξ_c^0 $(1/2^+)$	2.3 - 2.5	udc, usc, dsc
η_c, J/ψ, χ_{c0}, χ_{c1}, h_c, χ_{c2}	2.3 - 2.5	$c\bar{c}$
B^+, B^0, B_s^0 (0^-)	5.3	$u\bar{b}$, $d\bar{b}$, $s\bar{b}$
Λ_b^0, Ξ_b^0, Ξ_b^- $(1/2^+)$	5.6 - 5.8	udb, usb, dsb
η_c, Υ, χ_{b0}, χ_{b1}, h_b, χ_{b2}	9.4 - 9.9	$b\bar{b}$

Table 2.1. Conventional mesons and baryons referred to in this section (Cowan et al., 2018)

As explained above, to understand the quark content and build their nature as exotic or traditional states, it is necessary to determine the quantum numbers of hadrons. For instance, certain combinations of *J, P* and *C* cannot be created with quark-antiquark mesons, and therefore, these are exotic, which contain 0^{--}, 0^{+-} and 1^{-+}. Quantum numbers can also be measured by examining how a particle is produced. Alternatively, *J, P,* and *C* can be measured by what the particle decays to as well because all of them are conserved in both strong and electromagnetic interactions. So that, with known *P* and *C* values, the properties of the decaying hadron, the final state of a strong or electromagnetic decay can be explained (Cowan et al., 2018). The weak decays are easily identified, even if the interaction of both *P* and *C* quantum numbers is violated in the weak interaction. Because much smaller interaction strength means that they only occur when another decay is not possible, this provides measurable long lifetimes. It is valid for every open flavour hadron because the weak interaction is the just force in the SM that allows quark flavour changes. The clear flavour appeal and beauty hadrons are given in Table 2.1. have a life of $10^{-12}s$ and strange hadrons have lifetimes up to around $10^{-8}s$. Exotic hadrons can also be identified by using the conservation of quark flavour. For example, whether a meson is neutral can be understood from its containing a charm quark-antiquark pair. Thus, it can be understood whether a hadron could not be a traditional meson if it decays strongly to a final state containing a J/ψ meson plus another charged particle (ibid.).

The studies of hadrons containing charm and beauty quarks which are named heavy flavours, are twice as advantageous as light quark hadrons to understand QCD (ibid.). Because the light-quark hadrons are simpler and more reliable to make the theoretical calculations to estimate the spectrum of expected states by using well-understood tools such as non-relativistic quantum mechanics and lattice QCD (ibid.). Moreover, this makes the theory a guide to where experiments should research for resonances (ibid.). Another reason is that heavy-quark hadrons often decay to final states with leptons, and these final states are ideal for experimental detection.

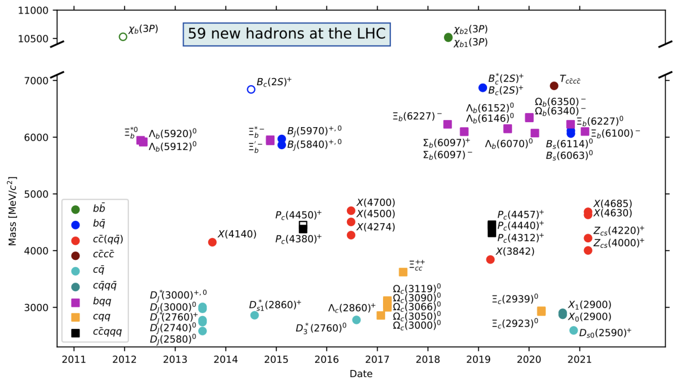

Figure 2.7. The diagram of new 59 hadrons found at the LHC last ten years (LHCb Collaboration, 2021)

The search for exotic hadrons, such as tetraquarks and pentaquarks, has a history with ups and downs based on the new experimental developments. The capacity of accelerators and detectors has increased significantly, over the past years. In the 50th anniversary of hadron colliders at CERN, a full list of the 59 new hadrons found at the LHC has been published. Some of these particles are pentaquarks, some are tetraquarks, and some are new high-energy (excited) states of baryons and mesons (Piotr, 2021). Figure 2.7. shows the diagram of new hadrons found at the LHC during the last ten years. The diagram includes the first hadron discovered at the LHC, $\chi_b(3P)$, which was discovered by ATLAS (Georges Aad et al., 2012a), and the most recent ones include a new excited beauty strange baryon observed by CMS (CMS Collaboration, 2021) and four tetraquarks detected by LHCb (LHCb Collaboration, 2021). The discovery of these new particles, along with measurements of their properties, continues to provide important information for testing the boundaries of the quark model.

2.8.3. Discovery of the Exotic Meson X(3872)

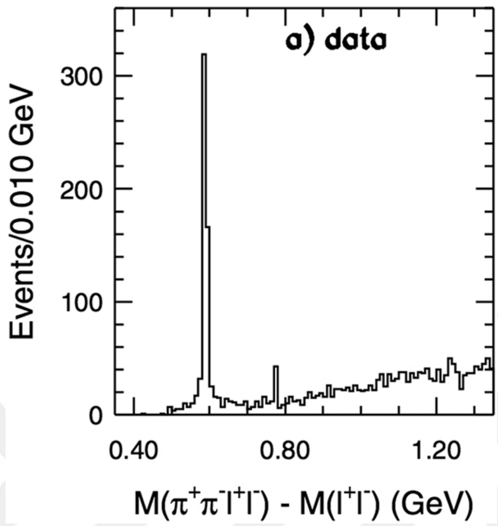

Figure 2.8. Distribution of the difference between $\pi^+\pi^-\ell^+\ell^-$ and $\ell^+\ell^-$ invariant masses of $B^+ \to J/\psi\pi^+\pi^-K^+$ candidates (Cowan et al., 2018)

In 2003, the observation of a particle named X(3872) led to the beginning of the current era of exotic hadron studies (Belle Collaboration, 2003). The Belle experiment, when studying the $J/\psi\pi^+\pi^-$ invariant mass spectrum of B^+ mesons decaying to $J/\psi\pi^+\pi^-K^+$, has made this discovery. Figure 2.8. shows the original Belle experiment result. This distribution shows the very clear signature of the well-known $\psi(2S)$ meson as well as an unexpected second narrow peak. This designates there is another resonance that decays to the same final state, $J/\psi\pi^+\pi^-$ (Cowan et al., 2018).

Many exotic hadron observations have a feature that they are seen by only one experiment and/or in only one decay mode. But this is positively different for the X(3872). Because shortly after its discovery by Belle, it was confirmed by the BaBar experiment and also observed to be produced in $p\bar{p}$ collisions by the CDF and D0 experiments (Cowan et al., 2018). The ATLAS, CMS, and LHCb experiments have been measuring its production rate in pp collisions not long after the LHC began operating. The riches of these new and quite enigmatical data aroused great interest in the particle physics community. In the final results with precise measurement, the X(3872) mass is 3871.69 $\pm$ 0.17 MeV, and its quantum numbers are determined as $J^{PC} = 1^{++}$ (ibid.). It is the most studied exotic hadron, but still, its true nature remains a mystery. When looking at the detailed analysis of the discovery decay mode X(3872)$\rightarrow$J/ $\psi\pi^+\pi^-$, it can be understood the $\pi^+\pi^-$ pair comes predominantly from the ρ^0 meson. And it shows the violation of isospin symmetry that is not expected for a traditional charmonium meson. Thus, if it is not a traditional $c\bar{c}$ state, it would be composed of two quarks and two antiquarks ($c\bar{c}u\bar{u}$) and produced in B decay. Based on the popular hypothesis, just as the deuteron is considered to be a bound state of a proton and neutron, it is a molecule of D^0 and $\bar{D}^{*0}$ mesons bound together by pion exchange. This also clarifies the observed isospin violation (ibid.). The mass of X(3872) is right at the threshold to make a D^0–$\bar{D}^{*0}$ pair, which is barely but considerably below the corresponding threshold involving charged D mesons. Another explanation is that X(3872) can be a heavy tetraquark (ibid.). The tetraquark with quarks and antiquarks firmly bound into a colour singlet object by diquarks (cu)($\bar{c}\bar{u}$). This explanation allows decay to $J/\psi\rho^0$. But $J/\psi\rho^0$ should decay to $J/\psi\rho^+$ that have not yet been observed (ibid.). The diquark models are described as the quark pairs to hold together to form a single object which interacts with the third quark in a baryon or an anti-diquark in a tetraquark via gluon exchange (ibid.).

2.9. Current Models of Diquarks

2.9.1. Tetraquarks

There is strong evidence about the exotic nature of the X(3872), but still, it is not easy to ultimately reduce the likelihood of being related to traditional charmonia. A signature is necessary to ensure the existence of exotic hadrons. This is possible by a charged charmonium-like resonance (Cowan et al., 2018). The $Z(4430)^-$ state, which is the first of which to be discovered as a peak in the invariant mass of $\psi(2S)\pi^-$ combinations found in the decays of B mesons: $B^0 \rightarrow \psi(2S)K^+\pi^-$ with $\psi(2S) \rightarrow \mu^+\mu^-$ by Belle (Choi et al., 2007). However, the first claims of discovery was not accepted universally. Although the BaBar experiment analyzed a similarly-sized dataset with the Belle, it has not found any evidence for contributions from exotic hadrons. Because various K states with different spins can contribute, a complicated interference pattern that could fake a peak in $\psi(2S)\pi^-$ invariant mass may appear (Cowan et al., 2018). In 2014, the LHCb released results based on a sample of B-meson decays that larger than those available to Belle and BaBar. The LHCb physicists did not only control the $\psi(2S)\pi^-$ invariant mass, but also they improved an amplitude model which made use of the complete kinematic information available in the $B^0 \rightarrow \psi(2S)K^+\pi^-$ decay. This provided to increase the sensitivity of their data analysis to exotic hadron contributions. Based on this model, a three-body decay containing only spin-0 particles indicates that only two variables are required to precisely define the decay system through the conservation of energy-momentum (ibid.).

Figure 2.9. (right) displays the results for the six complex numbers obtained from a fit, plotted in the Argand plane for values of $m(\psi(2S)\pi^-)^2$ increasing along the line from the topmost point. The red line shows the expectation for a Breit-Wigner

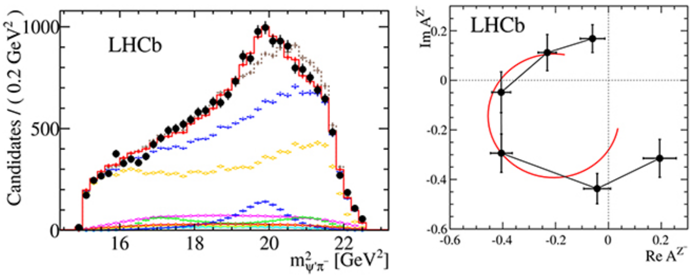

Figure 2.9. Squared invariant mass spectrum of $\psi(2S)\pi^-$ combinations in $B^0 \to \psi(2S)K^+\pi^-$ decays (left) and (right) the data points show the variation of the $Z(4430)^-$ decay rate in the Argand plane, displaying the characteristic circular behaviour of a resonance (Cowan et al., 2018)

amplitude which matches the data well. Moreover, this red line strongly supports the hypothesis that the $Z(4430)^-$ is a resonant state. After this analysis, it seems clear that the $Z(4430)^-$ must be exotic with a minimal quark content of $c\bar{c}\,d\bar{u}$ (Cowan et al., 2018). However, still, the big question does exist that waiting for the answer about its internal structure. For the answer to this big question, observations of the same state in different decay modes can provide useful information (ibid.).

A lot of other neutral and charged tetraquark-like states have been observed. Nevertheless, these states have not yet to be observed in the decays of b-quark hadrons. Although important experimental information about $Z(3900)^{\pm}$ states is collected, there are contradictory theoretical models related to the molecules of their open-charm mesons, combinations of tightly bound diquarks, or some effect of the decay kinematics and nearness open-charm threshold. When these are taken into account, it is clear that the X(3872), $Z(3900)^{\pm}$, and $Z(4430)^-$ states, which are intensely studied, are the exception rather than the rule in this new era of exotic spectroscopy (ibid.). But still, observation of new exotic hadrons is promising for understanding exotic hadron spectroscopy. Among them, it is good to mention the very recent first observation of the decay $B_0^s \to X(3872)\phi$, the study of the inclusive production characteristics of the X(3872) state and the search of its neutral bottomonium partner in the $\Upsilon(1S)\pi^+\pi^-$ final state by CMS experiment (CMS Collaboration, 2020). Furthermore, this observation may shed new light on the nature of the X(3872) particle.

2.9.2. Pentaquarks

The pentaquark states have been investigated for more than fifty years. In 2015, the LHCb experiment revealed the claim of a heavy charmonium pentaquark that contributed to the $\Lambda_b^0 \rightarrow J/\psi p K^-$ disruption (LHCb Collaboration, 2016). This process includes additions from many traditional excited Λ^* baryons with quark content uds. Moreover, these baryons decay to pK^-, which interference could potentially cause fake signals. However, as seen in Figure 2.10., in the invariant mass of the $J/\psi p$ system, there is a clear sign of a narrow peak around 4.4 GeV. It could be due to a charged resonance with minimal quark content $uudc\bar{c}$ (Cowan et al., 2018).

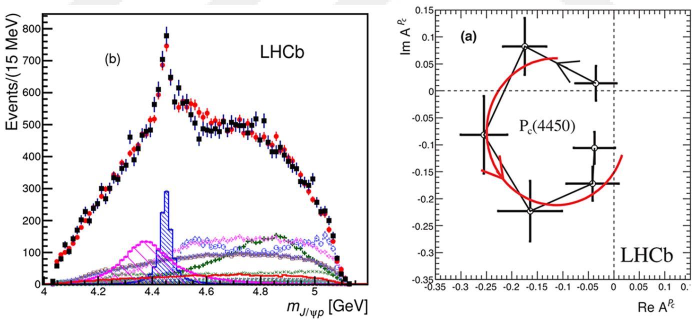

Figure 2.10. Squared invariant mass spectrum of $J/\psi p$ combinations in $\Lambda_b^0 \rightarrow J/\psi p K^-$ decays (left) and (right) the Argand diagram of the P_c $(4450)^+$ state (Cowan et al., 2018)

LHCb physicists already experienced from the study of the Z(4430) state in the $B^0 \rightarrow \psi(2S)K^+\pi^-$ process. Based on this study, they made a multidimensional amplitude model that fit the data to approve this pentaquark hypothesis. When they added the two exotic $P_c^0 \to J/\psi p$ components, they had obtained satisfactory fits. These two states are needed, at high statistical significance, to define the data. In this diagram is seen the expected resonant behavior is seen (Cowan et al., 2018).

2.9.3. Doubly Heavy Baryons

There are major uncertainties associated with theoretical estimates for their mass in different models for exotic hadrons. Actually, this is only one of the difficulties of interpreting the data on them. Therefore, studies of conventional hadrons will be important to ensure progress that can help reduce these uncertainties. The doubly heavy baryons that have two heavy quarks are a particularly curious field. The modeling of baryons with three light quarks suffers from the three-body problem that is common with classical gravity but in the doubly heavy systems are much simpler to define as the two heavy quarks are almost stable at the center of the baryon, with the lighter quark orbiting around them. This simplifies estimations in many theoretical approaches, especially in diquark models. In this model, it would be considered a double charm baryon consisting of [cc]u, [cc]d, or [cc]s will be considered (ibid.).

There was no obvious observation for the doubly heavy baryons until the first report about them came from the SELEX experiment at Fermilab (SELEX Collaboration, 2002). A signal of the Ξ_{cc}^{+}(ccd) state was reported but the properties that were very different from the expectations. Because of that, it was not confirmed by any other experiment. And so, it remained uncertain if it was truly a doubly heavy baryon. After the LHC produces large quantities of all species of hadrons, there was a good opportunity to clarify this situation. But the uncertainty of this situation remained since the production of doubly heavy systems requires both heavy quarks to be produced kinematically close to each other; in this way, they can bind and hadronize. And it is leading to large uncertainties on the production rates. However, the Tevatron and LHC had been observed the B_c^+ (c $\bar{b}$) meson, containing the heavy c and anti-b quarks, and this lead to some optimism about the observation of the doubly heavy baryons (Cowan et al., 2018).

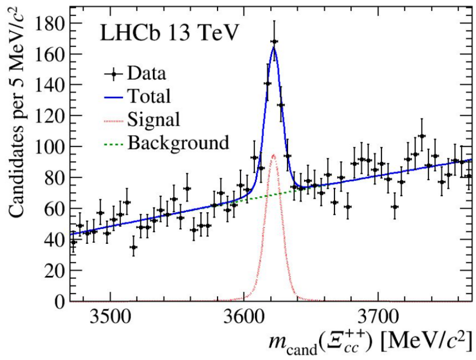

Figure 2.11. The signal for a double-charm baryon emerges from the invariant mass distribution of candidates obtained from data collected by the LHCb experiment (Cowan et al., 2018)

In Figure 2.11. is given the result of an analysis by LHCb searching for the doubly charged Ξ_{cc}^{++} (ccu) state through its decay to $\Lambda_c^+ K^- \pi^+ \pi^+$. By analyzing an independent data sample collected in 2012, the mass was measured as 3621.4 MeV, and the signal was confirmed (ibid.). It was a different particle to the singly charged state claimed by SELEX, but the results appeared inconsistent because the masses differ by around 100 MeV. Thus, the search for the counterpart of Ξ_{cc}^{++} state is among the few important studies that LHCb follows. Although it may seem extremely difficult to observe a double heavy baryon in any currently available experiment, this may increase the possibilities, along with experimental innovations that could increase the sensitivity (Cowan et al., 2018).

2.10. From X(3872) to X_b

As noted in the previous sections a lot of new states have been observed in charmonium and bottomonium systems, which do not be fit with estimations in the quark model. These new hadrons have been found above the corresponding threshold for producing pairs of D or B mesons. Current measurements are not able to separate clearly between the molecular and firmly bound diquark models. However, continued experimental studies of the X(3872) properties will help to understand its structure. With this purpose, this thesis presents an inclusive study of X_b which is the bottomonium counterpart of X(3872). In the next section, the expected general features of X_b will be mentioned.

2.10.1. Expected Characteristic Properties of X_b

A precise estimate of the mass of X(3872) was made long ago based on the calculation of the binding of D^0 and $\bar{D}^{*0}$ with pion exchange and other forces (Tornqvist, 1994). This estimate was prolonged to bottom mesons, for a $B\bar{B}^{*0}$ + c.c. state of $J^{PC} = 1^{++}$ the mass M(X_b) = 10562 MeV (Tornqvist, 2004) was predicted. This predicted mass is very close to observed for P-wave bb excitation χ_{b1}(3P), its mass ranging from about 10510 to 10550 MeV/c^2 (Karliner et al., 2015a).

There are several estimates for mass of X_b. From these estimates, an independent estimate of M(X_b), was based on the expected binding energy of a B and $\bar{B}^{*0}$, yielding 10585 MeV/c^2 (Karliner et al., 2015b). As a result of this, it was understood there should be two nearby states with $I = 0$, $J^{PC} = 1^{++}$ sharing common decay modes to some extent. In another estimate, just below $B\bar{B}^{*0}$ threshold, it was estimated the mass of the X_b should be $M(X_b)$ = 10604 MeV/c^2 (AlFiky et al., 2006).

Lately, the CMS (Chatrchyan et al., 2013) and ATLAS (G. Aad et al., 2014) experiments have searched for the decay $X_b \to \Upsilon(1S)\pi^+\pi^-$ being motivated from the analogous decay $X(3872) \to J/\psi\ \pi^+\pi^-$. The analogy is misleading for this particular decay channel, because for an isoscalar with $J^{PC} = 1^{++}$ such a decay is forbidden by G-parity conservation (Karliner et al., 2015a). Although the X_b is forbidden by G-parity conservation for an isoscalar with $J^{PC} = 1^{++}$, so how come X(3872) is also an isoscalar with the same J^{PC} does decay into $J/\psi\ \pi^+\pi^-$? The isospin is badly broken between D^+ and D^0. D^+ is 4.76 MeV heavier than D^0, while D^{*+} is 3.30 MeV heavier than D^{*0}, in the charm sector. $X(3872) \to J/\psi\ \pi^+\pi^-$ is allowed because X(3872) is right at the $\bar{D}D^*$ threshold, its decays break the isospin conservation (ibid.).

Like the charm sector, in the bottom sector, the decay $X_b \to \Upsilon(1S)\pi^+\pi^-$ is also forbidden because the $B^0 - B^+$ mass difference is tiny, 0.32 MeV, so isospin is very well conserved in the decays of X_b ($\bar{B}B^*$) molecules. By comparing the binding energy with the isospin splitting in the two-meson sectors, the difference between isospin violation in X(3872) and X_b decays can be measured in a simple way. For X(3872) to be pure $I = 0$, it would have to be an equal mixture of $\bar{D}^0 D^{0*}$ and $D^- D^{+*}$. But the masses of these two components are very different (ibid.): $M(\bar{D}^0 D^{0*}) = (3871.80 \pm 0.12)$ MeV vs. $M(D^- D^{+*}) = (3879.87 \pm 0.12)$ MeV.

The mass of X(3872) specified at the threshold $\bar{D}^0 D^{0*}$ is (3871.69 ± 0.17) MeV (Olive et al., 2014), i.e. the binding energy is less than 1/2 MeV. The $D^- D^{+*}$ component does not contribute as it is well above the threshold. X(3872) decays into both $J/\psi\omega$ and $J/\psi\rho$ with approximately equal branching fractions because the $\bar{D}^0 D^{0*}$ is a combination of $I = 0$ and $I = 1$. The X_b binding energy was estimated with the help of the existing data: $Z_b(10610)$, $Z_c(3900)$ in the $I = 1$ channel, and X(3872) in the $I = 0$ channel (Nussinov et al., 2013). Since the kinetic energy is inversely proportional to mass, the heavier the heavy quark, the deeper the binding. The upshot is that even in the most extreme case of infinitely heavy b-quark analogue the binding energy is 35 MeV (Karliner et al., 2015a). But, for the 5 GeV b-quark, the binding energy was found to be significantly smaller, about 20 MeV (ibid.). The situation in the bottomonium sector, about 20 MeV below the BB threshold of X_b, is very different from the charmonium sector: $M(\bar{B}^0 B^{0*})$ = (10604.8 ± 0.4) MeV vs. $M(B^- B^{+*})$ = (10604.5 ± 0.4) MeV.

In this case, the isospin splitting is very small compared with the binding energy: (0.3±0.4) MeV vs. at least 20 MeV, i.e., at most 1.5 % (ibid.). Therefore X_b will be an almost pure isoscalar (ibid.). The mass of X_b is predicted to be 10585 MeV/c^2, approximately 23 MeV/c^2 more than Tornqvist (Tornqvist, 1994).

2.10.2. Strategies for Observation to X_b

Possible mixing of X_b with the $\chi_{b1}(3P)$ bottomonium state indicates that the decays of the $\chi_{b1}(3P)$ and of lighter χ_b states will provide a good guide for isospin-conserving X_b decays (Karliner et al., 2015a). With this purpose, many final states are focused on the decay below:

- $\mathbf{X_b \to \Upsilon(1S)\omega = \Upsilon(1S)\pi^+\pi^-\pi^0}$

This process came to the fore with the $\chi_{b1,2}(2P) \to \Upsilon(1S)$ decays observed by CLEO Cooperation (Severini et al., 2004). It is difficult to make an estimate for $\chi_{b1}(3P) \to \Upsilon(1S)\omega$ because the increased *Q* value can be compensated by a smaller transition matrix element. The total width was projected 79 keV for $\chi_{b1}(2P)$ (Kwong et al., 1988), so the branching fraction is an expected partial decay width $\gamma(\chi_{b1}(2P) \to \Upsilon(1S)\omega) \simeq 1.3$ keV, about $1/3$ of the partial decay rates for $\chi_{b1}(3P) \to \gamma\Upsilon(1S, 2S)$ (Karliner et al., 2015a). Belle Collaboration did not observe a significant signal for

$X_b \rightarrow \Upsilon(1S)\pi^+\pi^-\pi^0$.

- **$X_b \rightarrow \Upsilon(2S)\omega^* = \Upsilon(2S)\pi^+\pi^-\pi^0$**

Although the Q value of this decay is too small to allow an accurate ω production, the three pion systems can be produced with an effective mass of up to 540-560 MeV depending on the exact mass of the X_b (Karliner et al., 2015a).

- **$X_b \rightarrow \chi_{b1}\pi^+\pi^-$**

This decay has features in common with the decays $\chi_b(2P) \rightarrow \chi_b(1P)\pi\pi$ observed by the CLEO (Cawlfield et al., 2006) and BaBar (Lees et al., 2011) Collaborations. The Particle Data Group (Olive et al., 2014) shows the averages for this decay as follows: $B(\chi_{b1}(2P) \rightarrow \chi_{b1}(1P)\pi\pi) = (9.1 \pm 1.3)10^{-3}$, $B(\chi_{b2}(2P) \rightarrow \chi_{b2}(1P)\pi\pi) = (5.1 \pm 0.9)10^{-3}$. In these decays, the total spin of the bottomonium system is preserved. Therefore, it is reasonable to assume that it will also apply to X_b decay (Karliner et al., 2015a). There is just barely enough Q-value to permit the decay $X_b \rightarrow \chi_b(2P)\pi\pi$, so it makes more sense to look for $X_b \rightarrow \chi_b(1P)\pi\pi$, followed of course by $\chi_{b1}(1P) \rightarrow \gamma\Upsilon(1S)$ (ibid.).

- **$X_b \rightarrow \Upsilon(3S)\gamma$**

Since it is assumed that X_b contain $\chi_{b1}(3P)$ a significant amount in its wave function, this decay is likely to dominate over $X_b \rightarrow \Upsilon(1S, 2S)\gamma$ (ibid.).

- **$X_b \rightarrow \Upsilon(1S, 2S)\gamma$**

The decays $\chi_b(3P) \rightarrow \Upsilon(1S, 2S)\gamma$ have been observed (G. Aad et al., 2014) and as the X_b is expected to mix strongly with the $\chi_{b1}(3P)$ so it is worthwhile to examine the $\Upsilon(1S, 2S)\gamma$ mass spectra for any departures from single Breit-Wigner behavior (Karliner et al., 2015a).

Several suggestions have been made to describe X_b, the bottomonium analog of X(3872), as noted above. Taking into account these references, the strategy for X_b

observation at the LHC experiments, in particular at CMS with Run-II data should include its search in the $\chi_{b1}(1P)\pi^+\pi^-$ final state, where $\chi_{b1}(1P)$ is reconstructed in its decay to $\Upsilon(1S)$ plus a photon with $\Upsilon(1S)$ decaying into two muons ($\Upsilon(1S) \rightarrow \mu^+\mu^-$). Alternatively, the $\Upsilon(1S)\pi^+\pi^-$ final state could be still explored, as done in CMS with Run-I data, since its reconstruction is more efficient even if the decay itself should be suppressed because it implies G-parity symmetry violation. By exploiting the data collected during Run-II, CMS can reconstruct the previous two final states and look for the X_b signal with enough experimental sensitivity.

This is realistic for two main reasons. The first is that a dedicated trigger has been configured to select events of interest (in which an *S-wave* bottomonium state, like Υ(nS) with n=1,2,3, is present), with enough low thresholds, and it has been producted during the whole data taking of 2017 and 2018. The second is that CMS has already shown the capability to reconstruct photons by conversion into electron-positron pairs within the tracker material, with enough mass resolution to resolve the $\chi_{c2}(1P)$ and $\chi_{b2}(1P)$ peaks from the $\chi_{c1}(1P)$ and $\chi_{b1}(1P)$ peaks, and recently to separate $\chi_{b1}(3P)$ from $\chi_{b2}(3P)$ peaks for the first time (CMS Collaboration, 2018). Of course, these converted photons, like those involved in the $\chi_{b1}(1P)$, are low energy ones ("soft") and are characterized by a low reconstruction efficiency. This happens because only a small fraction of those low-energy photons convert into e^+e^- pairs and only a fraction of those pair tracks can be reconstructed using the CMS silicon tracker. The photon reconstructed in the calorimeters instead of conversion in the silicon tracker should be also explored: the reconstruction efficiency would be much higher at the cost of spoiling the mass resolution; this trade-off should be better understood for the particular final states under study. Particular care is needed in the configuration of the selection criteria to reject as much background as possible while retaining the signal as efficiently as possible. Because of the low efficiency in the reconstruction of soft converted photons the latter needs to be carefully investigated with the help of simulated data. It will be likely needed to explore the extraction of the final states' mass spectra by using, alternatively to a cut-based selection, some neural network, or Boosted Decision Trees techniques. For the latter, simulated signal samples must be produced while background distributions are usually taken from real data.

Moreover, simulated signal samples with several different mass values should be generated in the search mass window for the X_b in order to extract the variation of the mass resolution as a function of the mass itself and to estimate the efficiency in the signal reconstruction again as a function of the mass. The statistical treatment needed to get a meaningful result is rather sophisticated, either in case of assessment of the statistical significance of the X_b observation or in case of providing the upper limit on the production cross-section of the X_b times its (unknown) branching fraction for the decay in the specific final state (either $\chi_{b1}(1P)\pi^+\pi^-$ or $\Upsilon(1S)\pi^+\pi^-$). In both cases, sophisticated interpolation techniques are required to be configured and executed on hybrid computational platforms. This research can be necessary for the physics of hadrons and help to shed light on the way quark combine to build the particles and, in the last analysis, how the matter can be intimately composed.

3. EXPERIMENTAL SETUP

CERN, the European Organization for Nuclear Research, was established at the Swiss-French border in Geneva in 1954. While it was one of Europe's first joint initiative now it has 23 member countries. Physicists and engineers at CERN use the world's largest and most complex scientific instruments that are purpose-built particle accelerators and detectors to search the basic constituents of matter i.e. fundamental particles. The task of accelerators is to boost particle beams to high energies before the beams collide with each other or with fixed targets. The task of the detectors is to detect and record the results of these collisions. CERN has played the main role in various stimulating discoveries of SM particles, like the discovery of the $W^{\pm}$ and Z^0 bosons in 1983 (UA2 Collaboration, 1983) and the Higgs boson in 2012 (Georges Aad et al., 2012b). Also it is the birthplace of the World Wide Web (www) (Segal, 1995).

LHC which is the world's largest and most powerful particle accelerator is also located at CERN. On 10 September 2008, it first launched up and still remains the latest addition to CERN's accelerator complex. There are four points around the accelerator ring to collide the beams inside the LHC which correspond to the positions of four particle detectors which are ATLAS, CMS, ALICE, and LHCb. In the following section, the LHC and its experiments will be briefly intro- duced. The CMS experiment at the LHC will also be briefly introduced with an emphasis on the most important components for this thesis.

3.1. The Large Hadron Collider

The LHC installed in the 26.7 km circular tunnel is a superconducting hadron accelerator and collider with a design center-of-mass energy $\sqrt{s}$ = 14 TeV for pp collisions. In the LHC, protons are used instead of electrons because an electron is about 2000 times lighter than a proton, and at some point, it is impossible to make the electrons rotate around the circle because of the amount of energy they lose. Before the LHC, the Large Electron-Positron Collider (LEP) which was the most powerful lepton accelerator to date that was in operation until 2000 and subsequently dismantled, was installed in this tunnel. Moreover, the LHC is also designed to accelerate lead ions. And in 2017 xenon-xenon collisions have been achieved (Schaumann et al., 2018). But the focus here will be on pp collisions recorded during the data-taking period starting in 2015 and ending in 2018, so-called LHC Run II.

An overview of the CERN accelerator complex is given in Figure 3.1.. And the LHC is the last element in the chain of this accelerator complex since protons need to be accelerated to enough energies before they reach the LHC. After obtaining protons by stripping electrons off of hydrogen atoms in the Duoplasmatron, protons are accelerated in so-called bunches containing $N_\mathrm{b} \sim 1.15\times 10^{11}$ protons each. The LINear ACcelerator 2 (LINAC2) where protons are accelerated up to 50 MeV is the first step for them. After the LINAC2, they are sent to the next stages, all of which are Synchrotons. They are accelerated up to 1.4 GeV in the Proton Synchroton Booster (PSB), bunches are formed in the Proton Synchroton (PS) where they are accelerated up to 25 GeV before they are transferred to the Super Proton Synchroton (SPS). In the SPS the acceleration up to 450 GeV occurs before the protons are fed into and accumulated in the LHC ring in two circulating beams. It continues until the design value of n_b= 2808 bunches per beam is reached. These bunches are accelerated up to the desired collision energy, 7 TeV, afterward fully filling the LHC. In ideal conditions, the total process of filling the LHC and accelerating the protons to the design energy takes about 36 minutes. But the beams can be kept in “collision mode” for some hours till the beam intensity becomes too low and a new fill is started (Bryant, 2008). The bunches travel in the beamlines which are arranged such that there are four main collision points along the LHC ring. The main experiments ATLAS, CMS, ALICE, and LHCb are built around these collision points. These four experiment will be introduced shortly below.

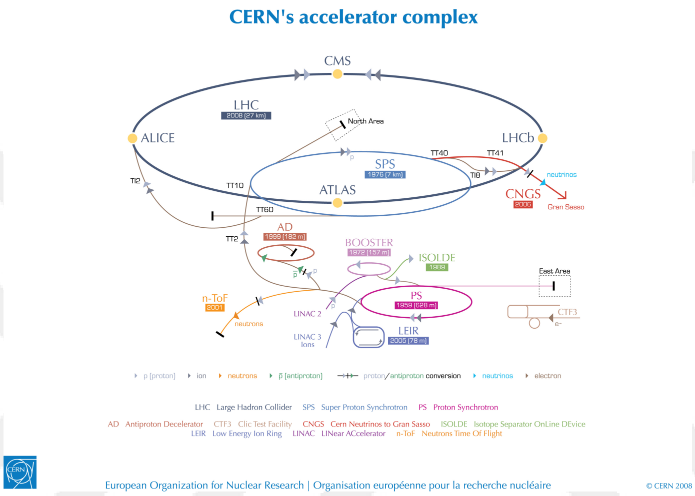

Figure 3.1. Overview of the CERN accelerator complex ($Lef\tilde{A}\acute{I}vre$, 2008)

- **ALICE**: The ALICE experiment was designed to research the physics of strongly interacting matter and the occurrence of the quark-gluon plasma at excessive energy intensities and temperatures in heavy-ion collisions (ALICE Collaboration, 2008). While it is designed to cope with the excessively high multiplicity of charged particle tracks occurring in heavy-ion collisions, it cannot operate at the same instantaneous luminosity conditions as ATLAS and CMS during pp collisions.
- **ATLAS**: The ATLAS detector is the largest of the four LHC experiments

(Georges Aad et al., 2012a). It is a 25 m in diameter and 44 m of length. Like CMS, it is a general-purpose detector addressing a wide range of physics questions. To confirm possible discoveries, CMS and ATLAS experiments supplement each other and serve as independent experiments.

- **CMS**: CMS is another general-purpose experiment with a slightly different design than ATLAS (CMS Collaboration, 2008). It will be explained in more detail in Sec. 3.2.
- **LHCb**: The LHCb experiment specializes in researching the slight differences between matter and antimatter by studying a type of particle, the b quark (LHCb Collaboration, 2008). While the ATLAS and CMS surround the entire collision point with an enclosed detector, it uses a series of subdetectors to detect mainly forward particles thrown forward by the collision in one direction.

For a given cross-section in a particle accelerator, the expected average number of events per second can be calculated by

$$N = L \cdot \sigma \tag{3.1}$$

where L is the instantaneous luminosity which is one of the most important parameters defining a particle accelerator, the total amount of data collected by the LHC experiments can be estimated as a function of the specific cross-section and the integrated luminosity as follows:

$$N = \sigma \cdot \int \mathcal{L}(t)dt, \tag{3.2}$$

Figure 3.2. gives the LHC total luminosity by 2018. The luminosity is generally given in the unit of fb^{-1} or pb^{-1}. The barn is a unit to measure cross-sections in particle physics and $1b = 10^{-24}$ cm^{-2}. Luminosity associates the average number of occurrences of a process with a given cross-section to collected data. Figure 3.2.

shows that the LHC has delivered 192.3 fb^{-1} to CMS, of which 177.7 fb^{-1} have been recorded from the start of Run I in 2011 to the end of Run II in 2018.

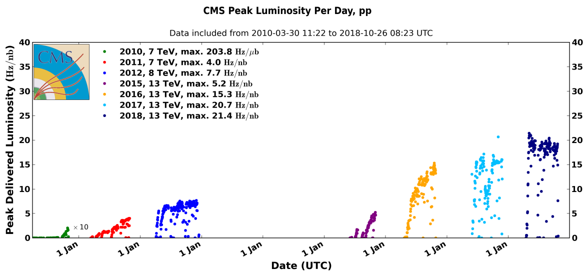

Figure 3.2. Peak instantaneous luminosity ($10^3 4$ cm^{-2} s^{-1} = 10 Hz nb^{-1}) in pp collisions vs time for Run I (2010–2012) and Run II (2015–2018) (CMS Collaboration, 2019)

The LHC tries to collect as many protons as possible into the beam and squeeze it as close as possible to maximize the probability of the tiny protons colliding with one another. Thus, the narrower the beam, and the more protons in it, the higher the luminosity is. When these bunches cross one another, more than one proton-proton collision occurs; this is known as pile-up (PU). The CMS must work backward because it must observe the decay products of the various particles produced in these collisions and determine which collision interactions produced which particles. In 2012 the average number of interactions per bunch crossing at the CMS was around 21 (CMS Collaboration, 2019). The PU distribution for different data-taking periods is given in Figure 3.3.

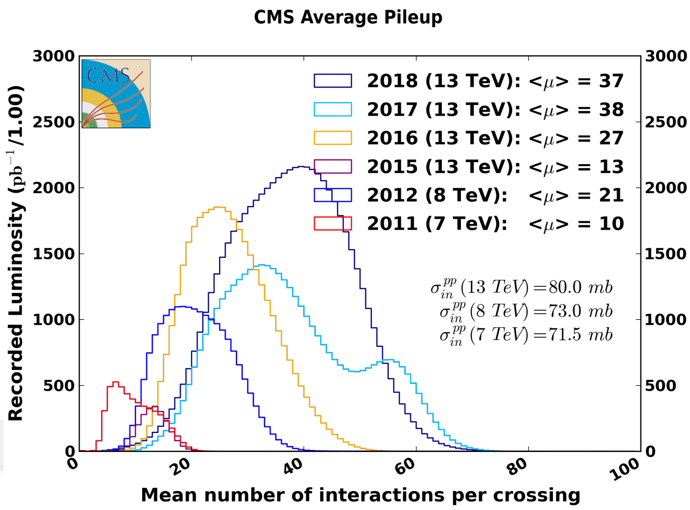

Figure 3.3. The distribution of pile-up for different data-taking periods in Run I (2010–2012) and Run II (2015-2018) (CMS Collaboration, 2019)

3.2. Compact Muon Solenoid

The CMS is an experiment located in Cessy, France, with a length of 21.6 m, a diameter of 14.6 m, and a mass of 14000 t (CMS Collaboration, 2008). It designed as a general-purpose particle detector to include a wide range of physics topics. Figure 3.4. shows the layout of the CMS detector.

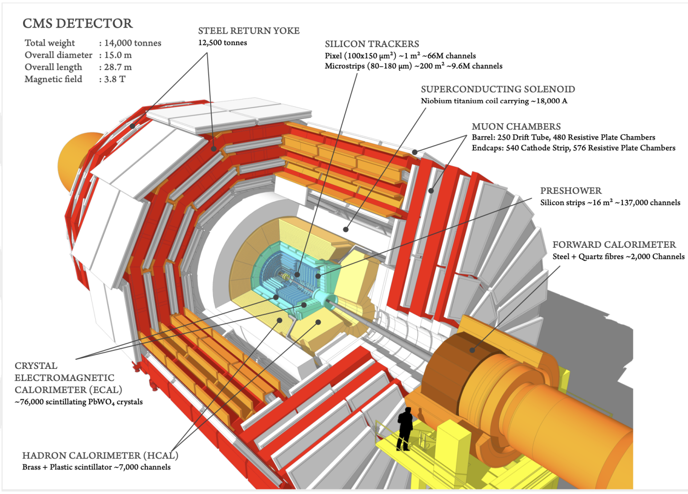

Figure 3.4. The layout of the CMS experiment after the upgrade of the pixel detector at the end of 2016 (Sakuma et al., 2014)

The CMS has a typical onion-like structure of modern particle physics experiments detectors at particle colliders. It is designed to measure the energy and momentum of particles exploiting specific properties. The main feature of the CMS is the solenoid providing a 3.8 T magnetic field. From the inside out, there are the silicon pixel and strip trackers, ECAL (the Electromagnetic Calorimeter), and HCAL (the Hadron Calorimeter). The muon detection system is outside of the solenoid. It is integrated into the steel return yoke for the magnetic field, which makes up more than 95 % of the total weight of CMS. The silicon trackers correctly measure the positions and momentum of charged particles. The calorimeters measure the energies of all particles. Electrons and photons deposit their energy in the ECAL, while hadrons mainly in HCAL. Muons detected in the muon system are the only particles that can enter the solenoid and reach the muon chambers of the muon system. Different particles leave different signatures in the CMS detector. In this way, different particles can be identified by their signatures, as shown in Figure 3.5..

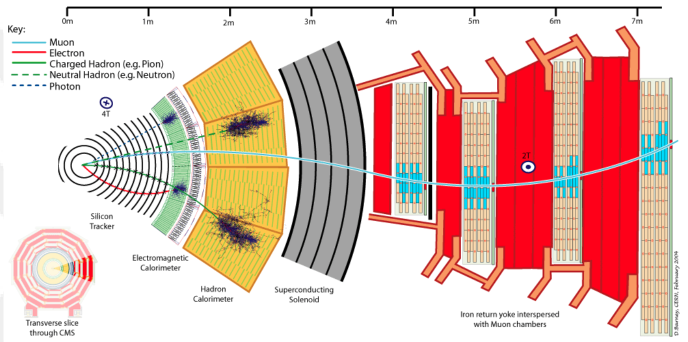

Figure 3.5. Illustration of particle identification in CMS in a slice of the transverse view of the detector (CMS Collaboration, 2018)

CMS uses a cylindrical coordinate system. The center of the coordinate system of the CMS is described to be in the foreseen interaction point (IP) of CMS. The *y-axis* is pointing vertically upward, and the *x-axis* is pointing radially inward toward the center of the LHC, and the *z-axis* is along the direction of the beam running counterclockwise. The polar angle θ is measured from the *z-axis* and the azimuthal angle Φ is measured from the x-axis in the *x-y-plane* (CMS Collaboration, 2006). The pseudorapidity, generally, is used in place of the polar angle, and it is described as:

$$\eta = -\ln\left[\tan\left(\frac{\theta}{2}\right)\right], \tag{3.3}$$

In the case of high energy with $E \gg$ m or massless particles, the rapidity η is described as a function of the energy E and longitudinal momentum p_z as follows (Tanabashi et al., 2018):

$$y = \frac{1}{2}\ln\left(\frac{E+p_z}{E-p_z}\right). \tag{3.4}$$

3.2.1. Inner Tracking System

The inner tracking system consists of silicon pixel and silicon strip sensors, and it is located in the innermost part of the CMS detector. It is designed to provide a precise and efficient measurement of the trajectories of charged particles emerging from the LHC collisions, as well as a precise reconstruction of secondary vertices (CMS Collaboration, 2008). Figure 3.6. shows a schematic cross-section through the CMS tracker. In this figure, each line represents a detector module, and double lines demonstrate back-to-back modules which deliver stereo hits. The pseudorapidity range is $|\eta| \leq 2.5$ in the tracking system. It is divided into two parts, the pixel detector and the silicon strip tracker. The CMS silicon pixel and strip trackers play a key role in the CMS physics program since they provide high-efficiency charged-particle reconstruction and momentum resolution in energy.

The tracking system has to deal with the difficult conditions posed by the LHC. It has a fast response time and high granularity since, at the instantaneous design luminosity, in each bunch crossing an average of 1000 charged particles hit the tracker. The main challenge in the design of the tracking system was to develop detector components able to operate in these harsh environments for an expected lifetime of 10 years (Tanabashi et al., 2018). These requirements on granularity, speed, and radiation hardness lead to a tracker design entirely based on silicon detector technology (ibid.). It has to meet all requirements, such as a minimal material budget to limit processes that could bias the trajectory reconstruction like multiple scattering, nuclear interactions, bremsstrahlung, or photon conversions. So it is completely silicon-based (ibid.). Moreover, the tracer must be radiation resistant to withstand the heavy radiation caused by the dense particle flux.

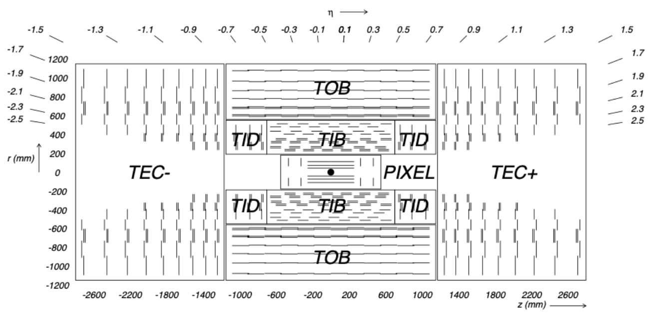

Figure 3.6. Schematic cross-section through the CMS tracker (CMS Collaboration, 2018)

3.2.1.1. Pixel Detector

The CMS pixel detector is the innermost subsystem installed nearest to the interaction region. Since it contributes precise tracking points in r-Φ and z, it is responsible for a small impact parameter resolution that is important for good secondary vertex reconstruction (CMS Collaboration, 2018). The pixel detector covers a pseudorapidity range $-2.5 < \eta < 2.5$, matching the acceptance of the central tracker. It is necessary to reconstruct secondary vertices from b and tau decays and form seed tracks for the outer track reconstruction and high-level triggering.Figure 3.7. shows the geometrical layout of the pixel detector (CMS Collaboration, 2018).

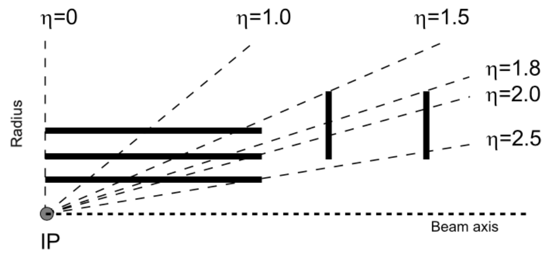

Figure 3.7. The geometrical layout of the pixel detector (CMS Collaboration, 2018)

The pixel detector has three barrel layers (BPix) with two endcap disks (FPix). During the Run II data-taking period, the 53 cm long BPix layers were located at mean radii of 4.4, 7.3, and 10.2 cm and the FPix disks extending from ≈ 6 to 15 cm in radius, was placed on each side at $z = \pm 34.5$ and $z = \pm 46.5$ cm (ibid.). The BPix contains 48 million and the FPix contain 18 million, the total 66 million, pixels covering a total area of BPix is 0.78 and FPix is 0.28 m^2. This layout of the 3 barrel layers and the forward pixel disks on each side provides 3 tracking points over almost the full η-range (ibid.).

In 2010, the LHC started its physics program with pp collisions at a center of mass energy of 7 TeV. But the center mass of energy was increased to 8 TeV and in August 2012, a further 11 fb^{-1} integrated luminosity has been delivered, with instantaneous peak luminosities approaching $7 \times 10^{33} cm^{-2} s^{-1}$ (Dominguez et al., 2012). The upgrading of the pixel detector to so-called Phase I of the pixel detector, was carried out before the end of 2016 and the beginning of the 2017 data-taking period to perform the same or even better in these operating conditions. During Phase I, owing to the modular design of the CMS detector, it was possible to replace the entire existing pixel detector with a new one within a few months. In this new pixel detector, the number of pixels is increased to 124 million, and it has been designed with four-barrel layers and three endcap disks. New readout chips were foreseen to withstand the increased luminosity conditions of the LHC until 2023 (Dominguez et al., 2012). It was made possible by these new instruments to provide higher tracking efficiencies, lower rates of misidentifying tracks, and lower data loss. Figure 3.8. shows the conceptual layout comparing the different layers and disks in the current and upgraded pixel detectors.

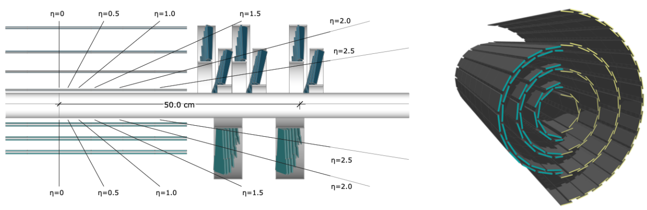

Figure 3.8. (Left) Conceptual layout comparing the different layers and disks in the current and upgraded pixel detectors. (Right) Transverse-oblique view comparing the pixel barrel layers in the two detectors (Dominguez et al., 2012)

3.2.1.2. The Silicon Strip Tracker

The Silicon Strip Tracker, built from silicon strip modules, is the following subdetector which is also part of the tracker system. Like the pixel tracker, the Silicon Strip Tracker which is consists of modules arranged in layers in the barrel and discs in the end cover regions and includes four main sub-detectors which are named Tracer Inner Barrel (TIB), Tracer Outer Barrel (TOB), Tracer Inner Discs (TID) and Tracer End Caps (TEC). As can be seen in figure 3.8., TIB and TOB are in the barrel part, which has a total of 10 layers that are arranged in the barrel extending up to a radius of 1.1 m. TID and TEC, consisting of three disks and nine disks, respectively, involve the beam axes covering the remaining part of the η phase space region of the whole tracker system. The CMS tracker is equipped with 15 different sensor geometries, which are two rectangular sensor types, each for TIB and TOB, and 11 wedge-shaped sensor types for TEC and TID. The strip tracker has 9.3 million strip modules and covers an area of 198 m^2, and the total number of silicon sensors is 24.244 (Dominguez et al., 2012).

3.2.2. Electromagnetic Calorimeter

The Electromagnetic Calorimeter (ECAL) of CMS detector is a hermetic homogenous calorimeter placed between the inner tracking system and the HCAL. It is consisting of 75848 lead tungstate (PbOW4) crystals which have high response and granularity, of which 61200 are mounted in the barrel part and the remaining ones in the two endcaps (ibid.). It has two main parts: the barrels, orientated through the z-axis (EB), and the endcaps (EE), which are oriented in a direction perpendicular to the beam axis. The whole ECAL system covers pseudorapidities up to $|\eta| < 3$. ECAL is

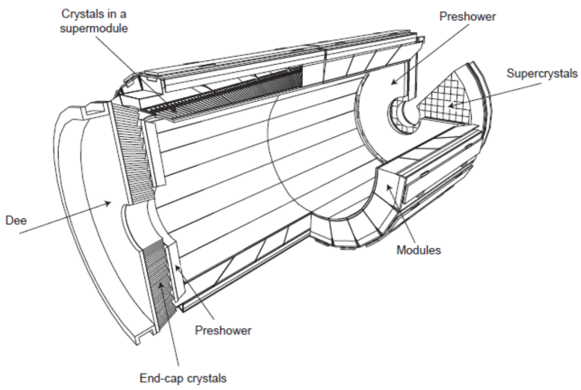

Figure 3.9. The 3D view of ECAL showing the part of the detector responsible to the energy reconstruction of photons and electrons (CMS Collaboration, 1997)

in charge of the energy reconstruction of photons and electrons. While electrons and photons pass through, the highly dense lead tungstate crystals scintillate. High energy photons and electrons produce a chain that has lower energy photons and electrons called an "electromagnetic shower". This process occurs mainly via pair production by photons or bremsstrahlung by electrons. It continues until either the energy of the photons drops below the threshold for pair production or ionization processes start to dominate. The charged particles in the electromagnetic shower ionize the atoms of the PbWO4 crystals. The de-excitation of the atoms gives scintillation light that is collected and converted into an electric signal in photodiodes (CMS Collaboration, 1997).

3.2.3. Hadron Calorimeter

The Hadronic Calorimeter (HCAL), which is installed between the ECAL and the solenoid of CMS, completes the calorimeter system. It consists of several absorbing brass layers interleaved with plastic scintillator layers. HCAL is a sampling calorimeter. It provides energy measurements of all the charged and neutral hadrons like protons, neutrons, pions, or kaons. It is divided into four subdetectors (Figure 3.10.): the HCAL barrel (HB), endcap (HE), forward (HF), and outer barrel (HO). HB and HE detectors provide coverage in the pseudorapidity (η) range |η| < 1.4 and 1.3 < |η| <3.0 respectively, surround the ECAL, and they are included entirely within the high magnetic field region of the solenoid (CMS Collaboration, 2009).

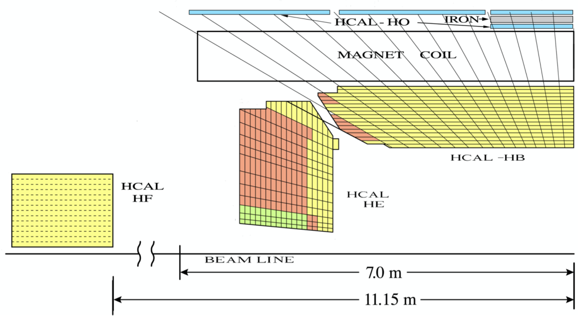

Figure 3.10. Quarter view of the CMS hadron calorimeter (CMS Collaboration, 2009)

The HF extends the HCAL pseudorapidity coverage into the |η| region 2.9 – 5.0, and it provides measurements of energetic forward jets and increases the hermeticity of the missing transverse energy measurement (ibid.). The HO is responsible for ensuring the energy reconstruction missed by the HB and HE. Moreover, each subdetector of HCAL covers the full range of the azimuthal angle Φ.

3.2.4. Superconducting Magnet

The CMS superconducting solenoid is the central device of the CMS detector with a 3.8 Tesla magnetic field which is 100.000 times stronger than the Earth's. This magnetic field is requisite to reconstruct the charges and the momenta of charged particles from 1 GeV up to more or less 1 TeV. The CMS solenoid has been made of a high-purity aluminum stabilized Niobium-Titanium conductor. It has a 6.3 m bore, is 12.5 m long, and weighs 220 t (Dominguez et al., 2012).

3.2.5. Muon system

The Muon detector is located in the outer part of the detector. It has three main parts: the drift tubes (DT), the cathode strip chambers (CSC), and the resistive plate chambers (RPC) (CMS Collaboration, 2006). The DTs are located in the barrel region ($|\eta| < 1.2$). They are organized in four stations placed between the layers of the steel return yoke. The CSCs are located in the endcap region ($0.9 < |\eta| < 2.4$) and are organized in four disks placed between the layers of the steel return yoke. The RPCs are placed both in the barrel and part of the endcap region (ibid.). Figure 3.11. shows a schematic picture of the muon system and all parts of it. The muon reconstruction is important for CMS since, like studies of quarkonium physics, many experimental signatures involve muons in their final state.

This detector is dedicated to three primary purposes: identifying muons, improving the measurement of muon momenta, and triggering the readout of exciting events. In muon detectors, only muons leave traces because all particles except

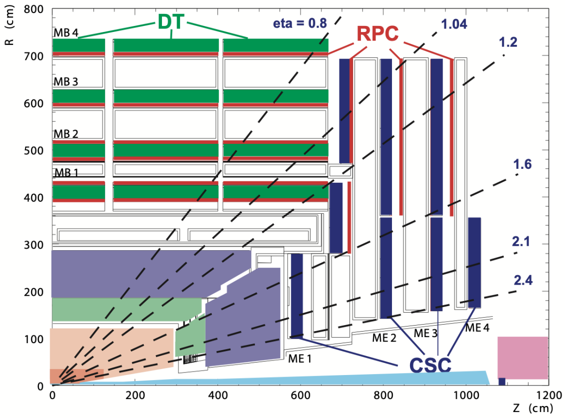

Figure 3.11. Layout of one quarter of the CMS muon system (CMS Collaboration, 2006)

weakly interacting muons and neutrinos are assumed to be stopped in calorimeters or solenoid.

3.2.6. Trigger and Data Acquisition Systems

The online selection of all data collected by the CMS detector is carried out in the Trigger System. The bunch spacing in the LHC is 25 ns, corresponding to a bunch crossing frequency of 40 MHz for pp collisions. At each bunch crossing, tens of collisions take place, and when the high frequency is combined with these collisions, this leads to PU. This process makes it impossible to read out, process, and store each event, which has a size of around 1 MB (Khachatryan et al., 2017). The main idea is to select signal processes not occurring that often. For those processes having a huge contribution, only a fraction of events are stored for further analysis. For this purpose, the trigger procedure consists of two levels: the Level-1 (L1) trigger and the high-level trigger (HLT).

Level-1 Trigger: The Level-1 trigger is a hardware-based selection procedure. It is in charge of decreasing the event rate in just 4 μs from the 40 MHz bunch crossing rate of the LHC to around 100 kHz, which is the maximal readout frequency of the full event information from the detector front-end electronics. In less than 4 μs, the L1 trigger has to form a decision whether to keep or discard an event using only information of the muon systems and the calorimeters (CMS Collaboration, 2000). Because of such tight low lateness limits, the L1 trigger is hardware-based. It uses Field Programmable Gate Arrays (FPGAs) and Application-Specific Integrated Circuits (ASICs) to run simple algorithms in parallel. The Global Trigger (GT) is the last L1 step, and only if the L1 trigger reaches a positive decision a full detector readout is triggered, and the event is further processed by the HLT (CMS Collaboration, 2008). The L1 trigger was upgraded during the Long Shutdown (LS) 1, commissioned in 2015, which was the first year of data taking in Run II, which is highly related to the data analysis of this thesis. During Run II, as it has been foreseen the center of mass energy of the LHC pp collisions increased the center of mass energy up to 13 TeV. It gradually reached an instantaneous luminosity of $2\times 10^{34}\text{cm}^{-2}\text{s}^{-1}$ or higher, the Trigger and Data acquisition system has been upgraded to have a successful physics program in this dense environment (Luca, 2017). It has been upgraded by benefits from the recent μTCA technology and is designed to maintain the performance under high instantaneous luminosity conditions (ibid.). Innovative algorithms have been used that can significantly reduce the trigger rate and increase trigger efficiency for a wide variety of physics processes (ibid.). Figure 3.12. is shown schematics of the structure of the L1 trigger upgraded system.

Before being merged in the GT, the calorimeter trigger and muon trigger

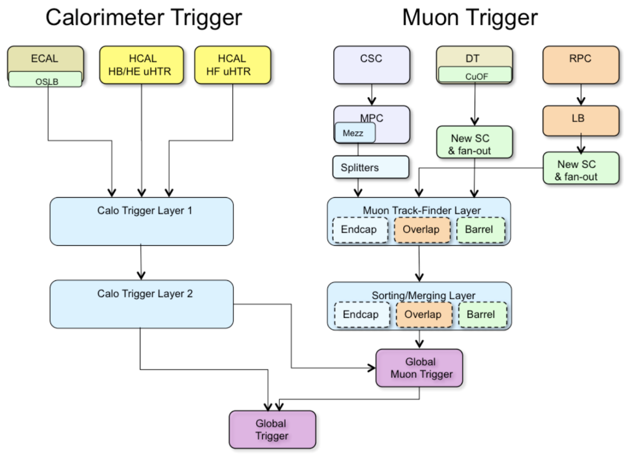

Figure 3.12. Schematics of the structure of the L1 trigger upgraded system (Luca, 2017)

receives input trigger primitives from different subdetectors. But the muon trigger also receives information from the calorimeter trigger to compute muon candidates' isolation. And the outputs of both calorimeters are combined into physics objects like muons, electrons or photons, jets, and various energy sums, in the GT for the final trigger decision (Luca, 2017).

High-Level Trigger: HLT using the information of all events received from the L1 Trigger system has to reduce the rate from 100 kHz down to 100Hz, which is the limiting factor in processing the output data downstream of the HLT. The HLT paths are collected in the HLT menu, like the L1 trigger, but the number of HLT paths that can be used is not limited by the hardware used in L1. HLT menu has almost 600 paths which covers different parts of the CMS physics program. After receiving the information of all events from the L1 Trigger system, HLT starts to reconstruct the events. They are stored or removed depending on whether they satisfied any of the path triggers. It decides to split the events into online streams and datasets according to the different physics analysis groups (PAGs). For example, the MuOnia is the primary data set for b-physics (BPH) PAG.

Data Quality Monitor: The Data Quality Monitoring (DQM) system is in charge of cross-checking the hardware and software intervening in the data processing at the early stage of the data taking. This procedure consists of two parts which are online and offline. The online procedure is performed as soon as the Trigger system collects the data. Moreover, the offline procedure cross-checks the results from the online DQM. In the online DQM, in order to define if there is a problem with the detector or trigger systems, the Graphical User Interface provides the histograms of key features corresponding to different subdetectors. This data monitoring procedure performs directly where the CMS is located. Afterward, the event reconstruction, the offline DQM are performed. DQM is very important to the detector and operational efficiency and the reliable certification of recorded data for physics analysis.

B-physics Triggers: The BPH PAG needs different and unique triggers that *low*-p_T dimuons with opposite signs, specific mass windows, displaced vertices, and so on. The BPH trigger space is pretty pure, so that the same events are rarely triggered by more than one trigger path. Thus, at the BPH trigger level, choosing quarkonia is a challenging duty in the circumstances found in CMS because it is necessary to discriminate two muons of *low*-p_T quarkonium decay from high-rate soft muons from hadronic jets. On the one hand, for *high*-p_T quarkonium decays, the two muons are not spatially separated very well. They can be confused with a single muon by the L1 trigger system. But these problems could be alleviated at the HLT.

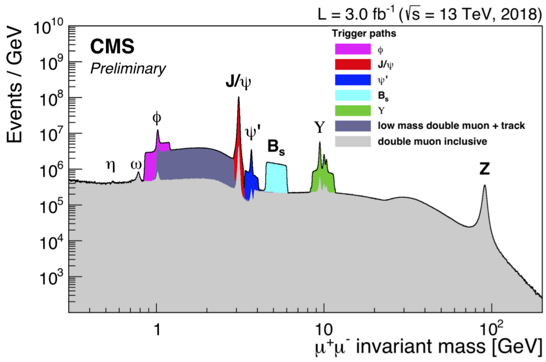

Figure 3.13. Dimuon mass distribution collected with various dimuon triggers (CMS Collaboration, 2018)

Because during Run-II, The LHC is entering into operation with an increased center-of-mass energy of 13 TeV, the B hadron production cross-section was expected to nearly double at this energy. And it was expected that since potentially increasing by almost one order of magnitude, the collected statistics relative to the previous operation period would enable CMS to perform enhanced measurements in the B-physics sector. The BPH trigger has been upgraded to be ready for this increasing luminosity. Figure 3.13. is shown a graphical representation of the events collected by the physics triggers relevant for low mass dimuon physics at 13 TeV in 2018.

3.2.7. Quarkonium reconstruction at CMS

The decay mode of *S-wave* quarkonia is the experimentally most important decay mode at CMS, which is the decay into a pair of oppositely charged muons. The *P-wave* quarkonia are reconstructed in their radiative decay to *S-wave* quarkonia. Thus, the reconstruction of quarkonia in CMS launches by triggering on dimuons and then using the corresponding events for the offline analysis. The reconstruction of quarkonium states is not much different from the reconstruction of other states in high-energy physics experiments. The main idea is that possible candidates are built by combining the known decay products to obtain the original one from which they come. While in the *S-wave* quarkonia reconstruction, this procedure is as simple as combining pairs of oppositely charged muons within the mass region of the quarkonium, in the *P-wave* quarkonia reconstruction, these muon pairs have to be combined with an additional photon. Since many photons and muons are produced in hadron collisions, it is not easy to describe them. In particular, identifying the corresponding photon of *P-wave* conditions is one of the main challenges. The following sections will be explaining muon and photon reconstructions briefly.

3.2.7.1. Muon Reconstruction and Identification

In pp collisions, the standard CMS muon tracks are first reconstructed independently in the inner tracker, which is named the tracker track, and in the muon system, which is named the standalone-muon track. Depending on these objects; there are two reconstruction approaches, Global and tracker muon reconstructions (CMS Collaboration, 2000).

Global muon reconstruction: There is an outside-in approach for global muons reconstruction. For each standalone-muon track, there are two paths propagated onto a common surface. A matching tracker track is found by comparing the parameters of these two paths. A global-muon track is obtained by fitting the combining hits from the tracker track and standalone-muon track (ibid.).

Tracker muon reconstruction: In this approach, all tracker tracks and total momentum are accepted as possible muon candidates. Furthermore, all these candidates are extrapolated to the muon system taking into account the magnetic field, the average expected energy losses and multiple Coulomb scattering in the detector material (CMS Collaboration, 2000). For example, if at least one matching segment, a short stub consisting of DT or CSC hits, is found, the corresponding tracker track is qualified as tracker muon. While tracker Muon reconstruction requires only a single muon segment in the muon system, Global Muon reconstruction requires at least two muon segments. It is designed to have high efficiency for muons penetrating through more than one muon station. For these reasons, tracker muon reconstruction is more efficient than the global muon reconstruction at low momenta (ibid.). In pp collisions at CMS with sufficiently high momenta and within the geometrical acceptance of the muon system, about 99 % of muons are reconstructed. Muon candidates are reconstructed either as a global muon or a tracker muon and very often as both (ibid.). Different selection criteria can be applied to the reconstructed muons in the different physics analyses, based on the needs, to provide the essential balance of detection efficiency and purity. This procedure is named muon identification (muon ID).

3.2.7.2. Photon Conversion Reconstruction

In the CMS detector, there are two ways to reconstruct photons. The first one is from energy deposited in the ECAL, and the second one is from the conversion into an e^+e^- pair in the silicon tracker. Standard photon reconstruction from the energy deposited in the ECAL has a disadvantage: the relative energy resolution scales with the photon energy, and this makes it convenient for the reconstruction of only highly energetic photons. Depending on the knowledge of the silicon trackers, it is possible to reconstruct the converted photons with a relative energy resolution of the order of 10^{-3} converted photons, like for the photons used in the analysis of this thesis. As mentioned before, *P-wave* decays are radiative decays of *S-wave* decays in quarkonia. To reconstruct radiative decays of *P-wave*, $H^{3P_J} \rightarrow H^{3S_1}\gamma$, a photon has to be reconstructed in addition to the two muons from the dimuon decay of the *S-wave* states. However, difficulties arise in this reconstruction process, such as causing photons with low energy and transverse momentum resulting from mass differences of hundreds of MeV between the *P-wave* and *S-wave* states. And such as the mass difference between the *J = 1* and *J= 2* states, which is even lower in the range of tens of MeV. To be able to have the necessary invariant mass resolution of the $\mu\mu\gamma$ system to separate the *J = 1* and *J = 2* states, the photons in radiative *P-wave* quarkonium decays must be reconstructed with a perfect energy resolution.

Photons can be converted into an e^+e^- pair by pair production processes. The pair production processes are the dominant processes for the interaction of the photon with the material of the silicon tracker for photon energies happening in the radiative decays of *P-wave* quarkonia. These converted photons are reconstructed by using the features of the conversion process. These features are that the opposite sign electron pair that comes from conversion vertex (CV), must have an invariant mass comfortable with zero and momenta of the electrons must be parallel at the CV. The resulting electron momentum can be quite asymmetrical because the two electrons do not equally share photon energy. This makes it possible that one or both of the electrons with low transverse momentum do not even reach the ECAL. That means using the tracker-only knowledge is a unique possibility for the reconstruction of the very low-energy photons.

4. ANALYSIS SETUP

4.1. Trigger Selection

The ability of selection of the Υ meson decaying into two oppositely signed muons ($\Upsilon(1S) \rightarrow \mu^+\mu^-$) is the first and important step for the reconstruction of the $X_b \rightarrow \Upsilon(1S)\pi^+\pi^-$ and $X_b \rightarrow \chi_{b1}(1P)\pi^+\pi^-$ final states. Two HLT paths before the 2017 data taking and at the beginning of 2018 data taking has been set up to select this meson. All of the HLT paths are shown below; number one is for the full 2016, number two is for the full 2017, and number three is for a start right after the beginning of 2018 data-taking.

1. **HLT_Dimuon8_Upsilon_Barrel**
   - $p_T(\mu^+\mu^-) > 7.9$ GeV
   - $m(\mu^+\mu^-) \in [8.5, 11.5]$ GeV
   - $|y(\mu^+\mu^-)| < 1.25$
   - The probability for the vertex fit of the two muons, $P_{vtx}(\mu\mu) > 0.5$ %
2. **HLT_Dimuon12_Upsilon_eta1p5**
   - $p_T(\mu^+\mu^-) > 11.9$ GeV
   - $m(\mu^+\mu^-) \in [8.5, 11.5]$ GeV
   - $|\eta(\mu)| < 1.5$
   - The probability for the vertex fit of the two muons, $P_{vtx}(\mu\mu) > 0.5$ %
3. **HLT_Dimuon12_Upsilon_y1p4**
   - $P_T(\mu^+\mu^-) > 11.9$ GeV
   - $m(\mu^+\mu^-) \in [8.5,\ 11.5]$ GeV
   - $|y(\mu^+\mu^-)| < 1.4$
   - The probability for the vertex fit of the two muons, P_{vtx} ($\mu\mu$)> 0.5 %

4.2. Data Samples

The CMS Collaboration reconstruction software is CMSSW which has the X_Y_Z versions. The CMSSW_9_4_7 is used for 2016 and 2017 datasets and the CMSSW_10_2_1 is used for the 2018 dataset,for the offline study in this thesis. The datasets used in this thesis are the whole dataset of events collected by CMS in 2016, 2017, and 2018 data-taking periods which is so-called Run II in pp collisions at $\sqrt{s}$ = 13 TeV. All these datasets are input into MuOnia primary Dataset to obtain the central prompt reconstruction. The events accepted by the HLT are streamed on disk, and they are grouped into a set of streams.

In the CMS, the Primary Datasets (PDs) are described via grouping a set of triggers that perform similar selections, the files are in MINIAOD format, where AOD means Analysis Object Data. For physics analysis, the MINIAOD includes some high-level physics objects such as muons, electrons, tracks, calorimetric clusters, vertices, etc. Moreover, it includes information about event selection and identification criteria for physics objects. This analysis was performed with the CMS MuOnia PD, which includes all the dimuon triggers. The integrated luminosity of the analyzed dataset is about 138.57 fb^{-1} for all 2016, 2017, and 2018 datasamples. Table 4.1. shows the list of data samples, and respective run ranges for the years 2016, 2017, and 2018.

Data Set	Run Range
/MuOnia /Run2016B-17Jul2018 ver2-v1/MINIAOD	273150 - 275376
/MuOnia/Run2016C-17Jul2018-v1/MINIAOD	275657 - 276283
/MuOnia/Run2016D-17Jul2018-v1/MINIAOD	276315 - 276811
/MuOnia/Run2016E-17Jul2018-v1/MINIAOD	277420 - 277305
/MuOnia/Run2016F-17Jul2018-v1/MINIAOD	277932 - 278808
/MuOnia/Run2016G-17Jul2018-v1/MINIAOD	278820 - 280385
/MuOnia/Run2016H-17Jul2018-v1/MINIAOD	281207 - 284068
/MuOnia/Run2017B-31Mar2018-v1/MINIAOD	297046 - 299329
/MuOnia/Run2017C-31Mar2018-v1/MINIAOD	299368 - 302029
/MuOnia/Run2017D-31Mar2018-v1/MINIAOD	302030 - 303434
/MuOnia/Run2017E-31Mar2018-v1/MINIAOD	303824 - 304797
/MuOnia/Run2017F-31Mar2018-v1/MINIAOD	305040 - 306462
/MuOnia/Run2018A-17Sep2018-v1/MINIAOD	315252 - 316995
/MuOnia/Run2018B-17Sep2018-v1/MINIAOD	317080 - 3s19310
/MuOnia/Run2018C-17Sep2018-v1/MINIAOD	319337 - 320065
/MuOnia/Run2018D-17Sep2018-v1/MINIAOD	320673 - 325175

Table 4.1. The official MuOnia datasets with the corresponding run ranges for 2016, 2017, and 2018 years data collected by the CMS experiment during Run II.

4.3. Monte Carlo Samples

The Monte Carlo (MC) samples have been produced at first privately and then officially for $\Upsilon(1S)\pi^+\pi^-$ and $\chi_{b1}(1P)\pi^+\pi^-$ final decays that were used in this analysis. These MCs were generated with the official RunIISummer16, RunIIFall17, and RunIIAutumn18 campaigns for 2016, 2017, and 2018, respectively. The list of simulated MC samples are given in Table 4.2. and Table 4.3. for $X_b \rightarrow \Upsilon(1S)\,\pi^+\pi^-$ and $X_b \rightarrow \chi_{b1}(1P)\pi^+\pi^-$ decays, respectively.

The MC events are generated using PYTHIA8. Since there is no X_b particle in the generator, signal samples are generated with a replacement of the mass of the χ_{b0} state. Generator-level filters have been applied to increase the production speed and MC efficiency. In these MC events, it is necessary that an X_b candidate decay to an $\Upsilon(1S)$ or a $\chi_{b1}(1P)$ particles in accordance with the decay of interest for the latter particle, forced decay is into $\Upsilon(1S)$ radiatively. Moreover, some criteria have been applied to approximately cover the whole acceptance of the detector. These criteria include the existence of at least two opposite-sign muons with pseudo-rapidity $|\eta| < 2.4$ and a minimum transverse momentum of 2.5 GeV and also a minimum transverse momentum of 0.5 GeV for generic tracks (Lezki, 2019).

M(X_b)[GeV]	**Monte Carlo**
X = 10.1, 10.3, 10.5, 10.7, 10.9,	chib0_ToUpsilon1SPiPi_ mX_TuneCUEP8M1_ 13TeV-pythia8-evtgen
11.1, 11.4, 11.7, 12.0	chib0_ToUpsilon1SPiPi_ mX_TuneCUEP8M1_ 13TeV-pythia8-evtgen

Table 4.2. The different generated X_b mass values in the produced simulated signal samples for $X_b \to \Upsilon(1S)\pi^+\pi^-$ decay.

M(X_b)[GeV]	**Monte Carlo**
X = 10.3, 10.5, 10.7, 10.9, 11.1,	chib0_ToUpsilon1SPiPi_ mX_TuneCUEP8M1_ 13TeV-pythia8-evtgen
11.4, 11.7, 12.0	chib0_ToUpsilon1SPiPi_ mX_TuneCUEP8M1_ 13TeV-pythia8-evtgen

Table 4.3. The official MC samples produced with 2016, 2017, and 2018 years data collected by the CMS experiment during Run II for $X_b \to \chi_{b1}(1P)\pi^+\pi^-$.

5. RECONSTRUCTION OF THE $\Upsilon(1S)\pi^+\pi^-$ FINAL STATE

In this chapter, the inclusive reconstruction of the $X_b \to \Upsilon(1S)\pi^+\pi^-$ candidates is described using CMS Run-II data. The strategy of this analysis is searching for a extra peak on the invariant mass spectra $\Upsilon(1S)\pi^+\pi^-$ ($\Upsilon(1S) \to \mu^+\mu^-$). If there is a definite peak in the spectra beyond signals predicted by the traditional hadron spectroscopy, the relative production cross-sections, and the yields could be measured. If no clear evidence of the signal is observed, it will be determined that there is no clear signal of X_b in the mass range examined for this final state. In the following sections, the reconstruction steps of the $\Upsilon(1S)\pi^+\pi^-$ final state is described in detail.

5.1. Event Selection with $\Upsilon(1S)$ Candidates

This section represents pre-selection applied at the level of the analyzer. The analyzer look for $X_b \to \Upsilon(1S)\pi^+\pi^-$ candidates for each event. It is trying to construct them by beginning with the reconstruction of the Υ candidates for each couple of oppositely charged muons existing in the event. The first step is that events are analyzed only if one of the following three trigger bits, which are already mentioned in Chapter 4. is fired, HLT_Dimuon8_Upsilon_Barrel, HLT_Dimuon12_Upsilon_eta1p5, HLT_Dimuon12_Upsilon_y1p4 since this analysis depends on the initial reconstruction of the $\Upsilon(1S) \to \mu^+\mu^-$ candidates. To reconstruct the $\Upsilon(1S)$ candidates, the official "soft muon" criteria given below are used in this analysis.

- the muon candidates should at least meet the quality reconstruction requirement "TMOneStationTight",
- the muon track needs to qualify as "high-purity" and must at least has 6 hits in the tracker layers, with at least one of them being in a pixel layer,

- the muon must be characterized by $|\eta| < 2.4$ and by a minimum transverse momentum of 4.0 GeV,
- the impact parameters $|dxy|$ and $|dz|$ of the muon tracks are required to be smaller than 3 cm and 30 cm, respectively (Lezki, 2019).

For each pair of muon with opposite charges, a Υ candidate is formed.The opposite-sign combinations of these muons, must initially fulfill that:

- the invariant mass must be in the mass window $8.6 < m(\mu^+\mu^-) < 11.4$ GeV,
- the P_T must be greater than 10 GeV,
- the vertex fit of the two muons with the geometrical constraint to originate from a common vertex must be not only valid but also have a vertex probability $P_{\chi^2}(\mu\mu)$ -vtx >1 % (ibid.).

To ensure that the muons of the selected combination are exactly those muons used at the trigger level to build the dimuon candidate, the trigger matching is applied to both muons of the selected pairs. In order to collect the three signals Υ(nS) with n = 1, 2, 3, the final selected $\mu^+\mu^-$ candidates, one per event, must be in the invariant mass of the range [9.1, 10.5] GeV. Moreover, in order to obtain results homogeneously it is necessary to apply these criteria: $|\eta(\mu\pm)| < 1.5$ and $P_T(\mu^+\mu^-) > 12$ GeV. Figure 5.1. shows the dimuon invariant mass distributions for the three years (2016, 2017, 2018), and the same three invariant mass distributions being superimposed after normalization and application of these two offline criteria is given in Figure 5.2..

5.2. Selection of $\Upsilon(1S)\pi^+\pi^-$ candidates

The next step after each selected Υ candidate is to combine any two additional, oppositely charged, tracks. The tracks must be different from the inner tracker track of the muon candidates used to create the Υ candidate. In order to reproduce the track acceptance offline, it is necessary to apply $P_T > 0.5$ GeV criteria. In this analysis, all

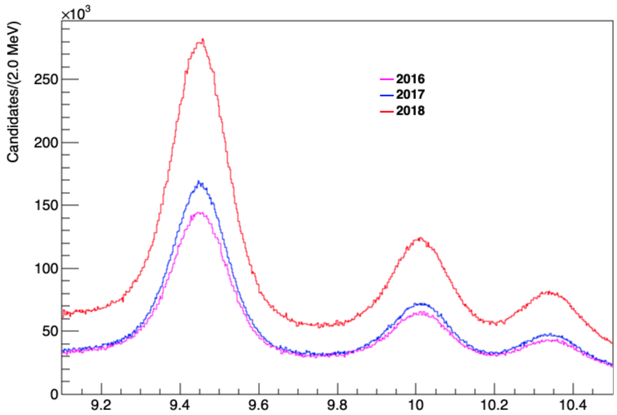

Figure 5.1. The superimpose distribution of dimuon mass for the 3 years of the Run-II data taking, after applying trigger matching and $|\eta(\mu\pm)| < 1.5$ and $P_T(\mu^+\mu^-) > 12$ GeV

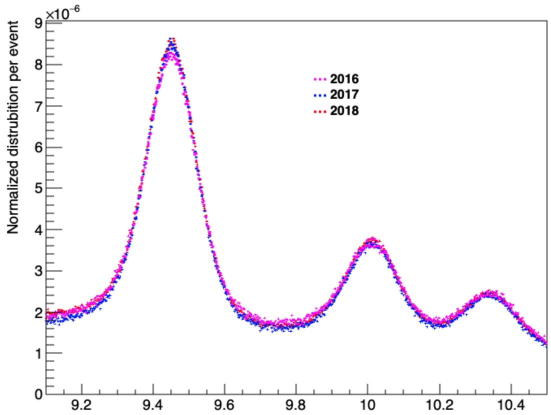

Figure 5.2. The normalized distribution of dimuon mass for the 3 years of the Run-II data taking, after applied trigger matching and $|\eta(\mu\pm)| < 1.5$ and $P_T(\mu^+\mu^-) > 12$ GeV

tracks except muons are accepted to be pions. These pion candidates should fulfill the following criteria:

- the pion candidates must pass standard high-quality and purity track requirements, to have at least 1 pixel hits, at least 5 tracker hits,
- each pion must have ΔR with respect to $\Upsilon(1S)$ candidates, less than 0.7 (the vast majority of pions meet this requirement),
- any considered dipion must have an invariant mass of less than 1.6 GeV (Lezki, 2019).

At the analyzer level, using the KinematicConstraintVertexFitter algorithm included in a standard CMSSW vertexing package, a $\mu^+\mu^-\pi^+\pi^-$ vertex fit with a geometric and kinematic constraint is achieved. This constraint is the refitted of two muons to ensure a $\Upsilon(1S)$ candidate to be mass constrained so that to have a nominal mass $M_{\Upsilon(1S)}$. To significantly improve resolution in the $\mu^+\mu^-\pi^+\pi^-$ mass reconstruction, the $\Upsilon(1S)$ mass constraint is also applied. Figure 5.1. shows the $\Upsilon(1S)\pi^+\pi^-$ invariant mass distribution in [9.8, 12.5] GeV range. In addition to these offline criteria, which are named baseline selection, it is also required to apply the other two criteria as offline. The first one is that the vertex fit probability is required to be greater than 5% to reject fake combinations. The second one is [9.3, 9.6] GeV mass window that $\Upsilon(1S)$ candidates are selected used to build the $\Upsilon(1S)\pi^+\pi^-$ candidates. The invariant mass distribution of $\Upsilon(1S)\pi^+\pi^-$ candidates after applying the vertex probability greater than 5% and the narrower [9.3, 9.6] GeV mass window for Υ candidates with baseline selection is given in Figure 5.4.. It can be clearly seen that the number of candidates per event, which called multiplicity is still higher even after applying all these offline criteria. All of the offline selections for muon pairs ($\Upsilon(1S)$), pion pairs and the 4-track candidates ($\Upsilon(1S)\pi^+\pi^-$) are summarized in Table 5.1.

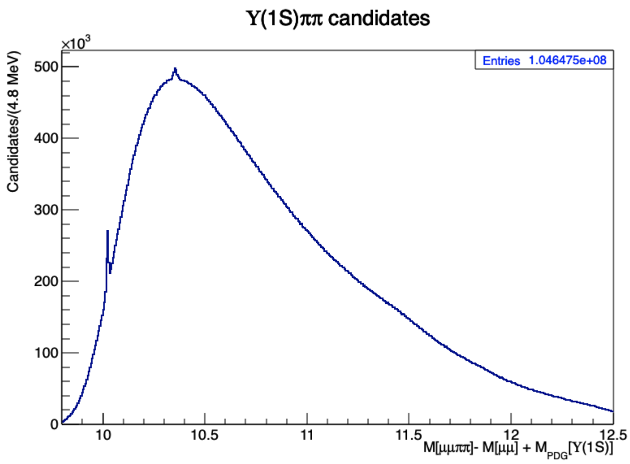

Figure 5.3. The invariant mass distribution of $\Upsilon(1S)\pi^+\pi^-$ candidates after applying the baseline selection

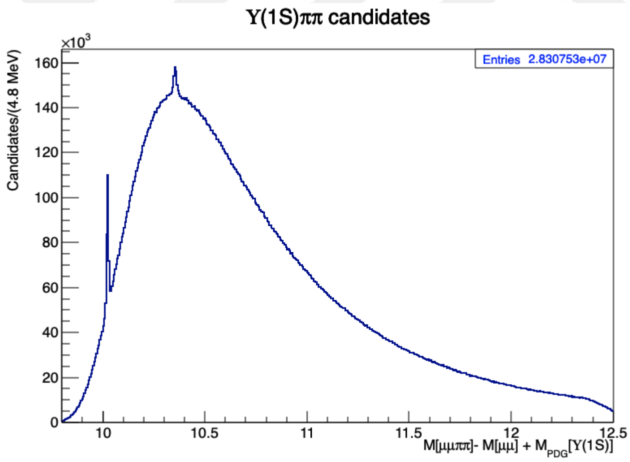

Figure 5.4. The invariant mass distribution of $\Upsilon(1S)\pi^+\pi^-$ candidates after applying the vertex probability greater than 5% and the narrower [9.3, 9.6] GeV mass window for Υ candidates with baseline selection

Source	Selections
inner-Tracker	numberOfValidStripHits $\geq$ 5 numberOfValidPixelHits $\geq$1 $P_T(\pi^{\pm}) > 0.5$ GeV $\|\eta(\pi^{\pm})\| < 2.5$ GeV
Track pair	Opposite charge sign pion P_T> 0.5GeV $M(\pi^+\pi^-) < 1.6$ GeV
$\mu^+\mu^-$ pair	9.3 GeV $< M_{\mu^+\mu^-} <$ 9.6 GeV $\|\eta(\pi^{\pm})\| < 1.5$ GeV $P_T(\mu^+\mu^-) > 12$ GeV
$\mu^+\mu^-\pi^+\pi^-$	Constrained fit probability > 5 % 9.8 GeV $< M_{\Upsilon(1S)\pi^+\pi^-} <$ 12.2 GeV

Table 5.1. All selection criteria for pions, $\pi^+\pi^-$ pairs, $\mu^+\mu^-$ pairs, and $\Upsilon(1S)\pi^+\pi^-$ candidates.

Figure 5.5. shows the distribution of the $\Upsilon(1S)$ candidates after applying the baseline selection. These $\Upsilon(1S)$ candidates are used to build a candidate in the$\Upsilon(1S)\pi^+\pi^-$mass spectrum within the mass window [9.8,12.5] GeV. This mass window criterion is necessary to obtain a pure sample of $\Upsilon(1S)$ candidates by cleaning up the fake $\Upsilon(1S)$ candidates completely by rejecting the sidebands. The superimposed and normalized distributions of the invariant mass of the $\Upsilon(1S)$ candidates used to build a $\Upsilon(1S)\pi^+\pi^-$ candidate for the three years of the Run-II data-taking are given in Figure 5.6. and 5.7., respectively.

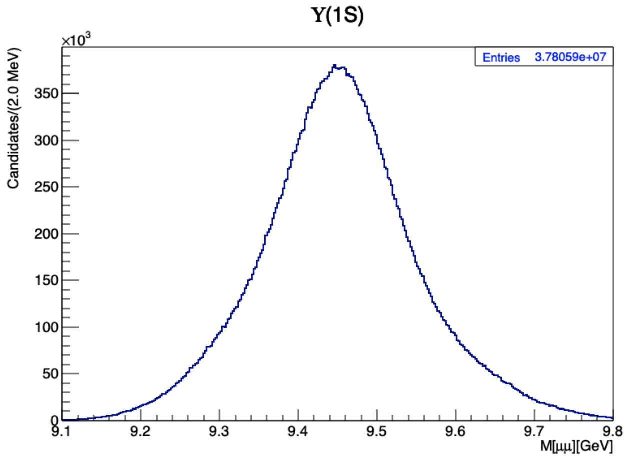

Figure 5.5. The invariant mass distribution of the $\Upsilon(1S)$ candidates used to build a $\Upsilon(1S)\pi^+\pi^-$ candidate

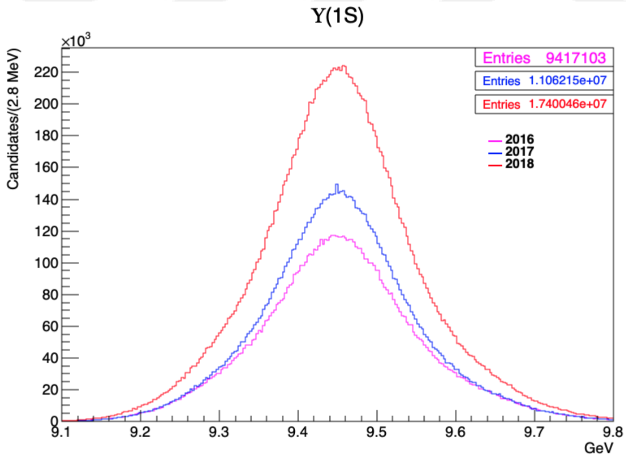

Figure 5.6. The superimposed distribution of invariant mass of the $\Upsilon(1S)$ candidates used to build a $\Upsilon(1S)\pi^+\pi^-$ candidate for the 3 years of the Run-II data taking.

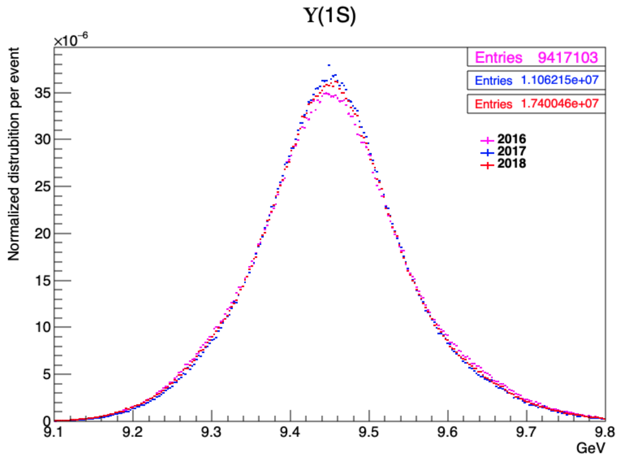

Figure 5.7. The normalized distribution of invariant mass of the $\Upsilon(1S)$ candidates used to build a $\Upsilon(1S)\pi^+\pi^-$ candidate for the 3 years of the Run-II data taking

5.3. The Study of Combinatorial Background Because of the Pions

After the reconstruction of $\Upsilon(1S)\pi^+\pi^-$, there is the background in the invariant mass distribution of the $\Upsilon(1S)\pi^+\pi^-$ final state (see Figure 5.3.). This background is essentially combinatorial and exists due to the so-called "pion-pollution" namely the large number of tracks (mostly pions) characterizing the LHC proton-proton collisions. The combinatorial nature of this background has been checked by comparing the distribution for wrong sign combinations (the two combined pions have the same charge, either positive or negative) with the previous distribution (right-sign one).

According to the value of their P_T, we can order the first and second pion from the two opposite-signed pions pair and re-label them as leading and soft pions, respectively. The minimum P_T of both of them is 0.5 GeV. The P_T distributions for the leading and the soft pions are given in Figure 5.8.. And the $\Upsilon(1S)\pi^+\pi^-$ invariant mass distribution without applying leading pion P_T greater than 0.7 and soft pion P_T greater than 0.5 is given in Figure 5.9.. It is clearly seen the effect of these cuts from the difference of event number between Figure 5.3. and Figure 5.9..

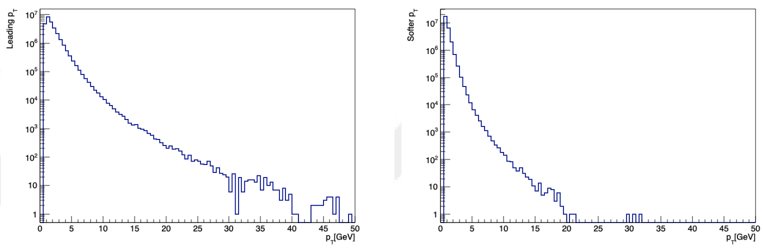

Figure 5.8. The distributions of the P_T of the leading pion (left) and soft pion (right).

An "in situ" study of the change of 1) shape of the $\Upsilon(1S)\pi^+\pi^-$ invariant mass spectrum, and 2) the yield of the $\Upsilon(2S)$ signal when applying different minimum P_T-cuts to both pions, has been carried out. The soft (leading) pion threshold has been raised from 0.5 GeV to 0.7(0.8) GeV progressively. A change in the shape of the spectrum shape is shown in Figure 5.10. (where the different distributions are just superimposed). Combinations of stronger cuts have been explored, and it was found that they would imply a relevant distortion of the whole spectrum shape and thus have not been further investigated.

The change in yield and statistical significance of the $\Upsilon(2S)$ signal has been studied with the following method. The signal and background yields are estimated by fitting each time the invariant mass distribution of $\Upsilon(1S)\pi^+\pi^-$ for different combi-

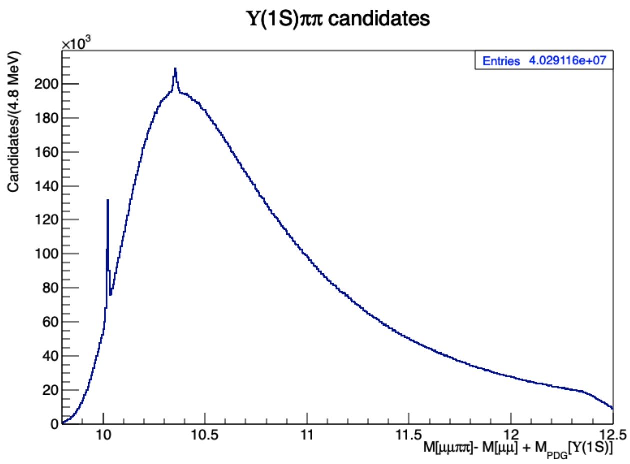

Figure 5.9. The invariant mass distribution of $\Upsilon(1S)\pi^+\pi^-$ without applying leading pion P_T greater than 0.7 and soft pion P_T greater than 0.5

nations of P_T-cuts inside a $\Upsilon(2S)$ peak region coherently defined. The invariant mass distribution of the $\Upsilon(1S)\pi^+\pi^-$ in the $\Upsilon(2S)$ region, as an example, after requiring P_T(L/S)> 0.5 GeV for both leading/soft pion is shown in Figure 5.11.

Tables 5.2., 5.3. and 5.4. report yield (S), statistical significance $S^2/(S+B)$ and purity S/(S+B) for each of the different requirements of minimum P_T values that have been investigated; the statistical significance and purity have been calculated in a 2σ signal window around the fitted $\Upsilon(2S)$ mass value.

As a working point, it has been chosen to require $P_T(L) > 0.7$ GeV and $P_T(S) > 0.5$ GeV by considering it as a compromise between the reduction of the statistical significance and the increase of purity. This choice is clearly sub-optimal, but it does not show a sculpting effect (see Figure 5.10.) and retains most of the signal yield. Afterward, the multiplicity level (number of candidates per event) has been evaluated (reported in Figure 5.12.). This level appears to be still very high, and a

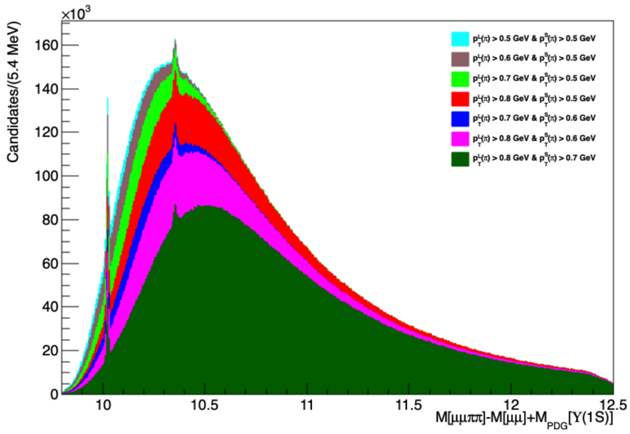

Figure 5.10. The “sculpting” effect of the minimum-P_T values for both leading and soft pions on the $\Upsilon(1S)\pi^+\pi^-$ invariant mass spectrum

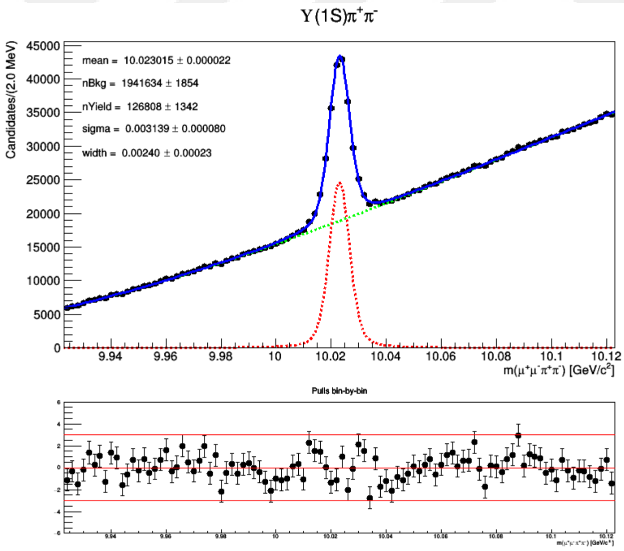

Figure 5.11. The invariant mass distribution of $\Upsilon(1S)\pi^+\pi^-$ when requiring $P_T > 0.5$ GeV for both the leading and the soft pions

dedicated study needs to be carried out to get rid of multiple candidates since only one candidate per event can be the correct one.

Minimum-P_T [GeV]		**Yield**
leading pions	soft pions	$\Upsilon(2S)\rightarrow\Upsilon(1S)\pi^+\pi^-$
0.5	0.5	127785
0.6	0.5	122898
0.7	0.5	111674
0.7	0.6	80584
0.8	0.5	96751
0.8	0.6	72164
0.8	0.7	51328

Table 5.2. The yields of $\Upsilon(2S)$ in $\Upsilon(1S)\pi^+\pi^-$ invariant mass spectrum for different minimum-P_T values of the two pions

Minimum-P_T [GeV]		**Statistical Significance**
leading pions	soft pions	$\Upsilon(2S)\rightarrow \Upsilon(1S)\pi^+\pi^-$
0.5	0.5	49085
0.6	0.5	48937
0.7	0.5	47819
0.7	0.6	37802
0.8	0.5	44208
0.8	0.6	35595
0.8	0.7	26866

Table 5.3. The statistical significance of $\Upsilon(2S)$ in $\Upsilon(1S)\pi^+\pi^-$ invariant mass spectrum for different minimum-P_T values of the two pions.

Minimum-P_T [GeV]		Purity
leading pions	soft pions	$\Upsilon(2S) \rightarrow \Upsilon(1S)\pi^+\pi^-$
0.5	0.5	0.38
0.6	0.5	0.39
0.7	0.5	0.42
0.7	0.6	0.46
0.8	0.5	0.45
0.8	0.6	0.49
0.8	0.7	0.52

Table 5.4. The purtiy of $\Upsilon(2S)$ in$\Upsilon(1S)\pi^+\pi^-$ invariant mass spectrum for different minimum-P_T values of the two pions.

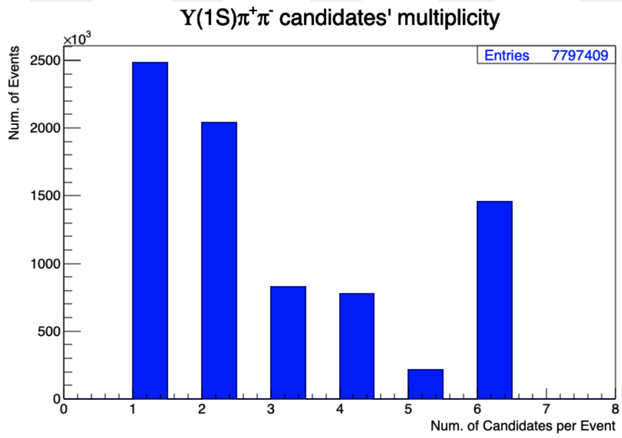

Figure 5.12. Multiplicity of $X_b \rightarrow \Upsilon(1S)\pi^+\pi^-$ candidates after the cut-based event selection. The first column to the right indicates a number equal or more than 6

5.4. Study of the Elimination of Multiple Candidates in $\Upsilon(1S)\pi^+\pi^-$ Spectrum

In order to eliminate the combinations due to fake dipions, there are two selection criteria that can be generally applied (on top of the cut-based selection adopted so far, that will be called later "baseline"):

1. choose the candidate in the event having the highest P_T value,

2. choose the candidate in the event with the highest vertex fit probability (of the two muons and the two pions building up the candidate).

Figure 5.13. shows the invariant mass distribution of the $\Upsilon(1S)\pi^+\pi^-$ after applying the criterion of choosing the candidate in the event with the highest P_T value. Instead, Figure 5.14. presents the invariant mass distribution of the $\Upsilon(1S)\pi^+\pi^-$ after applying the criterion of choosing the candidate in the event with the highest vertex fit probability.

The performances of these two criteria need to be studied exploiting simulated samples, in terms of figures-of-merit such as efficiency and purity, to choose the most effective one between them. In the following study, the signal MC sample with generated X_b mass value of 10.7 GeV has been used.

The reconstructed invariant mass distribution of the $\Upsilon(1S)\pi^+\pi^-$ candidates with and without the application of the MC truth-matching requirement is given in Figure 5.15.. The reconstructed and true (truth-matched) signal candidates are counted within the mass signal window [10.67, 10.73] GeV. Figure 5.16. shows the reconstructed invariant mass distribution of the $\Upsilon(1S)\pi^+\pi^-$ candidates before and after the application of the selection criterion of the highest-P_T candidate in the event, whereas Figure 5.17. illustrates the reconstructed invariant mass distribution of the $\Upsilon(1S)\pi^+\pi^-$ candidates before and after the application of the selection criterion of the highest vertex fit probability candidate in the event.

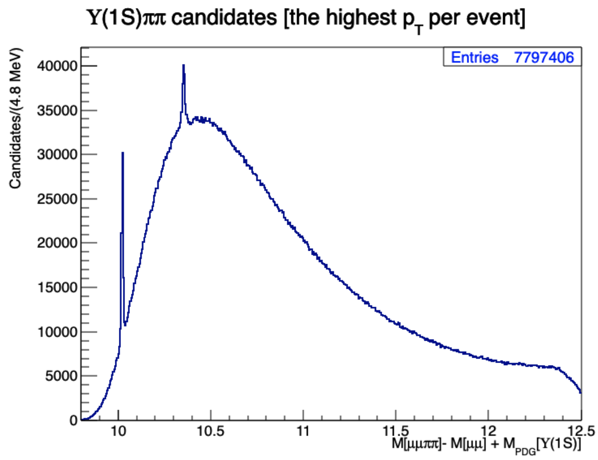

Figure 5.13. The invariant mass distribution the $\Upsilon(1S)\pi^+\pi^-$ after applying the criteria of choosing the candidate the highest P_T value in the event.

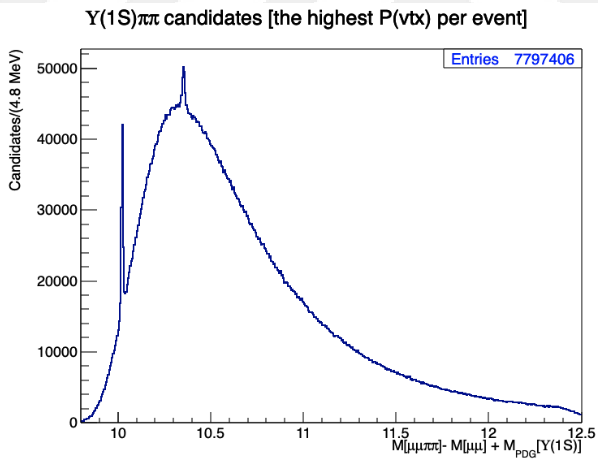

Figure 5.14. The invariant mass distribution the $\Upsilon(1S)\pi^+\pi^-$ after applying the criteria of choosing the candidate the highest vertex fit probability in the event.

For both multiplicity rejection criteria, the signal efficiency ε_{cut} and the fake rate are reported in Table 5.5.. They are respectively calculated, in the mass signal window [10.67, 10.73] GeV, as ratios of true and fake candidates with respect to all candidates, before and after applying a criterion. It is evident from the numbers in Table 5.5., the result of this study is that the choice of the highest-P_T candidate in the event is better performing than the choice of the highest vertex probability candidate in the event.

	Baseline Selection	Highest P_T Selection	Highest P(vtx) Selection
Total	3675	2366	1711
True	2899	2176	1533
Fake	776	190	178
Fake Rate %	21.11	**8.03**	**10.40**
ε_{cut} %		**75.06**	**52.88**

Table 5.5. The comparison of the differences in the fake rate and the efficiency of the two criteria

For illustration purposes, the invariant mass distribution of the $\Upsilon(1S)\pi^+\pi^-$ best candidate per event, in the $\Upsilon(2S)$ region, is shown in Figure 5.18.. The fitted value of the $\Upsilon(2S)$ is consistent with the PDG average mass value.

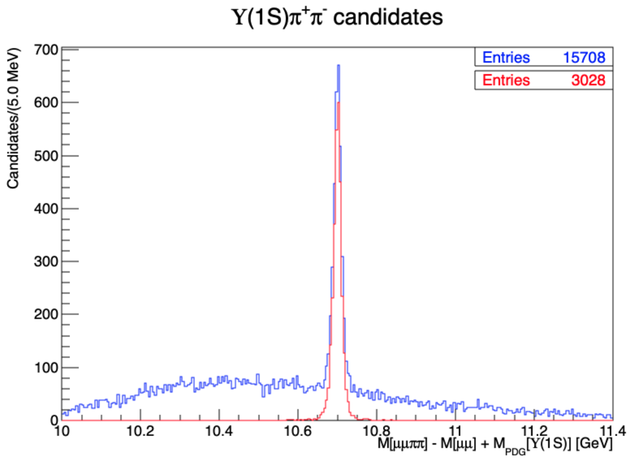

Figure 5.15. The invariant mass distribution of $\Upsilon(1S)\pi^+\pi^-$ candidates obtained by analyzing the signal MC sample with generated $m(X_b)$ = 10.7 GeV. The blue/red lines represent the reconstructed candidates before/after applying the MC truth matching requirement

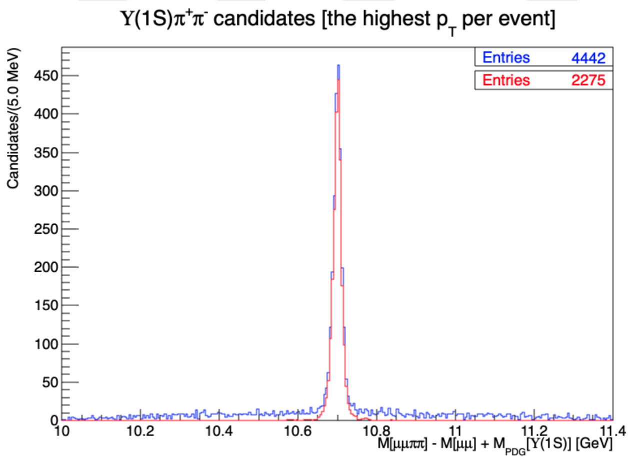

Figure 5.16. The invariant mass distribution of $\Upsilon(1S)\pi^+\pi^-$ candidates obtained by analyzing the MC sample with generated mass value $m(X_b)$ = 10.7 GeV. The blue/red lines represent reconstructed candidates and truth-matched candidates after choosing the candidate with the highest P_T value in the event

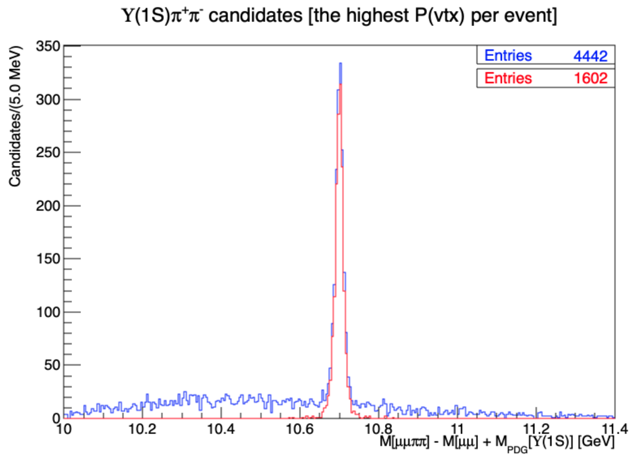

Figure 5.17. The invariant mass distribution of $\Upsilon(1S)\pi^+\pi^-$ candidates obtained by analyzing the MC sample with generated mass value $m(X_b) = 10.7$ GeV. The blue/red lines represent reconstructed candidates and truth-matched candidates after choosing the candidate with the highest vertex fit probability in the event

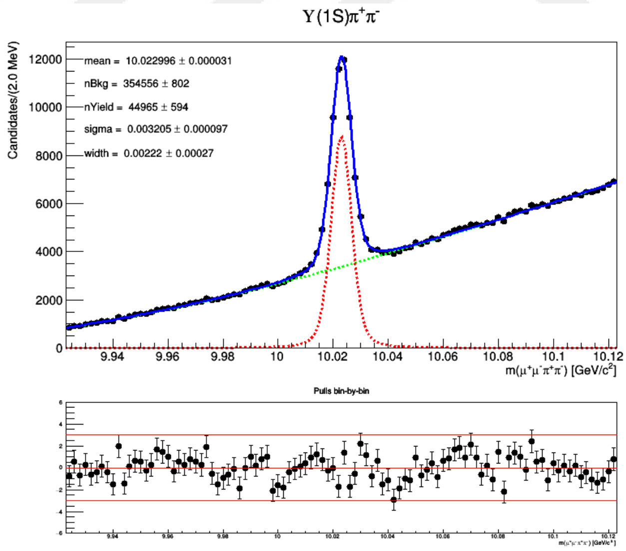

Figure 5.18. The invariant mass distribution of the $\Upsilon(1S)\pi^+\pi^-$ candidates, in the $\Upsilon(2S)$ region, after selecting the highest-P_T candidate per event

5.5. Full Mass Spectra Resolution Study for $\Upsilon(1S)\pi^+\pi^-$ Final State

Simulated samples (reported in Table 4.2. in Chapter 4.) with different run conditions (corresponding to 2016, 2017, and 2018 data taking) have been used to extract the experimental mass resolutions and the reconstruction efficiencies as a function of the mass, for the $\Upsilon(1S)\pi^+\pi^-$ final state (9 generated mass values for the hypothetical X_b particle). The simulated signals have been studied after applying the MC truth matching. In order to obtain each fitted distribution, the Double Gaussian fit was used by superimposing the two components and sharing the same mean. These distributions for three years and 9 generated mass values are given in Appendix A. In order to illustrate, Figures 5.20. shows the fitted distributions of the invariant mass $\Upsilon(1S)\pi^+\pi^-$ after MC truth matching for 2018 MC data and 12.0 GeV mass. Figure 5.20. summarizes the results for $\Upsilon(1S)\pi^+\pi^-$ final state. Fits (one for each year) are superimposed to the data for the sets of simulated masses obtained after applying MC truth matching. These results extrapolated to the whole mass spectrum are crucial in extracting the Upper Limits in the X_b production cross-sections as a further study.

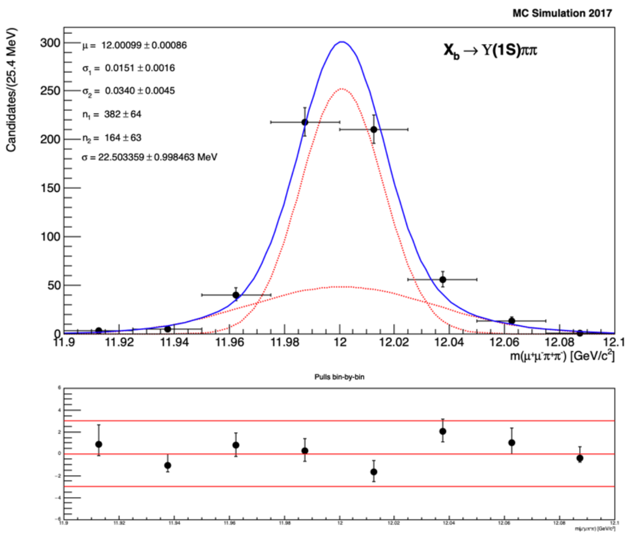

Figure 5.19. The fitted distributions of the invariant mass $\Upsilon(1S)\pi^+\pi^-$ after MC truth matching for 2018 MC data and 12.0 GeV mass.

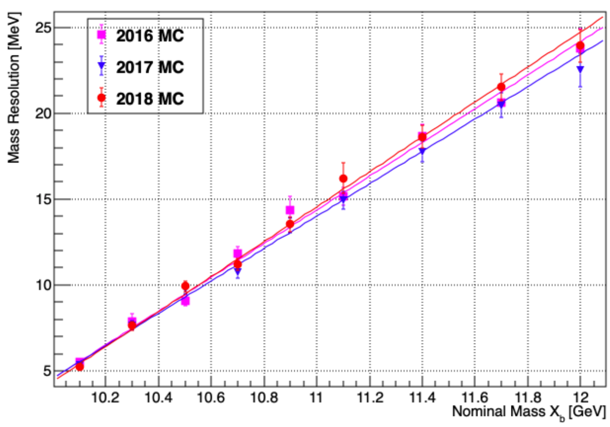

Figure 5.20. Fits to the mass resolution as a function of the mass for the $\Upsilon(1S)\pi^+\pi^-$ final state

5.6. Comparison Between Data and MC Samples for $\Upsilon(1S)\pi^+\pi^-$ Final State

This study has been performed to be sure that there are no remarkable discrepancies between the data and MC events. The simulated signal sample which is used for this study is the generated $m(X_b)$ = 10.7 GeV. If remarkable discrepancies between data and MC events are found, it might be required to think about modifying the output of the MC simulation which is called the re-weighting procedure for the $X_b \rightarrow \Upsilon(1S)\pi^+\pi^-$ decay mode. The P_T and η comparisons between data and MC events, after applying all the selection criteria for $\Upsilon(1S)\pi^+\pi^-$, $\Upsilon(1S)$, leading π, softer π and $\pi^{\pm}$, are given in Appendix B. In order to illustrate, the comparison between data and MC events for $\Upsilon(1S)\pi^+\pi^-$ P_T and η distributions are given in Figure 5.21. and 5.22.,respectively. As can be seen from the comparison distributions,there are no remarkable discrepancies between data and MC events.

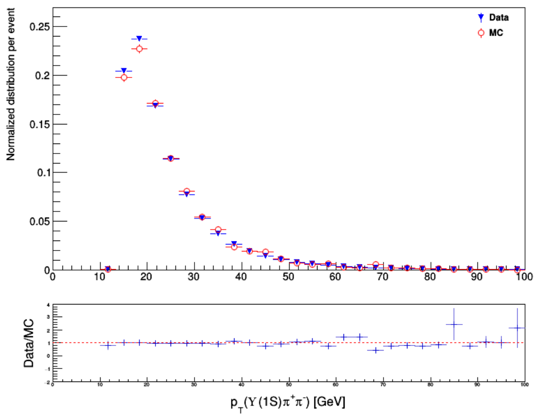

Figure 5.21. The comparison between data and MC events for $\Upsilon(1S)\pi^+\pi^-$ P_T distribution

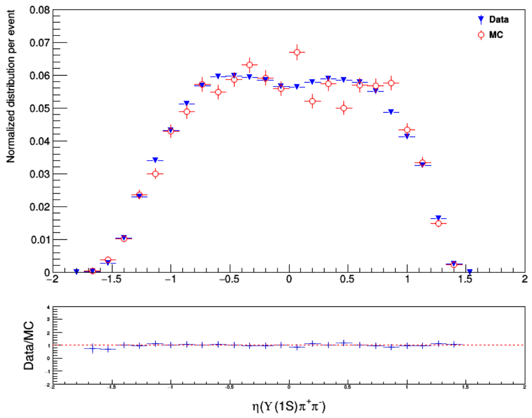

Figure 5.22. The comparison between data and MC events for $\Upsilon(1S)\pi^+\pi^-$ η distribution

6. RECONSTRUCTION OF THE $\chi_{b1}(1P)\pi^+\pi^-$ FINAL STATE

In this chapter, the inclusive reconstruction of the $X_b \rightarrow \chi_{b1}(1P)\pi^+\pi^-$ candidates is described using the CMS Run-II data. Searching for an extra peak on the invariant mass spectra $\chi_{b1}(1P)\pi^+\pi^-$ ($\chi_{b1}(1P) \rightarrow \Upsilon(1S)\gamma$) is the strategy of this analysis. If there is a definite peak in the spectra beyond signals predicted by the traditional hadron spectroscopy, the relative production cross-sections, and the yields could be measured. If no clear evidence of the signal is observed, it will be determined that there is no clear signal of X_b in the mass range examined for this final state. In the following sections, the reconstruction steps of the $\chi_{b1}(1P)\pi^+\pi^-$ final state is described in detail.

6.1. Selection of the $\chi_{b1}(1P)\pi^+\pi^-$ Candidates

The candidates of $\chi_{b1}(1P)$ are reconstructed by combining the selected Υ (as explained in the previous sections) with a converted photon ($\gamma \rightarrow e^+e^-$). And then the candidate of $\chi_{b1}(1P)\pi^+\pi^-$ is reconstructed by combining a $\chi_{b1}(1P)$ candidate with two tracks. In the following sections, the reconstruction of the converted photons and $\chi_{b1}(1P)$ will be explained.

6.1.1. Photon Reconstruction

The energies of the photons involved in X_b decays are relatively low. And this makes the investigation of photons converted to electron-positron pairs the most complex step in the whole reconstruction. Since the reconstruction efficiency is very low, a few percent, it leads to a strong reduction in the number of candidates available for the final state $\chi_{b1}(1P)\pi^+\pi^-$ in this analysis. The mass resolution of the χ_b candidates is excellent. This excellent resolution achieved by the reconstruction of the converted photons in the tracker volume. As mentioned in chapter 3, photon conversions are described by an electron-positron pair that come from the photon conversion vertex. Most of these tracks can be stopped before arriving at the calorimeter due to their low-P_T and they can be asymmetric. So, an algorithm that uses only tracker information to reconstruct these tracks is necessary. This algorithm depends on the capabilities and features of repetitive tracking in order to efficiently reconstruct the low-P_T and displaced tracks as those coming from a typical photon conversion. In this analysis, high purity conversions that meet the following criteria are used as the official standard:

- the two tracks must have opposite charge,
- the two tracks must have at least 4 and 3 hits, respectively, in the tracker,
- the difference in the z coordinate (Δz) of the innermost hits must be less than 5 cm,
- the reduced χ^2 of their track fit must be less than 10,
- the χ^2 probability of the kinematic fit to a common vertex must be more than 5×10^{-4},
- the two tracks should be characterized by a small angular separation: $\Delta\Phi < 0.2$ and $\Delta(\cot\theta) < 0.1$,
- the transverse distance of minimum approach (in the xy plane), d_{xy}, must satisfy the condition -0.25 cm $< d_{xy} <$ 1 cm,
- the signed impact parameter d_0 multiplied by the charge must be positive: $d_0 \cdot q > 0$ (Sanchez et al., 2017).

6.1.2. Reconstruction of the χ_b(1P)

In order to build χ_b(1P) candidates, for each event, the selected Υ candidate and the converted photons are matched. For this match, the following criteria must be met:

- the *dz* of the photon with respect to the dimuon vertex, i.e. the distance in the direction parallel to the *z-axis* between the dimuon vertex and the extrapolation of the photon direction to the beam-line, is required to be less than 5 mm,
- the per-event mass difference, or *Q-value*, $Q = m(\mu\mu\gamma) - m(\mu\mu)$, must be less than 1 GeV,
- the conversion radius must be $\rho_{conv} > 1.5$ cm, to suppress the background due to track pairs originating in the interaction point, caused by π^0 Dalitz decays (Lezki, 2019).

In order to reconstruct the photon conversions, they should happen in the one-two innermost pixel layers as can be seen in the distribution along the radial dimension of the photon conversion vertices, which is given in Figure 6.1.. Increasing the number of pixel layers between 2016 and 2017 are clearly visible from this figure. It can be clearly seen that the photon reconstruction efficiency is relatively low for photons with energies less than 400 MeV from the photon energy distribution, which is given in Figure 6.2.. Figure 6.3. shows the $\mu\mu$ invariant mass distributions, and Figure 6.4. shows its normalized distribution after the baseline criteria have been applied to dimuon candidates. Invariant mass distribution of the Υ(1S) candidates used to build the χ_b(1P) candidates by combining with the converted photons is given in Figure 6.5. and its normalized distribution is given in Figure 6.6. for the three years of data taking periods. And finally, the signal fit to the invariant mass distribution $\chi_{b1,2}$(1P) obtained from the Run-II data is given in Figure 6.7.

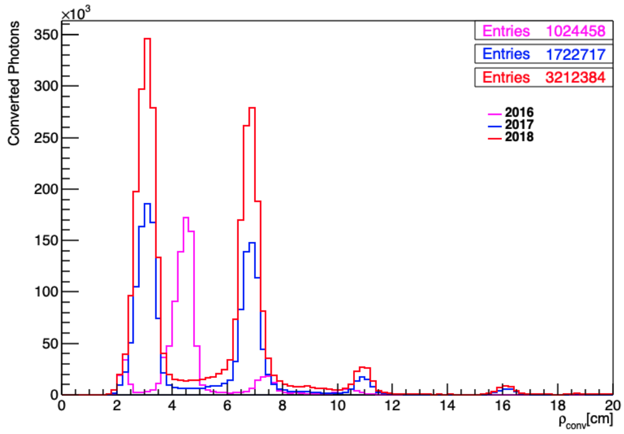

Figure 6.1. The distribution of the radial coordinate of the photon conversion vertices without applying requirements on the dimuon candidate for the three years of data taking periods

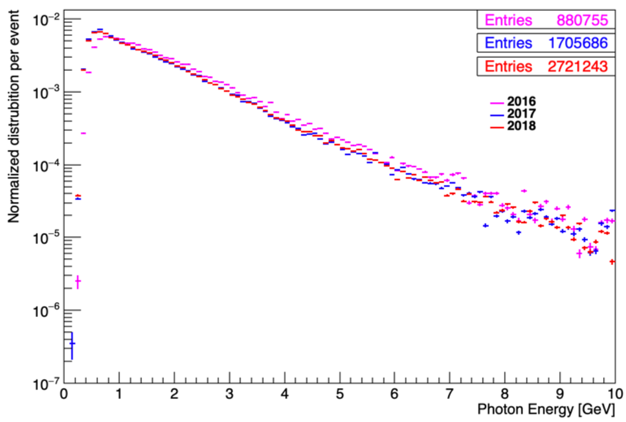

Figure 6.2. Energy distributions of the converted photons, after passing the trigger matching requirement of the Run-II data taking and applying $|\eta(\mu\pm)| < 1.5$ and $P_T(\mu^+\mu^-) > 12$ GeV criteria

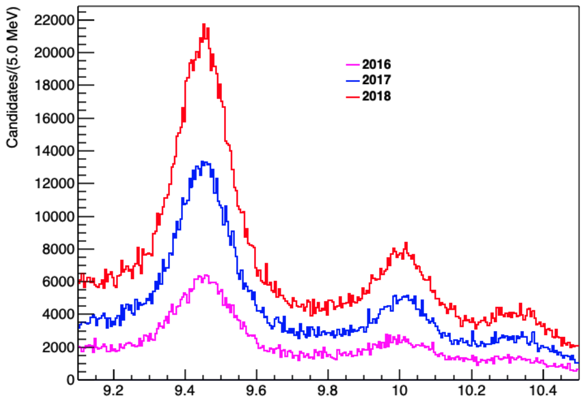

Figure 6.3. The Dimuon mass distribution after applying the trigger matching requirement and $|\eta(\mu\pm)| < 1.5$ and $P_T(\mu^+\mu^-) > 12$ GeV criteria

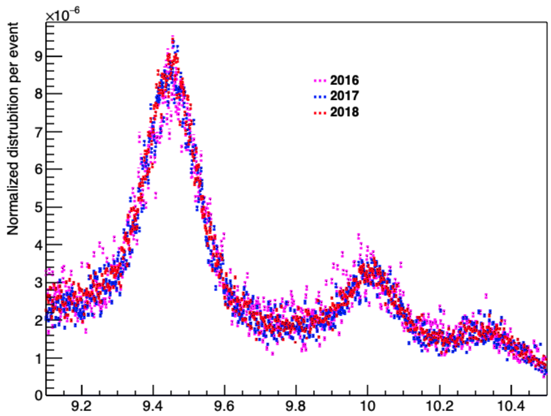

Figure 6.4. The superimpose distribution of the Dimuon mass, after applying the trigger matching requirement $|\eta(\mu\pm)| < 1.5$ and $P_T(\mu^+\mu^-) > 12$ GeV criteria and proper relative normalisation

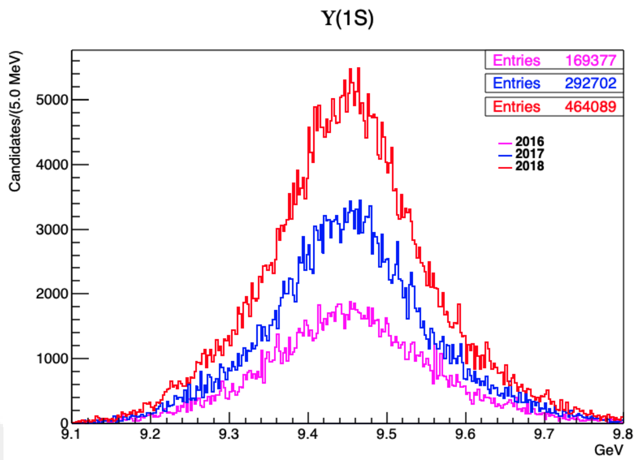

Figure 6.5. The superimpose distribution of invariant mass of the $\Upsilon(1S)$ candidates used to build $\chi_b(1P)$ candidates after applied the trigger matching requirement and $|\eta(\mu\pm)| < 1.5$ and $P_T(\mu^+\mu^-) > 12$ GeV criteria

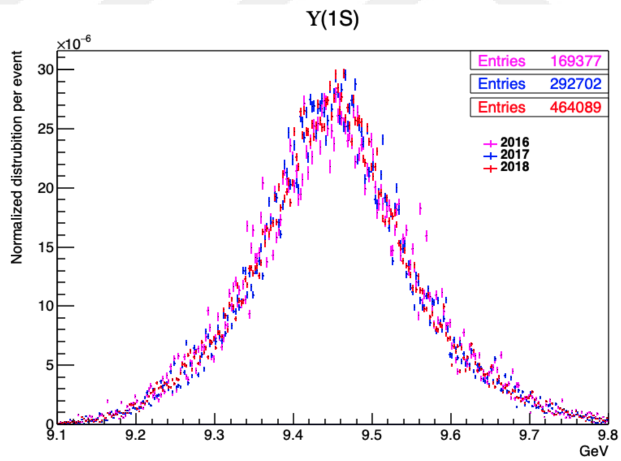

Figure 6.6. The superimpose distribution of invariant mass of the $\Upsilon(1S)$ candidates used to build $\chi_b(1P)$ candidates after applied the trigger matching requirement and $|\eta(\mu\pm)| < 1.5$ and $P_T(\mu^+\mu^-) > 12$ GeV criteria and proper relative normalisation

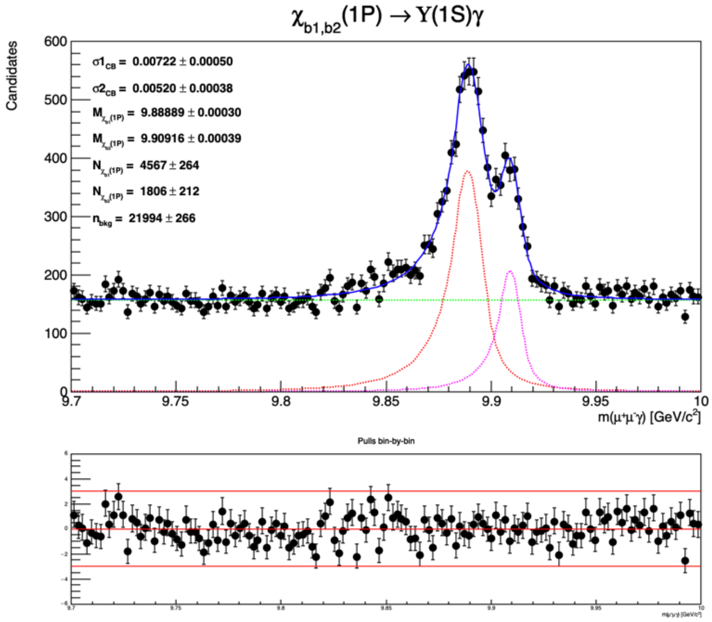

Figure 6.7. The signal fit to the invariant mass distribution $\chi_{b1,2}(1P)$ obtained from the Run-II data

6.1.3. Reconstruction of the χ_b(1P)$\pi\pi$

After combining the χ_b(1P) candidate with two oppositely charged pions the additional pions were selected from leading pions with $P_T > 0.7$ GeV and soft pions with $P_T > 0.5$ GeV. At the analyzer level, using the KinematicConstraintVertexFitter algorithm included in a standard CMSSW vertexing package, a $\mu^{+}\mu^{-}\pi^{+}\pi^{-}$ vertex fit with a geometric constraint together with the mass constraint of a χ_b(1P) candidate is achieved. The final candidate is obtained in [10, 12.5] GeV invariant mass range. In order to reject the fake combinations, the final vertex fit probability is again required to be greater than 5%. Most of the combinatorial background in the dimuon mass spectrum is eliminated by applying this vertex probability cut. And to reconstruct the χ_b(1P) candidates with only Υ(1S) candidates the [9.3, 9.6] GeV mass window are used. All these baseline selection criteria are summarised in Table 6.1.. While Figure 6.8. shows the distributions of the χ_b(1P)$\pi\pi$ invariant mass after applied baseline selection, Figure 6.9. shows the level of multiplicity. It is clearly visible that the level of multiplicity is still quite high even after applying the baseline selection.

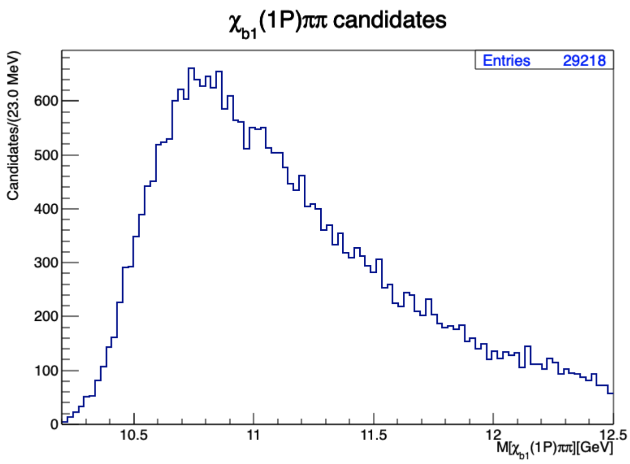

Figure 6.8. The invariant mass distribution of $\chi_b(1P)\pi\pi$ candidates after baseline selection

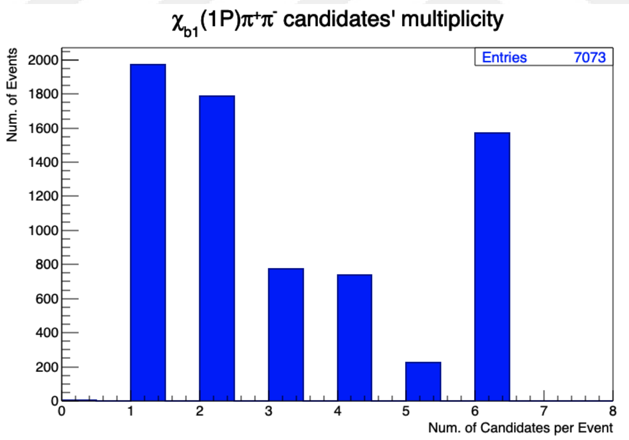

Figure 6.9. Multiplicity of $X_b \rightarrow \chi_b(1P)\pi\pi$ candidates after the event selection

Source	Selections
inner-Tracker	numberOfValidStripHits $\geq$ 5 numberOfValidPixelHits $\geq$1 $P_T(\pi^\pm) > 0.5$ GeV $\|\eta(\pi^\pm)\| < 2.5$ GeV
Track pair	Opposite charge sign P_T(Leading π) > 0.7 GeV P_T (Softer π) > 0.5 GeV $M(\pi^+\pi^-) < 1.6$ GeV
$\mu^+\mu^-$ pair	9.3 GeV $< M_{\mu^+\mu^-} <$ 9.6 GeV $\|\eta(\pi^\pm)\| < 1.5$ GeV $P_T(\mu^+\mu^-) > 12$ GeV
$\chi_b(1P)$	9.87 GeV $< M_{\mu^+\mu^-\gamma} <$ 9.902 GeV
$\mu^+\mu^-\gamma\pi^+\pi^-$	Constrained fit probability > 5 % Energy(γ) > 400 GeV

Table 6.1. All selection criteria for pions, $\pi^+\pi^-$ pairs, $\mu^+\mu^-$ pairs, $\chi_b(1P)$ and $\chi_b(1P)\pi\pi$ candidates.

6.2. Study of the Elimination of Multiple Candidates in $\chi_b(1P)\pi\pi$ Spectrum

A similar study with the $\Upsilon(1S)\pi\pi$ final state given. in section 5.3 has been carried out for the $\chi_b(1P)\pi\pi$ final state as well. The multiplicity of $\chi_b(1P)\pi\pi$ candidates, shown in Figure 6.8., is rather high, as expected since the same considerations used before for the "pion pollution" also applied here. As done in section 5.3, the same criteria can be tried to get rid of the multiplicity in the case of the $\chi_b(1P)\pi\pi$ final state, thus rejecting part of the combinatorial background. Figure 6.10. represents the invariant mass distribution of the $\chi_b(1P)\pi\pi$ candidates after applying the criterion of choosing the candidate with the highest P_T value in the event, whereas Figure 6.11. presents the invariant mass distribution of the $\chi_b(1P)\pi\pi$ candidates after applying the criterion of choosing the candidate with the highest vertex fit probability in the event.

A new study, similar to in section 5.3, has been performed using another signal MC sample, with the generated X_b mass still chosen to be 10.7 GeV. The MC truth matching technique is now more complicated because of the additional photon. The invariant mass distributions of $\chi_b(1P)\pi\pi$ candidates, with and without the MC truth-matching requirement, are given -as a reference- in Figure 6.12.. Figure 6.13. shows the reconstructed invariant mass distribution of the $\chi_b(1P)\pi\pi$ candidates before and after the application of the selection criterion of the highest-P_T candidate in the event, whereas Figure 6.14. illustrates the reconstructed invariant mass distribution of the $\chi_b(1P)\pi\pi$ candidates before and after the application of the selection criterion of the highest vertex fit probability candidate in the event.

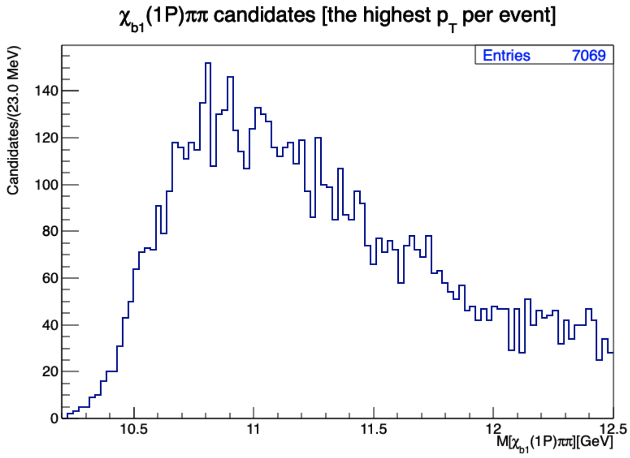

Figure 6.10. The invariant mass distribution the $\chi_b(1P))\pi^+\pi^-$ after applying the criteria of choosing the candidate the highest P_T value in the event

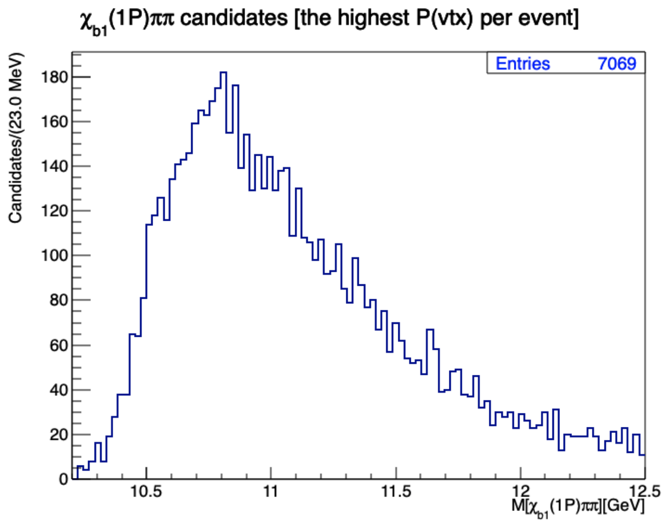

Figure 6.11. The invariant mass distribution the $\chi_b(1P)\pi^+\pi^-$ after applying the criteria of choosing the candidate the highest vertex fit probability in the event

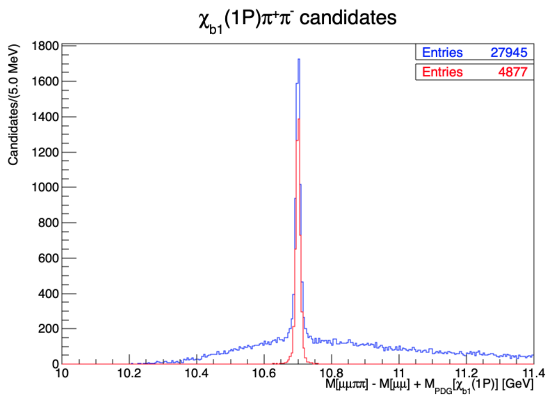

Figure 6.12. The invariant mass distribution of $\chi_b(1P)\pi^+\pi^-$ candidates obtained by analyzing the signal MC sample with generated $m(X_b)$ = 10.7 GeV. The blue/red lines represent the reconstructed candidates before/after applying the MC truth matching requirement

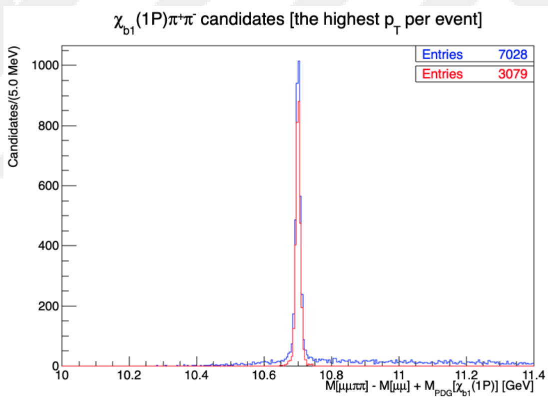

Figure 6.13. The invariant mass distribution of $\chi_b(1P)\pi^+\pi^-$ candidates obtained by analyzing the MC sample with generated mass value $m(X_b)$ = 10.7 GeV. The blue/red lines represent reconstructed candidates and truth-matched candidates after choosing the candidate with the highest P_T value in the event

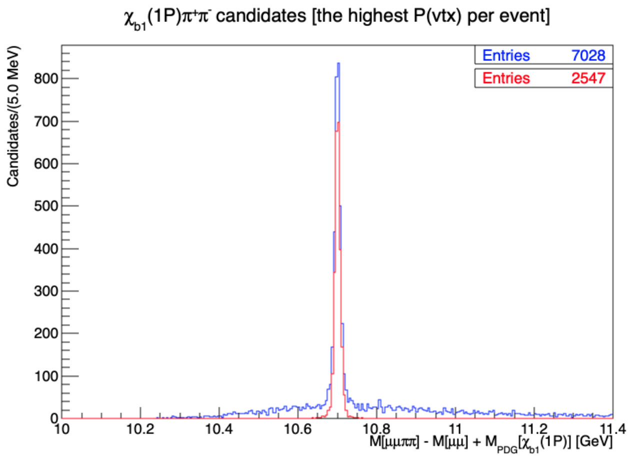

Figure 6.14. The invariant mass distribution of $\chi_b(1P)\pi^+\pi^-$ candidates obtained by analyzing the MC sample with generated mass value $m(X_b)$ = 10.7 GeV. The blue/red lines represent reconstructed candidates and truth-matched candidates after choosing the candidate with the highest vertex fit probability in the event

	Baseline Selection	Highest P_T Selection	Highest P(vtx) Selection
Total	3763	2366	3374
True	4804	3038	2520
Fake	2596	725	854
Fake Rate %	35.08	**19.26**	**25.31**
ε_{cut} %		**63.23**	**52.45**

Table 6.2. The comparison of the differences in the fake rate and the efficiency of the two criteria.

For both multiplicity rejection criteria, the signal efficiency ε_{cut} and the fake rate are reported in Table 6.2.. They are respectively calculated, in the mass signal window [10.67, 10.73] GeV, as ratios of true and fake candidates concerning all candidates, before and after applying both multiplicity rejection criteria. As can be clearly seen from the numbers in Table 6.2., the result of this new study is similar to the previous one, namely that the choice of the highest-P_T candidate in the event is better performing than the choice of the highest vertex probability candidate in the event.

6.3. Full Mass Spectra Resolution Study for $\chi_b(1P)\pi^+\pi^-$ Final State

Simulated samples (reported in Table 4.3.) with different run conditions (corresponding to 2016, 2017, and 2018 data taking) have been used to extract the experimental mass resolutions and the reconstruction efficiencies as a function of the mass, for the $\chi_b(1P)\pi^+\pi^-$ final state (8 generated mass values for the hypothetical X_b particle). The simulated signals have been studied after applying the MC truth matching. In order to obtain each fit distribution, the Double Gaussian fit was used by superimposing the two components and sharing the same mean. These distributions for three years and 9 generated mass values are given in Appendix C. In order to illustrate, Figures 6.15. shows the fitted distributions of the invariant mass $\chi_b(1P)\pi^+\pi^-$ after MC truth matching for 2018 MC data and 12.0 GeV mass. Figures 6.16. summarize the results for $\chi_b(1P)\pi^+\pi^-$ final state. Fits (one for each year) are superimposed to the data for the sets of simulated masses obtained after applying MC truth matching. These results extrapolated to the whole mass spectrum are crucial in extracting the Upper Limits in the X_b production cross-sections as a further study.

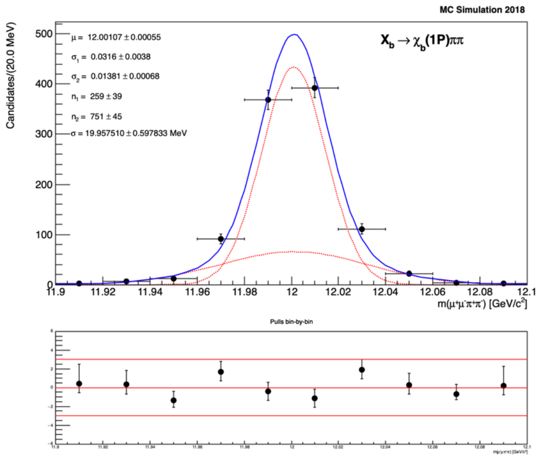

Figure 6.15. The fitted distributions of the invariant mass $\chi_b(1P)\pi^+\pi^-$ after MC truth matching for 2018 MC 12.0 GeV mass.

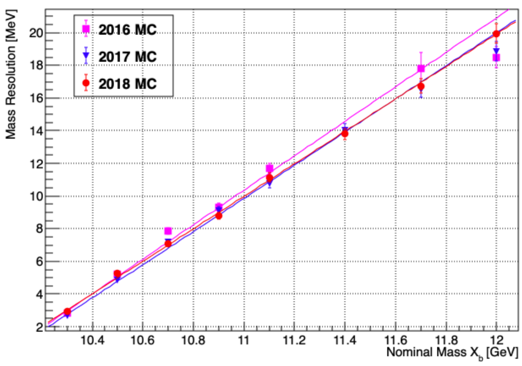

Figure 6.16. Fits to the mass resolution as a function of the mass for the $\chi_b(1P)\pi^+\pi^-$ final state

6.4. Comparison Between Data and MC Samples for $\chi_b(1P)\pi^+\pi^-$ Final State

This study has been performed to be sure there are no remarkable discrepancies between data and MC events. The simulated signal sample which is used for this study is the generated for $m(X_b) = 10.7$ GeV. If remarkable discrepancies are found between data and MC events, it might be required to think about a re-weighting procedure for $X_b \to \chi_b(1P)\pi^+\pi^-$ decay mode. The P_T and η comparisons between data and MC events after applying all the selection criteria which are given in Table 6.1 for $\chi_b(1P)\pi^+\pi^-$, $\chi_b(1P)$, photon, leading π, softer π and $\pi^\pm$ are given in Appendix D. In order to illustrate, the comparison between data and MC events for $\chi_b(1P)\pi^+\pi^-$ P_T and η distributions are given in Figure 6.17. and 6.18., respectively. As can be seen from the comparison of the distributions, there are no remarkable discrepancies between data and MC events.

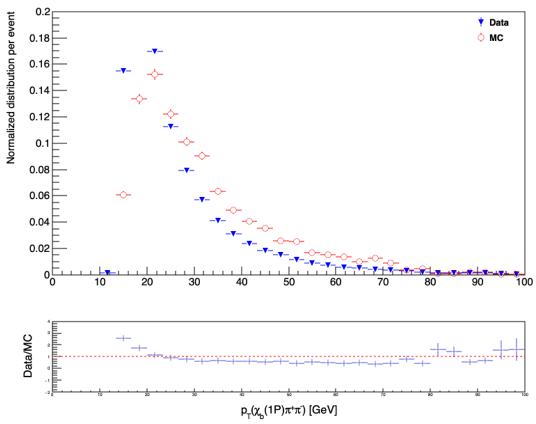

Figure 6.17. The comparison between data and MC events for $\chi_b(1P)\pi^+\pi^-$ P_T distribution

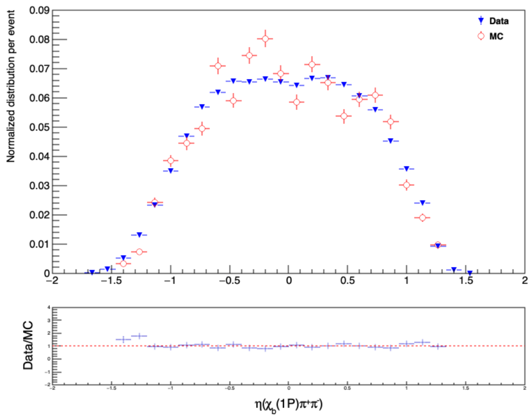

Figure 6.18. The comparison between data and MC events for $\chi_b(1P)\pi^+\pi^-$ η distribution

7. CONCLUSIONS

In this thesis, an analysis of $\Upsilon(1S)\pi^+\pi^-$ and $\chi_{b1}(1P)\pi^+\pi^-$ final states have been presented, with the purpose to search for the possible exotic X_b signal, by exploiting the nearly whole data sample collected during the Run-II data taking by the CMS experiment. Two decay chains were fully implemented and configured to obtain the distributions for the $\Upsilon(1S)\pi^+\pi^-$ and $\chi_{b1}(1P)\pi^+\pi^-$ final states. The reconstruction of the $\chi_b(1P)$ state through its radiative decay has shown the importance of the photons reconstructed by their conversion in the CMS Tracker material.

Since the amount of data and the size of the derived rootuples were quite large, the extraction of several signals was performed in the PROOF-Lite/ROOT frame to take advantage of conventional parallel computing (CPU). The kinematical and topological cut-based selections have been implemented and reasonably optimized to reduce the extensive combinatorial backgrounds mainly introduced by the additional pion pairs. The performance of two criteria to reject the multiple candidates per event has been evaluated by using simulated signal samples and the Monte Carlo truth-matching technique.

As a consequence of these studies, the obtained spectra for the two final states ($\Upsilon(1S)\pi^+\pi^-$ and $\chi_{b1}(1P)\pi^+\pi^-$) allow reporting no significant peaking structure that could be associated to the hypothetical X_b exotic state. This result holds the amount of LHC Run-II data collected by the CMS experiment and its current sensitivity. Additional data will be available from the Run-III data taking, foreseen for the period 2022-2024. The work carried out in this thesis provides all the ingredients to allow the extraction of current Upper Limits to the prompt production cross-section of this hypothetical X_b exotic state, which can be helpful in the theoretical studies carried out in the field of exotic hadron spectroscopy.

REFERENCES

LefÃĺvre, Christiane (2008). "The CERN accelerator complex". URL: `https://cds.cern.ch/record/1260465`.

Aad, G. et al. (2014). "Search for the X_b and other hidden-beauty states in the $\pi^+\pi^-\Upsilon(1S)$ channel at ATLAS". In: *Phys. Lett. B*. DOI: `doi:/10.1016/j.physletb.2014.11.055`.

Aad, Georges et al. (2012a). "Observation of a New χ_b State in Radiative Transitions to $\Upsilon(1S)$ and $\Upsilon(2S)$ at ATLAS". In: *Phys. Lett. B*. DOI: `doi:/110.1103/PhysRevLett.108.152001`.

— (2012b). "Observation of a new particle in the search for the Standard Model Higgs boson with the ATLAS detector at the LHC". In: *Phys. Lett. B* (B716). DOI: `doi:10.1016/j.physletb.2012.08.020`.

Aaij, R. et al. (2014). "Measurement of the $\chi_b(3P)$ mass and of the relative rate of $\chi_{b2}(1P)$ and $\chi_{b2}(1P)$ production". In: *J. High Energy Phys.* DOI: `doi:/10.1007/JHEP10(2014)088`.

Abe, F. et al. (1997). "J/ψ and $\psi(2S)$ production in $p\bar{p}$ collisions at $\sqrt{s}$ = 1.8 TeV". In: *Phys. Lett. B*. DOI: `doi:/10.1103/PhysRevLett.79.572`.

Ahmad, Q. R. et al. (2001). "Measurement of the rate of ν_e + d $\rightarrow p^+p^+e^-$ interactions produced by ^{8}B solar neutrinos at the Sudbury Neutrino Observatory". In: *Phys. Lett. B*. DOI: `doi:10.1103/PhysRevLett.87.071301`.

AlFiky, M. T. et al. (2006). "X(3872): Hadronic Molecules in Effective Field Theory". In: *Phys. Lett. B*. DOI: `doi:/10.1016/j.physletb.2006.07.069`.

ALICE Collaboration (2008). "The ALICE Experiment at the CERN LHC". In: *Journal of Instrumentation*. DOI: `doi:/10.1088/1748-0221/3/08/S08002`.

Andronic, A. et al. (2016). “Heavy-flavour and quarkonium production in the LHC era: from proton-proton to heavy-ion collisions”. In: *The European Physical Journal C*. DOI: doi:/10.1140/epjc/s10052-015-3819-5.

Aubert, J. J. et al. (1974). “Reliable Perturbative Results for Strong Interactions?” In: *Phys. Lett. B*. DOI: doi:/110.1103/PhysRevLett.33.1404.

Augustin, J. E. et al. (1974). “Discovery of a Narrow Resonance In e^+e^- Annihilation”. In: *Phys. Lett. B*. DOI: doi:/110.1103/PhysRevLett.33.1406.

Baier, R. et al. (1983). “Hadronic collisions: A quarkonium factory”. In: *Zeitschrift für Physik C Particles and Fields*. DOI: doi:/10.1007/bf01572254.

Belle Collaboration (2003). “Observation of a Narrow Charmoniumlike State in Exclusive $B\pm \rightarrow K \pm \pi^+\pi^- J/\Psi$ Decays”. In: *Phys. Lett. B*. DOI: doi:/10.1103/PhysRevLett.91.262001.

Bodwin, G. T. et al. (1995). “Rigorous QCD analysis of inclusive annihilation and production of heavy quarkonium”. In: *Phys. Lett. B*. DOI: doi:/10.1103/physrevd.51.1125.

Brambilla, N. (2011). “Heavy quarkonium: progress, puzzles, and opportunities”. In: *The European Physical Journal C*. URL: https://link.springer.com/article/10.1140/epjc/s10052-010-1534-9.

Cawlfield, C. et al. (2006). “Experimental Study of χ_b(2P)$\rightarrow \pi\pi\chi_b$(1P)”. In: *Phys. Lett. B*. DOI: doi:/10.1103/PhysRevD.73.012003.

Chatrchyan, S. et al. (2013). “Search for a new bottomonium state decaying to $\Upsilon(1S)\pi^+\pi^-$ in pp collisions at $\sqrt{s}$ = 8 TeV”. In: *Phys. Lett. B*. DOI: doi:/10.1016/j.physletb.2013.10.016.

Choi, S. K. et al. (2007). “Observation of a resonance-like structure in the $\pi^\pm\Psi$ mass distribution in exclusive $B \rightarrow K\pi^\pm\Psi$ decays”. In: *Phys. Lett. B*. DOI: doi:/10.1103/PhysRevLett.100.142001.

Clowe, Douglas et al. (2006). “A direct empirical proof of the existence of dark matter”. In: *Astrophys. J.* URL: https://iopscience.iop.org/article/10.1086/508162/pdf.

CMS Collaboration (1997). “The CMS Magnet Project Technical Design Report”. URL: https://cds.cern.ch/record/331056/files/Magnet%5C_TDR%5C_complete.pdf.

— (2000). “CMS TriDAS project: Technical Design Report, Volume 1: The Trigger Systems”. URL: http://cds.cern.ch/record/706847.

— (2006). “CMS Physics: Technical Design Report Volume I: Detector Performance and Software”. URL: http://cds.cern.ch/record/922757.

— (2008). “The CMS Experiment at the CERN Large Hadron Collider”. In: *Journal of Instrumentation*. DOI: doi:/10.1088/1748-0221/3/08/S08004.

— (2009). “Identification and Filtering of Uncharacteristic Noise in the CMS Hadron Calorimeter”. DOI: doi:/10.1088/1748-0221/5/03/T03014.

— (2018). “The Phase-2 Upgrade of the CMS Beam Radiation Instrumentation and Luminosity Detectors”. URL: https://cds.cern.ch/record/2759074?ln=en.

— (2019). “CMS Luminosity - Public Results”. URL: https://twiki.cern.ch/twiki/bin/view/CMSPublic/LumiPublicResults.

— (2020). “Observation of the $B_0^s \to X(3872)\phi$ decay”. In: *Phys. Lett. B*. DOI: doi:/10.1103/PhysRevLett.125.152001.

— (2021). “Observation of a new excited beauty strange baryon decaying to $\Xi_b^-\pi^+\pi^-$”. In: *Phys. Rev. Lett.* URL: https://arxiv.org/abs/2102.04524.

Collins, J. C. et al. (1982). “Parton distribution and decay functions”. In: *Nuclear Physics B*. DOI: doi:/10.1016/0550-3213(82)90021-9.

Cowan, G. et al. (2018). "Tetraquarks and pentaquarks". In: URL: https://inspirehep.net/literature/1686740.

Dominguez, A. et al. (2012). "CMS Technical Design Report for the Pixel Detector Upgrade". In: DOI: doi:/10.2172/1151650.

Faccioli, P. et al. (2010). "Towards the experimental clarification of quarkonium polarization". In: *The European Physical Journal C*. URL: https://link.springer.com/article/10.1140/epjc/s10052-010-1420-5.

Fritzsch, Harald (1977). "A direct empirical proof of the existence of dark matter". In: *Phys. Lett. B*. DOI: doi:/10.1016/0370-2693(77)90108-3.

Glashow, S. L. et al. (1975). "Is bound charm found?" In: *Phys. Lett. B*. DOI: doi:/110.1103/PhysRevLett.34.46.

Halzen, F. et al. (1977). "CVC for Gluons and Hadroproduction of Quark Flavours". In: *Phys. Lett. B*. DOI: doi:/10.1016/0370-2693(77)90144-7.

Herb, S. W. et al. (1977). "Observation of a Dimuon Resonance At 9.5 Gev in 400-gev Proton-Nucleus Collisions". In: *Phys. Lett. B*. DOI: doi:/110.1103/PhysRevLett.39.252.

Higgs, Peter W. (1964). "Broken Symmetries and the Masses of Gauge Bosons". In: *Phys. Rev. Lett*. DOI: doi:10.1103/PhysRevLett.13.508.

Karliner, M. et al. (2015a). "X(3872), X_b, and the χ_{b1}(3P) state". In: *Phys. Lett. B*. DOI: doi:/10.1103/PhysRevD.91.014014.

— (2015b). "X(3872), X_b, and the χ_{b1}(3P) state". In: *J. High Energy Phys.* URL: https://arxiv.org/abs/1304.0345.

Khachatryan, V. et al. (2015). "Measurement of the production cross section ratio $\sigma(\chi_{b2}(1P))/\sigma(\chi_{b1}(1P))$ in pp collisions at $\sqrt{s} = 8$ TeV". In: *Phys. Lett. B*. DOI: doi:/10.1016/j.physletb.2015.02.048.

Khachatryan, V. et al. (2017). “The CMS trigger system”. In: *Journal of Instrumentation*. DOI: doi:/10.1088/1748-0221/12/01/P01020.

Kwong, W. et al. (1988). “D-wave quarkonium levels of the Υ family”. In: *Phys. Lett. B*. DOI: doi:/10.1103/PhysRevD.38.279.

Lees, J. P. et al. (2011). “Study of di-pion bottomonium transitions and search for the h_b(1P) state”. In: *Phys. Lett. B*. DOI: doi:/10.1103/PhysRevD.84.011104.

Lezki, S. (2019). “Search for exotic bottomonium-like resonances in $\Upsilon(1S)\pi^+\pi^-$ and $\chi_b(1P)\pi^+\pi^-$ final states at the CMS experiment”. In:

LHCb Collaboration (2008). “The LHCb Detector at the LHC”. In: *Journal of Instrumentation*. DOI: doi:/10.1088/1748-0221/3/08/S08005.

— (2016). “Observation of $\Lambda_b^0 \to /\psi(2S)pK^-$ and $\Lambda_b^0 \to J/\psi pK^-$”. In: *J. High Energy Phys.* URL: https://link.springer.com/article/10.1007/JHEP05(2016)132.

— (2021). “List of hadrons observed at the LHC”. In: URL: https://cds.cern.ch/record/2749030/files/FIGURE-2021-001.pdf.

Luca, C. (2017). “The CMS Level-1 Trigger for LHC Run II”. In: *Journal of Instrumentation*. DOI: doi:/10.1088/1748-0221/12/03/C03021.

Ma, Y. Q. et al. (2016). “Quarkonium production in an improved color evaporation model”. In: *Phys. Lett. B*. DOI: doi:/10.1103/PhysRevD.94.114029.

Nayak, G. C. et al. (2005). “Fragmentation, NRQCD and NNLO factorization analysis in heavy quarkonium production”. In: *Phys. Lett. B*. DOI: doi:/10.1103/PhysRevD.72.114012.

Nussinov, S. et al. (2013). “The doubly heavies: $\bar{Q}Q\bar{q}q$ and $QQ\bar{q}\bar{q}$ tetraquarks and QQq baryons”. In: *J. High Energy Phys.* URL: https://arxiv.org/abs/1304.0345.

Olive, K. A. et al. (2014). “X(3872) Mass from $\bar{D}^0D^{0*}$”. In: *Chin. Phys.* URL: https://pdg.lbl.gov/2014/listings/rpp2014-list-X-3872.pdf.

Piotr, Traczyk (2021). “59 new hadrons and counting”. URL: https://home.cern/news/news/physics/59-new-hadrons-and-counting.

Politzer, H. D. (1973). “Reliable Perturbative Results for Strong Interactions?” In: *Phys. Lett. B*. DOI: doi:/110.1103/PhysRevLett.30.1346.

Purcell, A. (2012). “Go on a Particle Quest at the First CERN Webfes”. URL: https://cds.cern.ch/record/1473657.

Sakuma, T. et al. (2014). “Detector and Event Visualization With SketchUp at the CMS Experiment”. In: *J. Phys. Conf. Ser.* DOI: doi:/10.1088/1742-6596/513/2/022032.

Sanchez, G. R. et al. (2017). “χ_b studies at 13 TeV”. In: *CMS AN -2017/250*.

Schaumann, M. et al. (2018). “First Xenon-Xenon Collisions in the LHC”. In: DOI: doi:/10.18429/JACoW-IPAC2018-MOPMF039.

Segal, Ben (1995). “A Short History of Internet Protocols at CERN”. URL: http://ben.home.cern.ch/ben/TCPHIST.html.

SELEX Collaboration (2002). “First Observation of the Doubly Charmed Baryon Ξ_{cc}^{++}”. In: *Phys. Lett. B*. DOI: doi:/10.1103/PhysRevLett.89.112001.

Severini, H. et al. (2004). “Observation of the Hadronic Transitions $\chi_{b1,2}$(2P)→ $\omega\Upsilon$(1S)”. In: *Phys. Lett. B*. DOI: doi:/10.1103/PhysRevLett.92.222002.

Sirunyan, A. M. et al. (2012). “Observation of the χ_b1(3P) and χ_b2(3P) and Measurement of their Masses”. In: *Phys. Lett. B*. DOI: doi : /110 . 1103 / PhysRevLett.121.092002.

Tanabashi, M. et al. (2018). “Review of Particle Physics”. In: *Phys. Lett. B*. DOI: doi:/110.1103/PhysRevD.98.030001.

Tornqvist, N. A. (1994). “From the Deuteron to Deusons, an Analysis of Deuteron like Meson-Meson Bound State”. In: *J. High Energy Phys.* DOI: doi:/10.1007/BF01413192.

— (2004). “Isospin breaking of the narrow charmonium state of Belle at 3872 MeV as a deuson”. In: *Phys. Lett. B*. DOI: doi:/10.1016/j.physletb.2004.03.077.

UA2 Collaboration (1983). “Evidence for $Z^{0\prime} rightarrow^{+-}$ at the CERN pp collider”. In: *Phys. Lett. B*. DOI: doi:/10.1016/0370-2693(83)90744-X.

CURRICULUM VITAE
Candan ISIK

4 Rue Fayette 1094,
01630 Saint Genis-Pouilly, France
✉ *candan.isik@cern.ch*

Education

2015 – 2021 **PhD. degree in High Energy Physics**.
Cukurova University, Adana, Turkey
Advisors: Prof. Isa Dumanoglu (Cukurova University), Prof. Alexis Pompili (University of Bari Aldo Moro & INFN section of Bari)
Thesis title: *"Search of the hypothetical X_b exotic state into χ_b(1P)$\pi^+\pi^-$ final state with Run-II data collected by the CMS experiment at the Large Hadron Collider"*

2013 – 2015 **M.Sc degree in Solid State Physics**.
Cukurova University, Adana, Turkey
Advisor: Prof. Bekir Ozcelik (Cukurova University)
Thesis title: *"Production and characterization of FeSe-11 superconductors"*

2006 – 2011 **B.Sc. in Physics**.
Cukurova University, Adana, Turkey

Projects

2013–2015 **Production, characterization and magnetic properties of FeSe-122 super- conductors**.
Employer: Scientific and Technological Research Council of Turkey
Project Position: Researcher

2015–2017 **HCAL Upgrade and Physics Analysis in CMS Experiment**.
Employer: Turkish Atomic Energy Authority
Project Position: Researcher

2018–2021 **Detector Development/Upgrade and New Physics Analysis in CMS Experiment**.
Employer: Turkish Atomic Energy Authority
Project Position: Researcher

2020–2021 **Search of the hypothetical X_b exotic state into χ_b(1P)$\pi^+\pi^-$ final state with Run-II data collected by the CMS experiment at the Large Hadron Collider. Located in University of Bari Aldo Moro & INFN section of Bari**.
Employer: Scientific and Technological Research Council of Turkey
Project Position: Researcher

Grants Awarded

2016–2019 **Foundation: General Directorate of Higher Education Credit and Hostels Institution of Turkey**.

2019–2020 **Foundation: Fermilab & HCAL**.

2020–2021 **Foundation: Scientific and Technological Research Council of Turkey**.

Research Experience

2017–Present **Search of the hypothetical X_b exotic state into $\chi_b(1P)\pi^+\pi^-$ final state with Run-II data collected by the CMS experiment at the Large Hadron Collider**.

- Developing the analysis framework,
- Contribute to efficiency measurement,
- Study of the cut optimization.

2017–Present **Search of the hypothetical X_b exotic state into $\Upsilon(1S)\pi^+\pi^-$ final state with Run-II data collected by the CMS experiment at the Large Hadron Collider**.

- Developing the analysis framework,
- Contribute to efficiency measurement,
- Study of the cut optimization.

2021–Present **Analysis of 2017 and 2018 dataset for Hadronic Forward (HF)Vtrx investigation**.

- Developing the analysis framework,
- Producing the plots.
- Checking RSSI of HF.

2019-2020 **Installation of Hadronic Barrel (HB) Front-End electronics in CMS Detector**.

- Removing of all HB Phase-0 components from CMS at P5.
- Installing of all HB Phase-1 components in CMS at P5.
- HB Co60 Sourcing shift at P5.

2018-2017 **Preparation of Hadronic Barrel (HB) Front-End electronics for Full Insallation and Commissioning**.

- Reprogramming all HE1-18 RMs, CUs, and ngCCMs with bridge FW,
- Adding the QEI11 ID's in the database.
- Rasping and cleaning the Peltier cooling system.
- The commissioning and testing of CUs.
- Testing JTAG connectors.
- Testing Backplanes.

2017-2018 **High Granularity Calorimeter (HGCAL) Beam Test Analysis**.

- Contribution beam test shifts.
- Analysing the test beam data for the simulation.

2016-2017 **Hadronic Calorimeter (HCAL) Hadronic Endcap (HE) Beam Test**.

- Contribution beam test shifts.

2016-2017 **HE and HB Front End Preparation for Full Installation and Commissioning**.

- Reprogramming all HE1-18 RMs, CUs, and ngCCMs with bridge FW.
- Testing HB Calibration Unit quartz fibers.

Talks and posters

April 2015 **International Conference on Magnetic and Superconducting Materials (MSM15)**, Antalya/TURKEY.

Poster: *The Physical and magnetic properties of FeSe-11 superconductor*

Computing skills

Frameworks: CMSSW
Languages: PYTHON, C++, BASH
Libraries: ROOT, RooStats
Others: LATEX

Languages

TURKISH:Mothertongue
ENGLISH:Fluent

APPENDIX

A Full Mass Spectra Resolution Study for $\Upsilon(1S)\pi^+\pi^-$ Final State

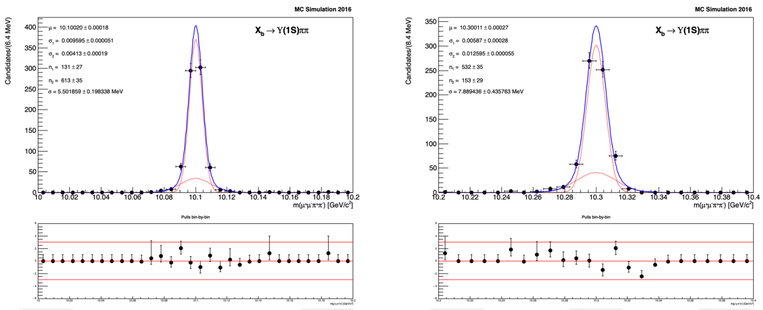

Figure A1. The fitted distributions of the invariant mass $\Upsilon(1S)\pi^+\pi^-$ after MC truth matching for 2016 MC data and (left/right) 10.1/10.3 GeV mass

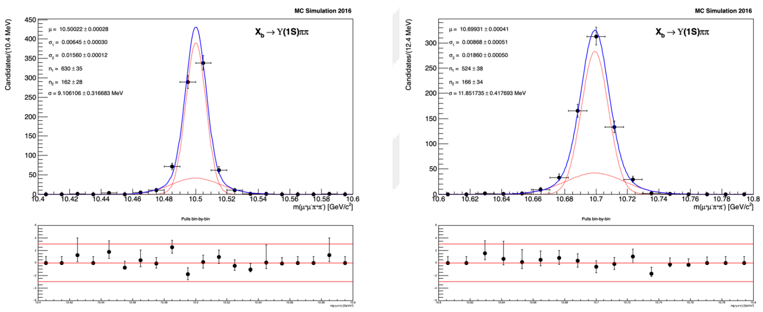

Figure A2. The fitted distributions of the invariant mass $\Upsilon(1S)\pi^+\pi^-$ after MC truth matching for 2016 MC data and (left/right) 10.5/10.7 GeV mass

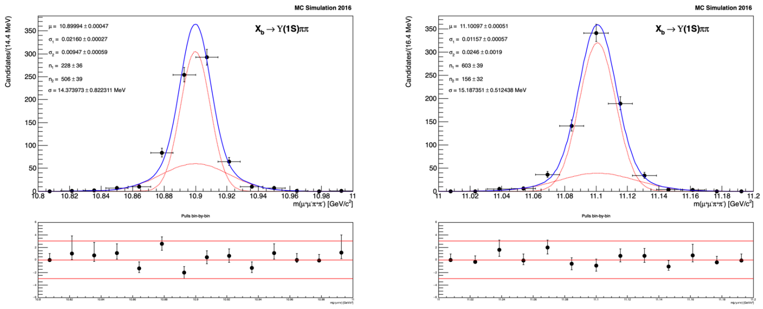

Figure A3. The fitted distributions of the invariant mass $\Upsilon(1S)\pi^+\pi^-$ after MC truth matching for 2016 MC data and (left/right) 10.9/11.1 GeV mass

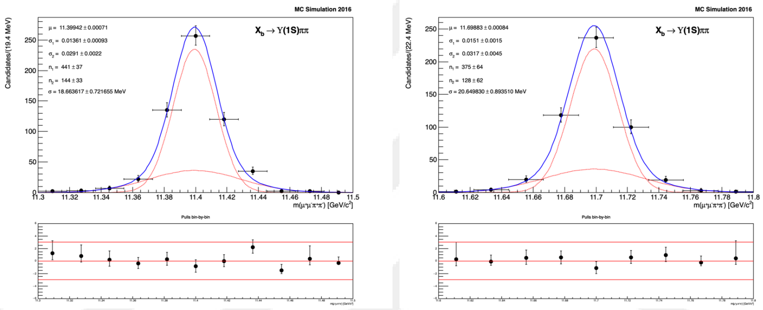

Figure A4. The fitted distributions of the invariant mass $\Upsilon(1S)\pi^+\pi^-$ after MC truth matching for 2016 MC data and (left/right) 11.4/11.7 GeV mass

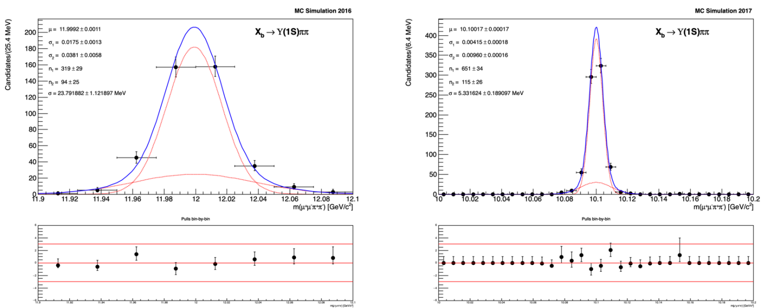

Figure A5. The fitted distributions of the invariant mass $\Upsilon(1S)\pi^+\pi^-$ after MC truth matching for (left/right) 2016/2017 MC data and 12.0/10.1 GeV mass

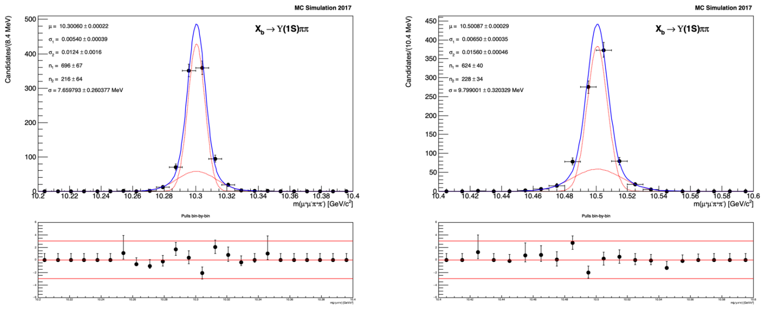

Figure A6. The fitted distributions of the invariant mass $\Upsilon(1S)\pi^{+}\pi^{-}$ after MC truth matching for 2017 MC data and (left/right) 10.3/10.5 GeV mass

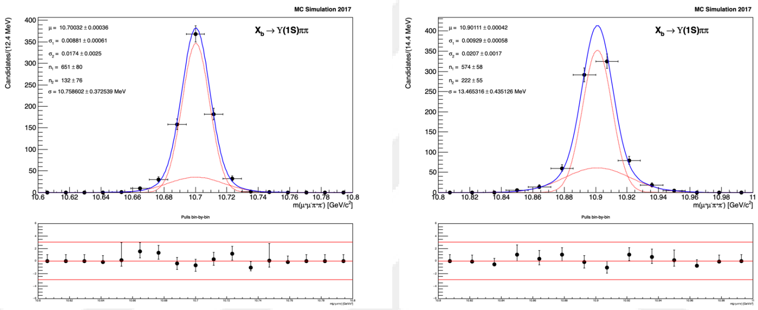

Figure A7. The fitted distributions of the invariant mass $\Upsilon(1S)\pi^{+}\pi^{-}$ after MC truth matching for 2017 MC data and (left/right) 10.7/10.9 GeV mass

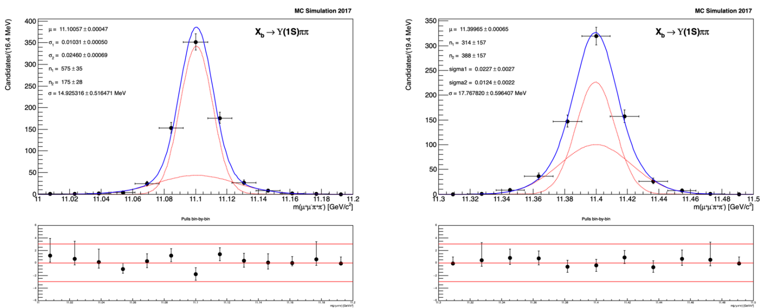

Figure A8. The fitted distributions of the invariant mass $\Upsilon(1S)\pi^{+}\pi^{-}$ after MC truth matching for 2017 MC data and (left/right) 11.1/11.4 GeV mass

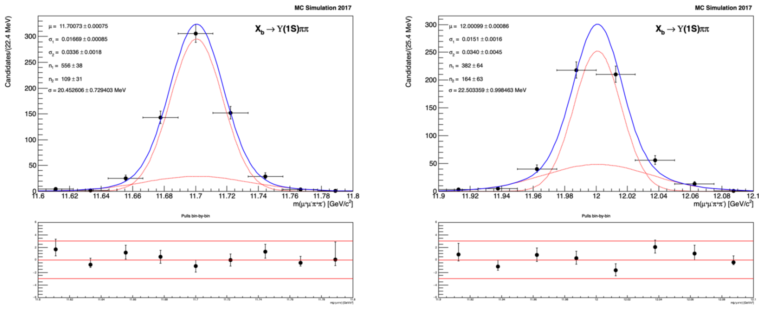

Figure A9. The fitted distributions of the invariant mass $\Upsilon(1S)\pi^+\pi^-$ after MC truth matching for 2017 MC data and (left/right) 11.7/12.0 GeV mass

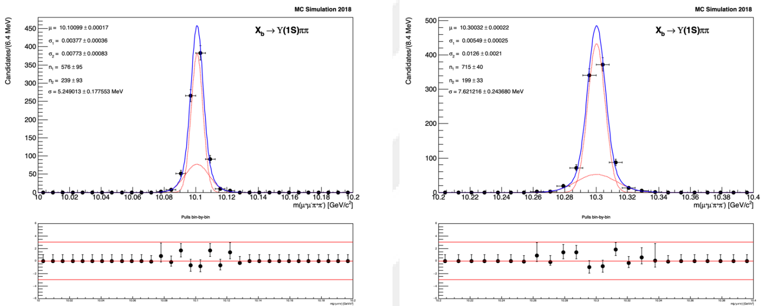

Figure A10. The fitted distributions of the invariant mass $\Upsilon(1S)\pi^+\pi^-$ after MC truth matching for 2018 MC data and (left/right) 10.1/10.3 GeV mass

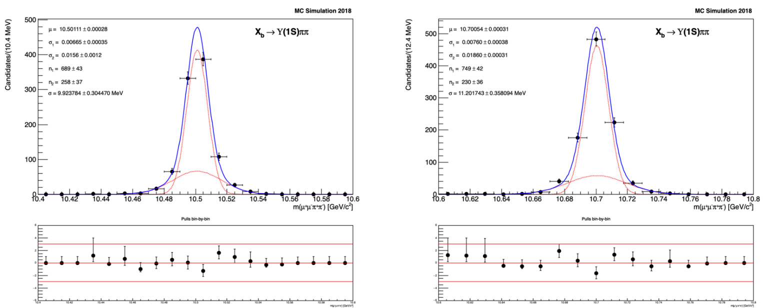

Figure A11. The fitted distributions of the invariant mass $\Upsilon(1S)\pi^+\pi^-$ after MC truth matching for 2018 MC data and (left/right) 10.5/10.7 GeV mass

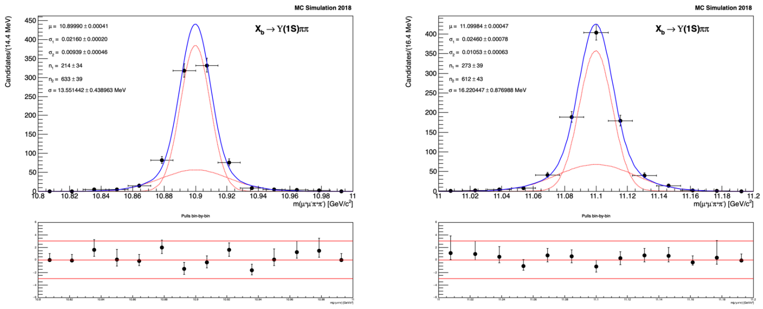

Figure A12. The fitted distributions of the invariant mass $\Upsilon(1S)\pi^{+}\pi^{-}$ after MC truth matching for 2018 MC data and (left/right) 10.9/11.1 GeV mass

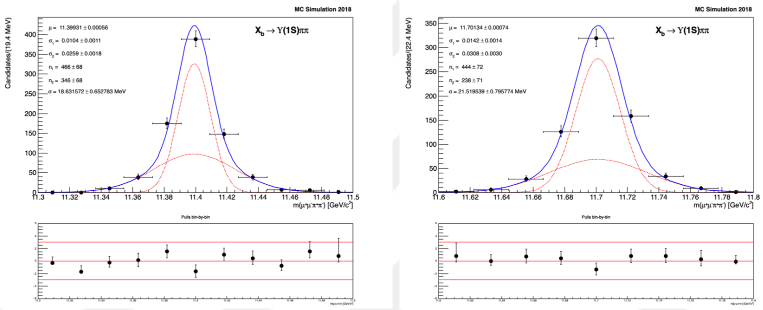

Figure A13. The fitted distributions of the invariant mass $\Upsilon(1S)\pi^{+}\pi^{-}$ after MC truth matching for 2018 MC data and (left/right) 11.4/11.7 GeV mass

B Comparison Between Data and MC Samples for $\Upsilon(1S)\pi^{+}\pi^{-}$ Final State

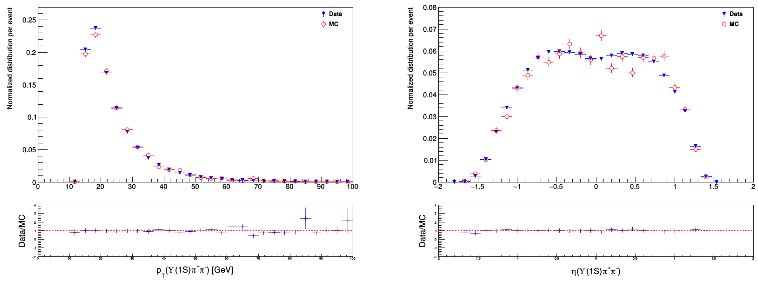

Figure B1. The comparison between data and MC events for $\Upsilon(1S)\pi^{+}\pi^{-}$ (left/right) P_{T} and η distributions

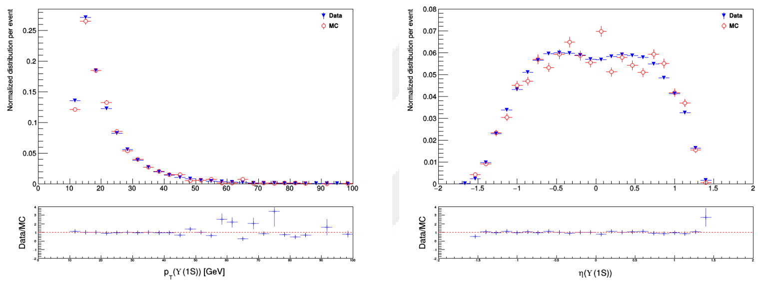

Figure B2. The comparison between data and MC events for $\Upsilon(1S)$ (left/right) P_{T} and η distributions

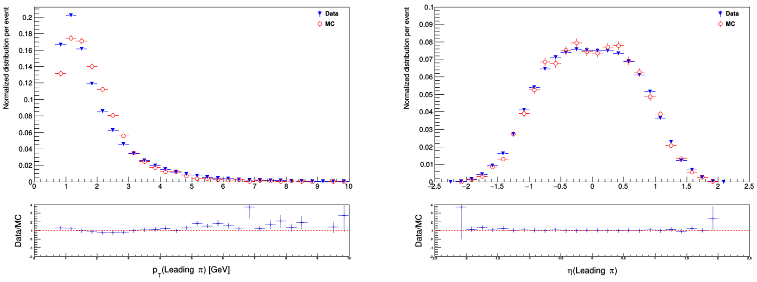

Figure B3. The comparison between data and MC events for leading π (left/right) P_T and η distributions

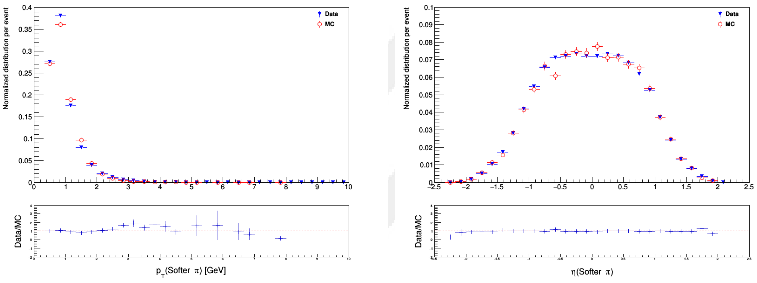

Figure B4. The comparison between data and MC events for softer π (left/right) P_T and η distributions

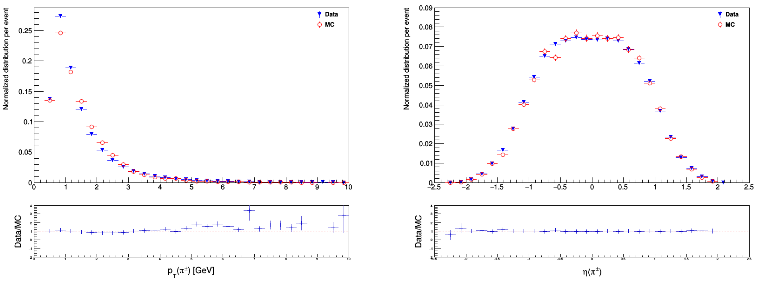

Figure B5. The comparison between data and MC events for $\pi^{\pm}$ (left/right P_T and η distributions.

C Full Mass Spectra Resolution Study for $\chi_b(1P)\pi^+\pi^-$ Final State

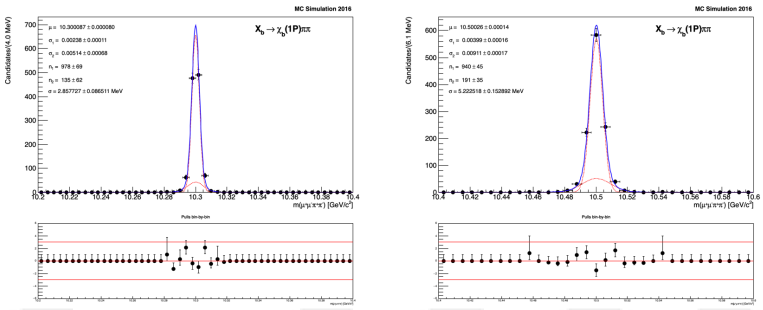

Figure C1. The fitted distributions of the invariant mass $\chi_b(1P)\pi^+\pi^-$ after MC truth matching for 2016 MC data and (left/right) 10.3/10.5 GeV mass

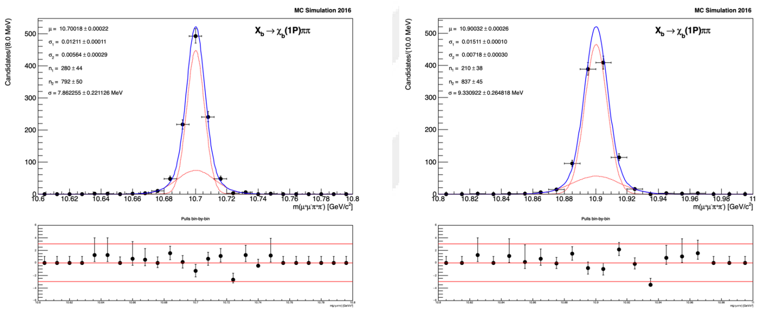

Figure C2. The fitted distributions of the invariant mass $\chi_b(1P)\pi^+\pi^-$ after MC truth matching for 2016 MC data and (left/right) 10.7/10.9 GeV mass

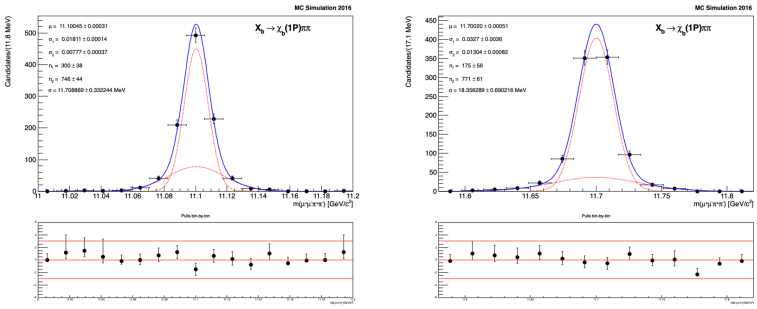

Figure C3. The fitted distributions of the invariant mass $\chi_b(1P)\pi^+\pi^-$ after MC truth matching for 2016 MC data and (left/right) 11.1/11.7 GeV mass

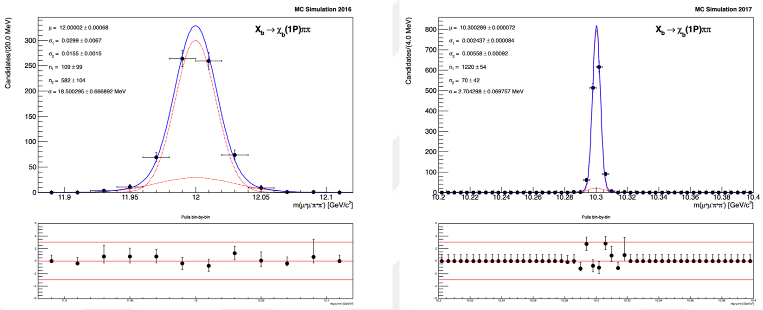

Figure C4. The fitted distributions of the invariant mass $\chi_b(1P)\pi^+\pi^-$ after MC truth matching for (left/right) 2016/2017 MC data and (left/right) 12.0/10.3 GeV mass

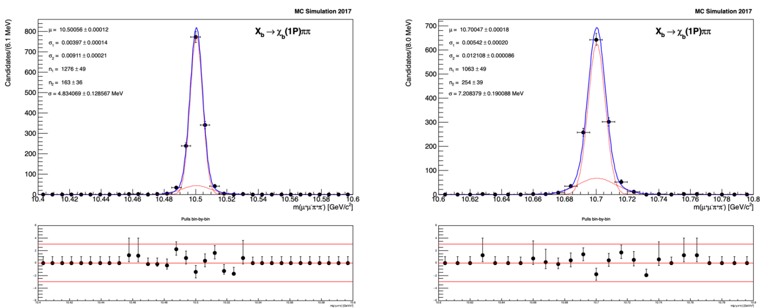

Figure C5. The fitted distributions of the invariant mass $\chi_b(1P)\pi^+\pi^-$ after MC truth matching for 2017 MC data and 10.5/10.7 GeV mass

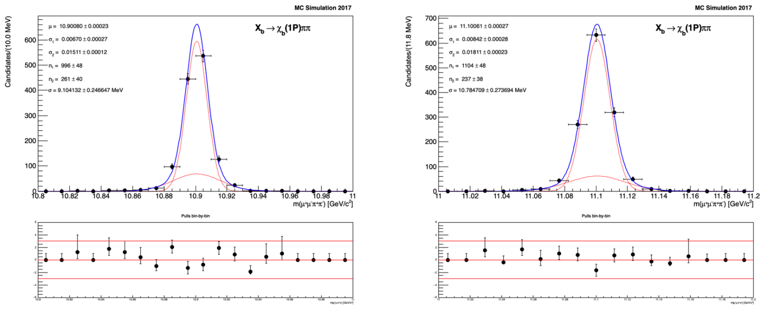

Figure C6. The fitted distributions of the invariant mass $\chi_b(1P)\pi^+\pi^-$ after MC truth matching for 2017 MC data and (left/right) 10.9/11.1 GeV mass

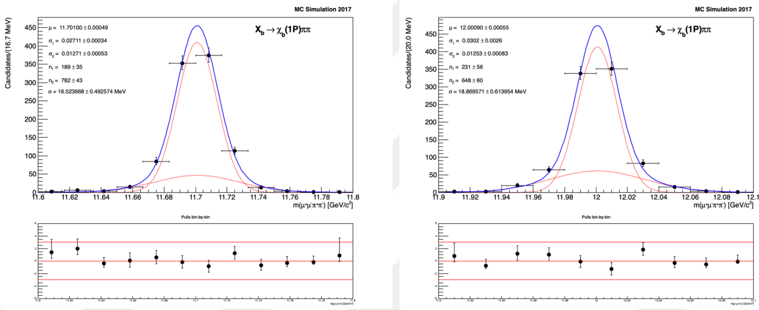

Figure C7. The fitted distributions of the invariant mass $\chi_b(1P)\pi^+\pi^-$ after MC truth matching for 2017 MC data and (left/right) 11.7/12.0 GeV mass

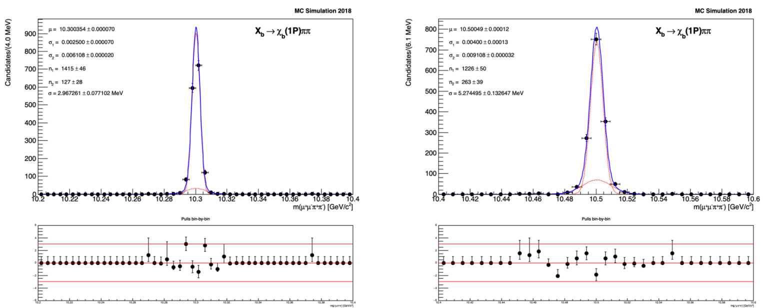

Figure C8. The fitted distributions of the invariant mass $\chi_b(1P)\pi^+\pi^-$ after MC truth matching for 2018 MC data and (left/right) 10.3/10.5 GeV mass

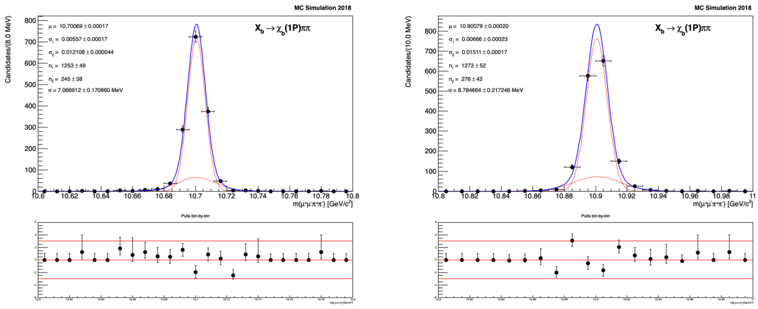

Figure C9. The fitted distributions of the invariant mass $\chi_b(1P)\pi^+\pi^-$ after MC truth matching for 2018 MC data and (left/right) 10.7/10.9 GeV mass

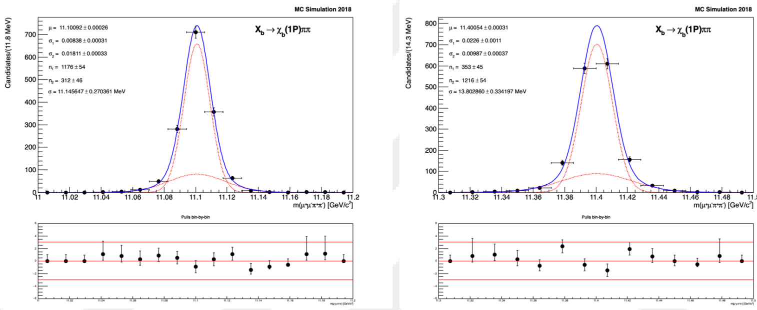

Figure C10. The fitted distributions of the invariant mass $\chi_b(1P)\pi^+\pi^-$ after MC truth matching for 2018 MC data and (left/right) 11.1/11.4 GeV mass

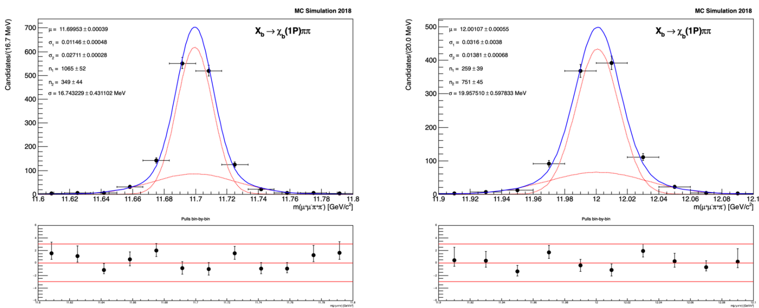

Figure C11. The fitted distributions of the invariant mass $\chi_b(1P)\pi^+\pi^-$ after MC truth matching for 2018 MC data and (left/right) 11.7/12.0 GeV mass.

D Comparison Between Data and MC Samples for $\chi_b(1P)\pi^+\pi^-$ Decay

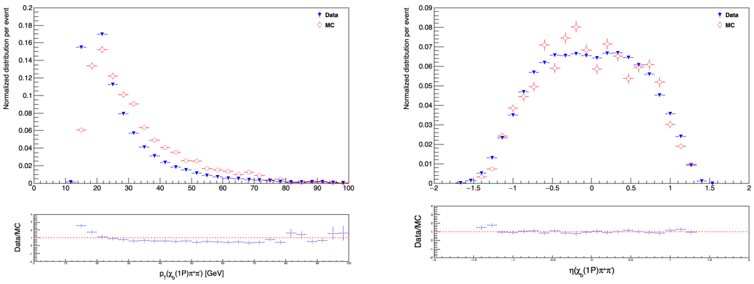

Figure D1. The comparison between data and MC events for $\chi_b(1P)\pi^+\pi^-$ (left/right) P_T and η distributions

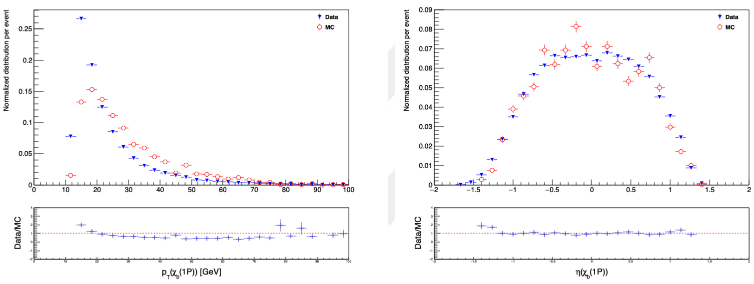

Figure D2. The comparison between data and MC events for $\chi_b(1P)$ (left/right) P_T and η distributions

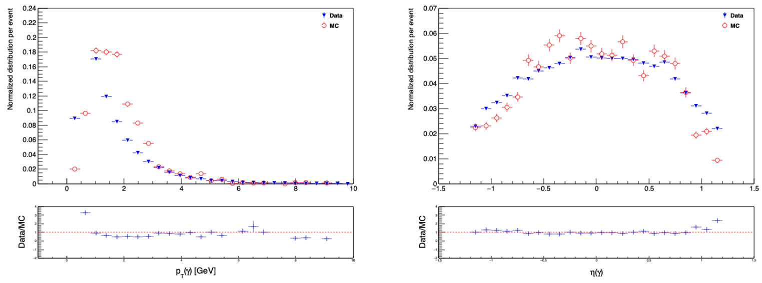

Figure D3. The comparison between data and MC events for γ (left/right) P_T and η distributions

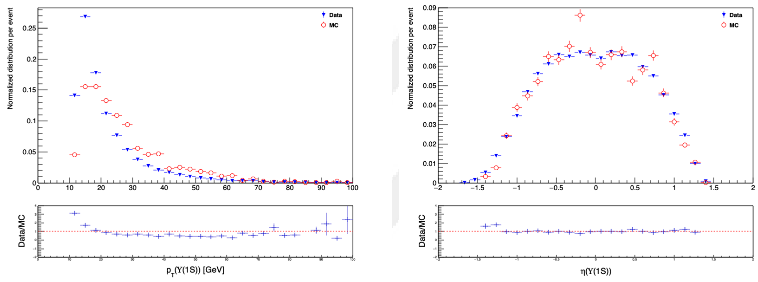

Figure D4. The comparison between data and MC events $\Upsilon(1S)$ (left/right) P_T and η distributions

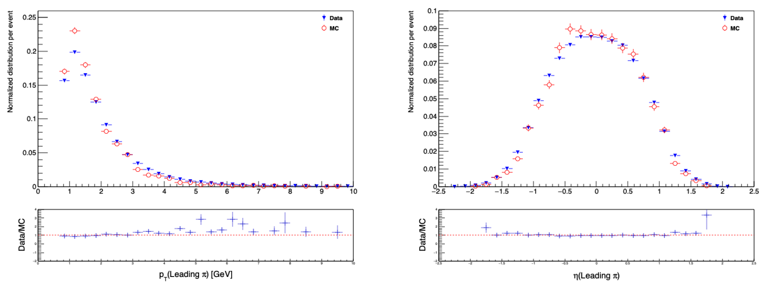

Figure D5. The comparison between data and MC events for leading π (left/right) P_T and η distributions

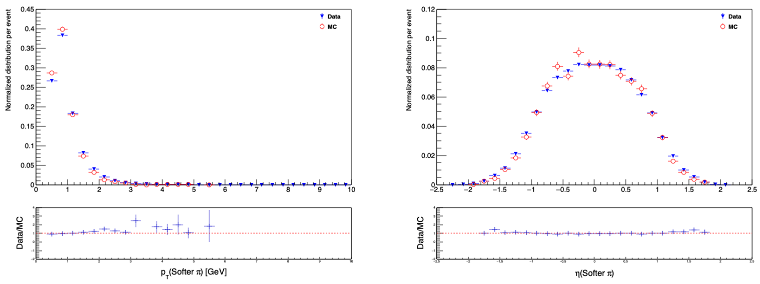

Figure D6. The comparison between data and MC events for softer π (left/right) P_T and η distributions

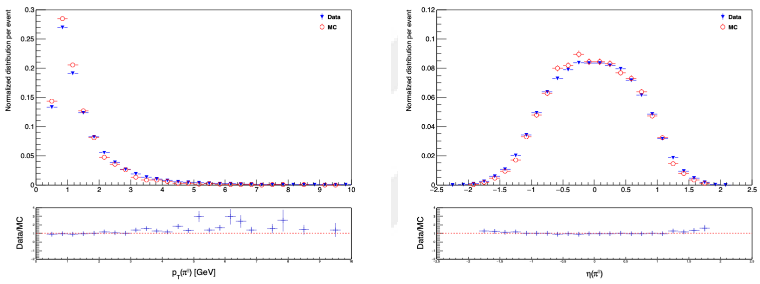

Figure D7. The comparison between data and MC events for $\pi^{\pm}$ (left/right) P_T and η distributions